MULTISCALE IN SILICO MODEL TO INVESTIGATE COMPROMISED BONE HEALING CONDITIONS

vorgelegt von

M. Sc.

Edoardo Borgiani

ORCID: 0000-0002-9645-2524

von der Fakultät V - Verkehrs- und Maschinensysteme
der Technischen Universität Berlin
zur Erlangung des akademischen Grades

Doktor der Ingenieurwissenschaften
- Dr.-Ing.-
genehmigte Dissertation

Promotionsausschuss:
Vorsitzender: *Prof. Dr.-Ing. Paul Uwe Thamsen*
Gutachter: *Prof. Dr.-Ing. habil. Manfred Zehn*
Gutachter: *Prof. Dr. Sara Checa Esteban*

Tag der wissenschaftliche Aussprache: *03.09.2020*
Berlin 2020

Essentially, all models are wrong,
but some are useful.

George E. P. Box

This achievement wouldn't have been possible
without the beloved moral sustainment
of my family and my friends.

The thesis is dedicated to you.

Table of content

List of Figures

List of Tables

Nomenclature

rhBMP-2	recombinant human Bone Morphogenetic Protein 2
BMP-2	Bone Morphogenetic Protein 2
MSC	Mesenchymal Stem Cell
TGFβ	Transforming Growth Factor β
FE	Finite Element
FEA	Finite Element Analysis
RAM	Random Access Memory
CPU	Central Processing Unit
CAE	Complete Abaqus Environment
.inp	Abaqus input file extension
.dat	Abaqus database file extension
.odb	Abaqus output database file extension
PEEK	PolyEther-Ether-Ketone
C3D8P	3-dimensional 8-node brick poroelastic mesh element
BW	Body Weight
CC	Calcified Cartilage
.cpp	C++ source code file extension
M. OB	Mature Osteoblast
IM. OB	Immature Osteoblast
CH	Chondrocyte

FB	Fibroblast
c.f.	chemotaxis factor
OB	Osteoblast
f.u.	fold units
SSP	Sum of the Squares of deviation about the mean
TSS	percentage of the Total Sum of Squares
µCT	Micro Computed Tomography
DOE	Design Of Experiments
SD	Standard Deviation
VEGF	Vascular Endothelial Growth Factor

Summary

Mechanics plays a key role in bone regeneration as it modulates the biological events taking place during the process. Extensive research has been done on elucidating the mechanical "rules" driving bone regeneration in uneventful healing conditions. However, under compromised healing conditions (e.g. aging, large bone defects) the mechanical regulation of healing might be altered and result in delayed healing or non-unions. The aim of this thesis was to investigate to what degree the mechano-regulation rules that have been identified for regular, uneventful healing still play a role in more challenging conditions. Among these conditions, aging and large bone defects were the focus of this study. The influence of mechanics on therapeutic solutions, as bone morphogenetic protein 2 (BMP-2), was also investigated to understand its role in the treatment of critical healing conditions.

A multiscale *in silico* approach that combined finite element analysis and agent-based computer models was used to simulate the bone healing process. The mechanical signals within the bone healing region were investigated using finite element techniques. Agent-based computer models simulated the cellular dynamics and BMP-2 concentration patterning within the callus. Computer model predictions were then compared to *in vivo* micro-CT and histological data at several time points over the course of healing. Aging effects on the mechano-regulation of healing was investigated *in silico* by using a design of experiment approach. The mechanobiological regulation of large bone defect healing was investigated in untreated conditions, under BMP-2 provision, under additional mechanical stimulation and under the combination of the two treatments.

The bone healing response to mechanical stimulation was observed to change with age. Reduction of cell mechano-response with aging could explain the differences on bone healing outcomes between adult and elderly mice under

different mechanical stability. Limited cellular activity could explain non-unions within untreated large bone defects. Furthermore, encapsulation of the medullary cavity was predicted in large defects due to an adverse mechanical environment. BMP-2 stimulated healing could be explained by its capacity to attract mesenchymal cells to migrate to the center of the fracture. Under BMP-2 treatment, the formation of a rigid callus since the first stages of healing was observed to weaken the contribution of additional mechanical stimulation on bone defect healing.

This study shows that mechanics plays a key role also in compromised healing conditions. Age-related reduction of cellular mechano-response points out the importance of mechanical stimulation as potential rehabilitative therapy for elderly patients. Under the mechanical environment that characterizes large bone defects, limited migration of mesenchymal cells was observed to lead to marrow encapsulation. Dose-Regulated chemotaxis was identified as a strong promoter to bridge the defect extremities and guarantee successful healing in critical conditions.

Zusammenfassung

Die Mechanik spielt eine Schlüsselrolle bei der Knochenregeneration, indem sie die biologischen Vorgänge dieses Prozesses beeinflusst. Umfangreiche Studien zur Aufklärung der mechanischen „Regeln“, die die Knochenregeneration unter komplikationslosen Heilungsbedingungen erforschen, wurden bereits durchgeführt. Allerdings kann unter beeinträchtigten Heilungsbedingungen (z.B. Alterung, große Knochendefekte) die mechanische Regulation der Heilung verändert werden und zu verzögerter Heilung oder Pseudoarthrose führen. Das Ziel dieser Doktorarbeit war zu untersuchen, inwiefern mechanisch-regulierende Regeln, die bei normaler, komplikationsloser Heilung identifiziert wurden, noch eine Rolle unter beeinträchtigten Bedingungen spielen. Unter diesen Bedingungen standen das Altern und große Knochendefekte im Mittelpunkt dieser Studie. Der Einfluss der Mechanik auf therapeutische Lösungen, wie die Anwendung des knochenmorphogenetischen Protein 2 (BMP-2), wurde ebenfalls untersucht, um deren Rolle in der Behandlung kritischer Heilungsbedingungen zu verstehen.

Ein skalenübergreifender *in silico* Ansatz, der Finite-Elemente-Analyse mit agentenbasierten Computermodellen kombiniert, wurde verwendet, um den Knochenheilungsprozess zu simulieren. Die mechanischen Signale in der Region der Knochenheilung wurden mit Finite-Elemente-Methoden untersucht. Agentenbasierte Computermodelle simulierten die Zelldynamik und BMP-2-Konzentrationsmuster innerhalb des Kallus. Die Vorhersagen des Computermodells wurden dann mit *in vivo* Mikro-CT und histologischen Daten an mehreren Zeitpunkten im Verlauf der Heilung verglichen. Der Einfluss von Alter auf die mechanische Regulierung der Heilung wurde anhand eines Design of Experiment Ansatzes *in silico* untersucht. Die mechanobiologische Regulierung der Heilung großer Knochendefekte wurde unter unbehandelten

Bedingungen, unter BMP-2-Versorgung, unter zusätzlicher mechanischer Stimulierung und unter der Kombination der beiden Behandlungen untersucht.

Es wurde beobachtet, dass sich die Reaktion der Knochenheilung auf mechanische Stimulierung mit dem Alter verändert. Eine altersbedingte Reduzierung der mechanischen Reaktion der Zellen könnte die Unterschiede des Knochenheilungsergebnisses zwischen erwachsenen und älteren Mäusen bei unterschiedlicher mechanischer Stabilität erklären. Beschränkte Zellaktivität in dieser Population könnte hingegen Pseudoarthrose in großen Knochendefekten begründen. Darüber hinaus wurde die Verkapselung der Markhöhle in großen Defekten aufgrund einer ungünstigen mechanischen Umgebung vorhergesagt. BMP-2-stimulierte Heilung konnte dadurch erklärt werden, dass dieser Wachstumsfaktor die Migration mesenchymaler Zellen in die Frakturmitte bewirkt. Unter BMP-2 Behandlung wurde beobachtet, dass die Bildung eines rigiden Kallus in der initialen Heilungsphase den Beitrag zusätzlicher mechanischer Stimulierung zur Knochendefektheilung schwächt.

Diese Studie zeigt, dass die Mechanik auch unter beeinträchtigten Heilungsbedingungen eine Schlüsselrolle spielt. Die altersbedingte Reduzierung der zellulären Mechano-Reaktion weist auf die Bedeutung der mechanischen Stimulation als mögliche rehabilitative Therapie für ältere Patienten hin. Unter der für große Knochendefekte spezifischen mechanischen Umgebung wurde beobachtet, dass eine begrenzte Migration von mesenchymalen Zellen zu einer Verkapselung des Knochenmarks führte. Es wurde festgestellt, dass eine dosisregulierte Chemotaxis die Überbrückung der defekten Extremitäten stark fördert und eine erfolgreiche Heilung unter kritischen Bedingungen gewährleistet.

1

INTRODUCTION

1.1. Clinical motivation

Bones provide to the skeleton the rigidity to protect internal organs and support the every-day loadings. However, the fragile nature of bones makes them susceptible to incur in fractures when they experience extreme mechanical stresses. Bones are capable to resist to the high loadings that the body experiences daily. However, their fragility typically increases with age that is coupled with a higher incidence of bone fractures [1]. A study reported that, in the US, one out of almost two women and five men will experience a bone fracture in their life after 50 years [2].

When a fracture occurs, the bone has the fascinating capacity to restore its original structure and functionality without leaving any scar on its surface [3]. The natural bone healing process spontaneously starts right after the fracture happens and needs several weeks to be completed [4]. The effective period is affected by different factors that could enhance or spoil the healing [5]. In fact, some fractures can result in delayed healing or still experience non-union several months after the injury [5].

Recovery of a bone fracture in elderly patients often generates long hospitalization periods and high costs [6]. Hip fracture, which is one of the most common injuries in elderly patients, requires a patient mean length of stay in hospital of around one month [7]. Moreover, 9% of the patients need to go under reoperation within 12 months from the hip fracture [7]. Increasing morbidity and mortality ratio due to hip fracture in the first year after the operation is another known complication. Even if the percentage of one-year mortality is reducing in the last decades, there is still a large group of patients that dies within the first 12 months after operation [8]. Identification of the mechanobiological aspects that most compromise the natural process of fracture healing is of primary importance to design new strategies to enhance healing in elderly patients. Therefore, the first aim of this study was to investigate age-related alterations in the mechanobiological regulation of bone healing.

Another clinically challenging condition relates to the treatment of large bone defects. Large bone defects are characterized by a large bone volume loss due to bone diseases, high-energy traumas or infected non-unions [9]. The wide fracture opening is a challenging condition for clinicians. If left untreated, in fact, bone defects tend to not heal still several weeks after the injury, resulting in the closure of the medullary cavity and a non-union. Autologous bone grafting is a common treatment for large bone defects, but its execution is challenging due to bone tissue availability [10]. Usually, growth factor supported treatment is a preferred alternative to autografts. Large bone defects are usually treated with recombinant human Bone Morphogenetic Protein 2 (rhBMP-2), which has been shown to enhance osteoinduction and reduce non-unions causalities [11]. However, Bone Morphogenetic Protein 2 (BMP-2) treatment can lead to heterotopic ossification, formation of abnormal trabecular bone and infections when the dosage is over proportionate [12]-[15]. Understanding the mechanobiology of BMP-2 stimulated healing is needed in order to optimize current treatment strategies. Therefore, the second aim of this study was to evaluate the mechanobiology of rhBMP-2 stimulated large bone defect healing.

1.2. Background

1.2.1. Bone Healing

Bone healing has caught the interest of the scientific community for many years [16]. The ability of bones to repair themselves is a subject that continues to fascinate the scientists and the failure of this capacity is a major clinical challenge. In fact, bone healing is a complex process that involves mechanics and biology on multiple levels of observation. The investigation of all the processes that cooperate to a complete bone healing is very challenging, especially since multiple tissues and cell types are involved in the progressive closing of the bone fracture or defect. In fact, according to the severity of the injury, the healing can happen through a direct bone bridging of the cortical extremities at the fracture site (primary bone healing) [4] or the natural formation of a callus, which is necessary to stabilize the fracture (secondary bone healing) [4]. In this latter case, the process requires a period of several weeks to be considered complete. Five overlapping phases are identified to describe the entire secondary bone healing process, from the fracture opening to the full restoration of the bone original functions [17]: hematoma formation phase (a), anti-inflammatory phase (b), soft callus formation phase (c), hard callus formation phase (d) and remodeling phase (e) (Figure 1.1.).

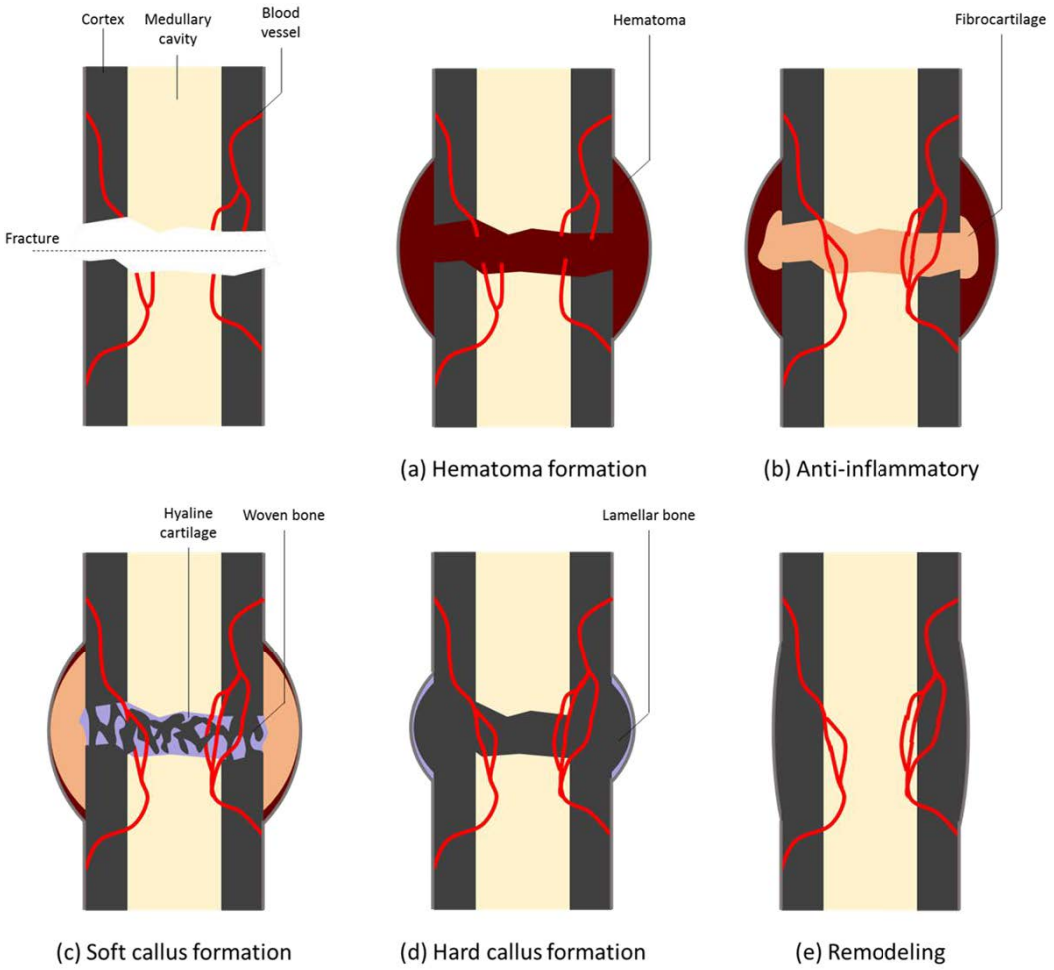

Figure 1.1. – The phases of secondary bone fracture healing process.

The different stages of healing involve multiple processes at different length- and time-scales. In the first hours after the fracture opening, a blood clot forms around the fracture (a). Then, a cascade of biological signals stimulates the attraction of immunological cells, macrophages and mesenchymal stem cells (MSC) inside the defect, where fibrocartilage starts to form (b). During the next stage of healing, called also reparative stage, the MSCs differentiate into chondrocytes and osteoblasts, promoting the formation of hyaline cartilage and woven bone and the formation of a soft callus starts (c). The subsequent phase of endochondral ossification promotes the formation of lamellar bone and the development of the hard callus (d). The final stage, which starts when the cortical bone fracture extremities are

bridged again, is characterized by a continuous formation and resorption of bone tissue to regenerate the original structure of the bone (e).

Due to the complexity of the entire process, it is not rare that a fracture does not completely heal in an acceptable time. During the last decades, numerous human and animal models have been used to investigate the factors that alter bone fracture healing leading to delays or non-unions [18]-[20].

1.2.2. Influence of mechanics on bone healing

Mechanics plays a major role in the regulation of bone healing. Many pre-clinical studies have demonstrated that bone healing progression is influenced by the mechanical environment [21]-[24]. Too rigid or too flexible fixations have been shown to result in delays in bone healing [22]-[24]. Moreover, bone fracture size has also been shown to influence healing. The dimension of the fracture determines interfragmentary tissue movement within the fracture and consequently the healing outcome [21].

1.2.3. Age-related alterations in the bone healing response

As in many other biological processes, aging has an effect on bone healing performance. Many of the healing-related processes are believed to get slower with increasing age and aging is associated with a reduction of the bone regenerative potential [25] [26], longer hospitalization stays [6] and increased risk of morbidities and mortality [27]. Changes in multiple cellular processes might contribute to the altered bone healing response with age. Reductions in the number of stem cells [28], migration [29] [30], proliferation or differentiation capacity [31] [32], altered re-vascularization [33], apoptosis [34] as well as altered tissue material properties [35] [36] have all been associated with a reduced regenerative capacity with increasing age. Most of these studies have investigated alterations in one or two cellular processes and have then proposed those processes as potential reasons for age-related

alterations in bone tissue formation during healing. However, the relative contribution of each of these factors to the overall healing progression remains largely unknown.

Aging has been also observed to influence the mechanical regulation of bone healing [37] [38]. Fixation stability plays a higher role in bone healing progression in younger animals [37]. At the cellular level, aging influences cellular mechanoresponse during bone remodeling [39]-[41]. In aged animals, reduced cellular response to mechanical stimuli led to increased bone resorption [39]. To date, it remains unknown how age-related alterations on cellular mechanoresponse influence tissue patterning over the bone healing process.

1.2.4. BMP-2 stimulated bone healing

Growth factors, as the name can suggest, are biological substances that can enhance the healing potential of the bone by promoting certain cellular processes, which help to accelerate bone restoration. Delivery of capsuled specific proteins and growth factors is clinically used to enhance fast bone fracture repair [42].

BMP-2 is a protein of the superfamily of the Transforming Growth Factor β (TGFβ), which is often used to treat critical bone fractures. Different *in vivo* studies have shown that critical size bone fractures treated with rhBMP-2 result in successful healing [43]-[45].

The effect of BMP-2 on bone healing is also affected by the mechanical conditions. Changes in fixation stability or mechanical stimulation have been shown to influence BMP-2 stimulated bone healing [45] [46]. Higher mechanical stimuli or low-stiffness fixator conditions favored mineralized tissue formation under BMP-2 treatment [45]-[47]. It remains unknown how local mechanical signals within the healing region influence BMP-2 stimulated bone regeneration.

At the cellular level, BMP-2 has been shown to stimulate the recruitment of MSCs [48] and bone cells [49], enhance cellular proliferation [50] and favorite chondrocyte maturation [51]. Cellular differentiation has also been shown to be influenced by BMP-2, where increased BMP-2 concentration has been shown to promote osteogenic [52] [53] and chondrogenic differentiation [54]. Moreover, the mineralization of the extracellular matrix has also been observed to be promoted by this growth factor [55]. However, to date, the relative contribution of BMP-2 stimulated cellular activities to bone regeneration remains largely unknown.

1.3. State of art

1.3.1. In silico models of bone fracture healing

Bone fracture healing is a complex process that is influenced by the mechanical and biological environments within the healing region. *In vivo*, it is very challenging to investigate the relative contribution of all the parameters that concur to regulate the healing process. As an example, the physical measurement of the mechanical stimuli inside the healing region is a challenging task to perform *in vivo*. However, it is possible to computationally model the mechanical environment using finite element (FE) techniques to predict the magnitude of the mechanical stimuli inside the region of interest. *In silico* studies on the mechanobiological regulation of bone healing have taken more and more a central role during the last thirty years [56]-[64]. Several *in silico* models have been developed with the aim of determining the range of mechanical stimuli driving tissue formation during the healing process. The effect of repeated application of axial load and bending inside the fracture gap was investigated *in silico* by Carter et al. (1998), who suggested that cyclic octahedral shear stress and principal tensile strain drive the tissue differentiation process [56] (Figure 1.2A). Prendergast et al. (1997) proposed a biphasic model to describe the relationship between biophysical stimuli and periprosthetic tissue formation [57]. They proposed a linear combination of tissue octahedral shear strain and interstitial fluid flow velocity as the mechanical stimuli sensed by the cells to drive their differentiation [57] (Figure 1.2B). Another model to describe the effects of mechanics on bone healing was proposed by Claes and Heigele (1999) who compared bone formation patterns over the course of healing with mechanical signals inside the callus, predicted using FE techniques [58]. They proposed that intramembranous bone formation occurs for strains smaller than +/- 5% and hydrostatic pressures smaller than +/- 0.15 MPa [58]. Endochondral ossification was associated with compression larger than -0.15 MPa and

strains within the +/- 15% range [58] (Figure 1.2C). More recently, Burke et al. (2012) proposed another theory which describes tissue differentiation as a function of substrate stiffness and oxygen presence [63]. Cartilage is proposed to more likely form in hypoxic regions and, as the oxygen tension increases, cartilage is proposed to calcify and to undergo endochondral ossification [63] (Figure 1.2D).

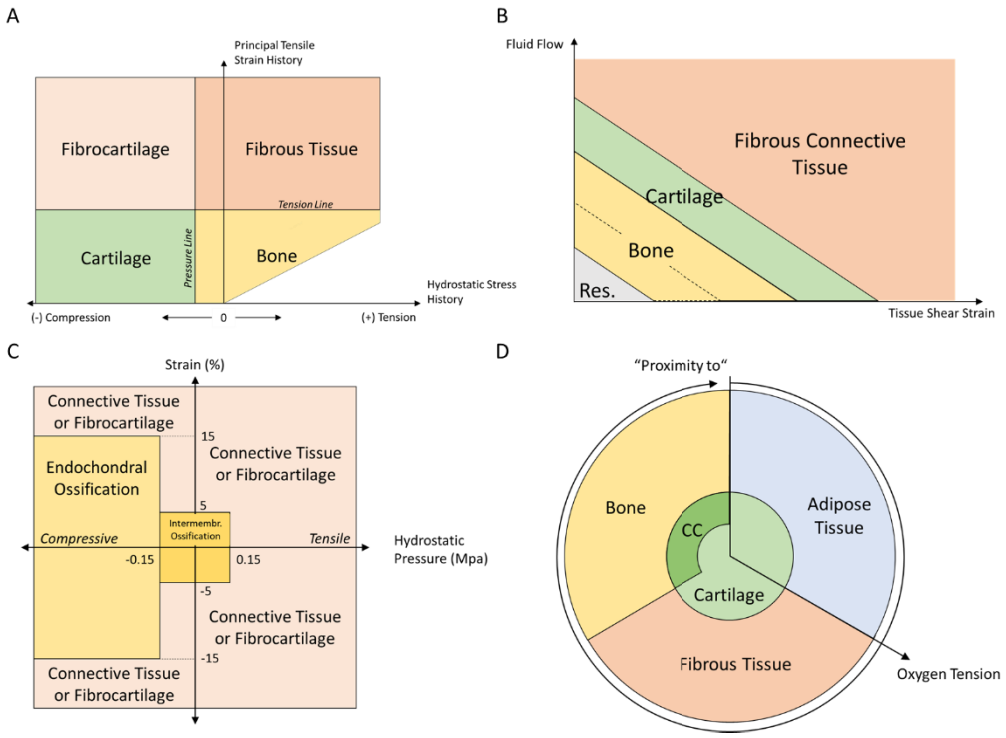

Figure 1.2. – Mechano-regulatory rules to describe cellular differentiation in bone healing. A: Carter et al. (1998) [56] B: Prendergast et al. (1997) [57] C: Claes and Heigele (1999) [58] D: Burke et al. (2012) [59]. CC: Calcified Cartilage.

Thereafter, the ability of these mechanical stimuli to predict bone tissue formation during healing has been tested in several *in silico* studies. Isaksson et al. (2006) compared the ability of different mechanical stimuli to predict bone healing progression in a sheep animal model and showed that deviatoric strain (tissue deformation) alone could accurately explain tissue patterning over the course of bone healing [65]. Tissue deformation was shown to play a main role in influencing the interfragmentary mechanical environment in initial phases of bone healing also by Epari et al. (2006) [66]. In that study, FE

methods were used to investigate the biophysical stimuli inside the fracture gap under different mechanical conditions. The contribution of volumetric stimuli, as hydrostatic pressure in Claes et al. (1999) model [58] and fluid flow velocity in Prendergast et al. (1997) model [57] were proposed to be minimal in the regulation of tissue formation [66]. Geris et al. (2010) investigated *in silico* the role of mechanical overload on the occurrence of non-unions. In detail, the multiscale computer model simulated the overloaded mechanical environment and the alteration of biological processes. It showed that mechano-alteration of both angiogenesis and osteogenesis led to non-union, while alteration of angiogenesis alone was not enough to explain compromised healing [67]. Steiner et al. (2010) used finite element analysis (FEA) to investigate which mechanical stimuli regulates fracture healing under different loading conditions (axial compression, torsion, shear, bending). They showed that distortional and dilatational strains better predict the course of healing in ovine bone [64].

To investigate the role of the mechanical environment in the healing process, multiple case scenarios of bone fracture healing have been simulated [68]-[70]. Interfragmentary mechanical environment and, consequently, the healing outcome were predicted to be affected by fracture gap size [68], external mechanical loading [69] and fixator stiffness [70]. Mechanobiological computer models have also been used to investigate inter-species differences in the mechanical regulation of bone healing. Several studies have proposed interspecies differences in the mechanical regulation of bone healing between small and large animal models [61] [71], however it remains unknown if differences also exist between different small size animal models (e.g. between mouse and rat).

Although many *in silico* studies have investigated the influence of mechanical and/or biological factors on uneventful healing conditions, very few studies have focused on compromised conditions, i.e. situations where the bone would not naturally regenerate. For example, critical size defects were only approached in the study by Carlier et al. (2014), where they focused on the

influence of biological factors (vascularization, growth factors) on healing outcomes [72]. The model showed that healing was impaired in large interfragmentary gap conditions due to insufficient vascularization of the callus [72]. The influence of mechanics on large bone defect healing has never been investigated before.

Mechanobiological computer models have been previously developed to investigate bone defect healing under BMP-2 stimulation [73] [74]. Tissue formation [50] [75], cellular migration [48] [49] and proliferation [50] [76] were simulated to be enhanced by the presence of BMP-2, which was locally consumed and produced by the cells [77] [78]. The mechanistic model of Moore et al. (2014) investigated the spatiotemporal dynamics of BMP-2 and periosteum progenitor cells in the overall process of defect healing [73]. Ribeiro et al. (2015) model gave an insight of the BMP-2 contribution on the promotion of bone regeneration in a large defect [74]. However, this study limited the healing region to the intercortical region, omitting any bone formation in the periosteal and endosteal regions. In addition, the bone remodeling process and the role of mechanical signals in the regulation of BMP-2 stimulated healing were not investigated by this model.

Early computer models of bone healing were limited to processes at the tissue scale. More and more, in the last decades, multiscale computer models have been developed to investigate bone healing taking into account biological processes at the cellular level and the interactions between multiple length- and time-scales [79]. Computer multiscale models permit a complete overview of the mechanobiological phenomena, extending the investigation to the mechanisms which interact at smaller levels. Processes like cellular migration, growth factor diffusion and angiogenesis have been simulated in this context [59] [80]-[83].

In summary, multiscale computer models have been used to understand the regulation of bone healing at different length- and time-scales. Numerous *in silico* models were developed to investigate mechanobiological “rules” behind the bone healing process and to investigate how mechanical signals regulate

biological parameters. Most of the models iteratively interact in a double-way, predicting how changes in tissue patterning influence the mechanical environment and, vice versa, how mechanical stimuli further influence tissue formation. However, these models have rarely been used to investigate the mechanisms which compromise bone healing under critical conditions. The aim of this project was to exploit computer models to investigate compromised situations to parametrically individuate which factors concur in altering the bone healing process.

1.4. Thesis objectives

In the last decades, more and more pre-clinical studies have focused on understanding the mechanisms behind compromised bone healing conditions. These studies have shown that factors like aging or the bone defect size seriously compromised bone healing potential, often leading to delayed or non-unions. However, *in vivo* studies are usually limited to histological observations at the tissue level and the measurements of very few biological cellular processes, if at all. In this thesis, a combined *in vivo*/*in silico* approach was used to investigate challenging healing conditions with the aim of identifying key factors playing a major role in the alteration of the mechanobiological regulation of bone healing at multiple length- and time-scales. Specifically, this work focused on compromised conditions due to aging and large defects. For this reason, this study focused on the following two objectives:

Objective 1: To investigate the influence of age-related alterations at the cellular level in the mechanical regulation of bone healing;

Objective 2: To investigate the mechanical regulation of large bone defect healing and its alteration under BMP-2 stimulation.

Objective 1 was achieved by using a computer model to simulate bone healing in adult and elderly mice under two different fixation stiffness (rigid and semirigid). To investigate age-related differences in bone healing progression, observed *in vivo*, between adult and elderly mice, cellular activities (migration, proliferation capacity, etc.) were downregulated, *in silico*, in a design of experiments (DOE) analysis to determine the most influential parameters. Histological data from bone healing progression in adult (26-week old) and elderly (78-week old) mice, under both rigid and semirigid fixation, were used to validate *in silico* tissue patterning at 7, 14 and 21 days after the fracture opening.

Hypothesis 1: Experimental data of bone healing in mice showed that fixator stiffness has a greater influence in adult than in elderly mice. I hypothesized that the MSC capacity to respond to mechanical stimuli can explain *in vivo* observations.

To achieve objective 2, a bone defect in rat was modeled to reproduce *in silico* the case studies from a previous *in vivo* study that investigated the potential of external mechanical loading to enhance the efficacy of BMP-2 treatment [45]. Multiscale modeling allowed to explore the mechanism behind the capacity of exogenous BMP-2 to favor bridging of critical fracture gap in acceptable healing periods. The model investigated the cellular level parameters that enhanced healing under BMP-2 and mechanical stimulation.

Hypothesis 2: The BMP-2 dose-dependent effect at the cellular level should explain the characteristic healing patterning observed in treated conditions (periosteal bridging after 2 weeks post-operation). I hypothesized that the simulation of BMP-2 dynamics can be a valuable resource to individuate the biological features which most contributed to promote the healing.

1.5 Thesis outline

In **Chapter 1** a brief introduction to the clinical relevance of this thesis is presented. Thereafter, the bone healing process is described followed by a brief overview of the studies that motivated this work. Finally, attention is addressed to studies that involve the use of multiscale computer models to investigate the dynamics of bone healing and the different mechanobiological factors involved. At the end of the chapter, the objectives of this thesis are reported.

In **Chapter 2** a detailed explanation of all the tools used to achieve the aims is presented. The properties of the FE and agent-based computer models involved in the simulation of bone healing in mice and rats are reported here. In addition, all the set-ups of the case studies investigated with the computer models are described.

In **Chapter 3** the results of all the studies forming part of this thesis are stated. All the results are reported in tables and plots with additional description of the most interesting aspects. An analysis of the results is provided in addition with the discussion of the eventual limitations of the models.

In **Chapter 4** the conclusive statements regarding the results of each study and their clinical contribution are reported. Moreover, potential improvements and aspects which should be addressed in future studies are described.

2

MATERIALS & METHODS

2.1. Finite element models

The mechanical environment within the fracture region plays the main role in the regulation of bone healing. The determination of the mechanical stimuli within the callus region during the healing process is challenging *in vivo*. FEA was used in this work to determine the mechanical signals within the healing region during healing progression. The three-dimensional geometry of the bone osteotomy was developed and material properties were assigned to the various parts of the model (fixator, bone cortex, medullary canal and callus). Forces and boundary conditions were applied to the meshed geometry to simulate the mechanics acting on the bone. The computational analysis of the FE model was performed in a machine with 4 GB RAM and Intel Core I5-4590 CPU @ 3.30 GHz processor. The FE models were created in *Abaqus/CAE v. 6.12-2* [85] where a design tool allowed to generate the three-dimensional geometry of the model. Within the same software, it was possible to assign the material properties, the loadings and the boundary conditions. *Abaqus/CAE* recognized the geometry of the model and generated an optimized node distribution within the entire volume, which was used to create a mesh of elements with user-defined dimensions. All the characteristics of the model were saved into an input file (*.inp*) that was then used in the following steps to perform the FE analysis with *Abaqus/standard v. 6.12-2*. The outputs of the analysis were two: a text file (*.dat*) with a tabular structure, which contained the predicted mechanical stimuli within every node of the model, and an output database file (*.odb*) that allowed the visualization of the mechanical stimuli distribution within the model geometry in *Abaqus/viewer v.6.12-2*.

2.1.1. Geometry of the models

In this work, bone healing was investigated *in silico* in two different animal species: mouse and rat. Mouse osteotomy bone healing models stabilized with two different external fixators (rigid and semirigid) were developed to investigate the mechano-regulation of bone healing in mice and how aging

influences the mechanical regulation of bone healing. Rat large bone defect osteotomy models under critical healing conditions were created to investigate the mechanical regulation of BMP-2 stimulated bone healing. Both *in silico* models aimed to replicate experimental conditions on *in vivo* studies [45] [86].

Mouse osteotomy model

The three-dimensional geometry of the mouse osteotomy model was designed by using the dimensions that were measured *in vivo*. The bone geometry was simplified as a hollow cylinder with an internal cavity to reproduce the bone marrow. The external and internal radii of the cylinder are 0.75 mm and 0.55 mm, respectively. Thereby the model is characterized by a 0.2 mm wide bone cortex. The cylinder length was set as 15 mm and an osteotomy of 0.5 mm was opened in the middle to simulate *in vivo* conditions. The callus domain was designed as a rotational ellipsoid. The optimal callus width in the central region was chosen in an additional study of the effect of callus size on the healing outcome predictions (*Appendix A.1.*). The optimal radius was identified with a value of 2 mm. The callus domain was limited to a length of 3.5 mm in the axial direction. Mouse osteotomized bone and callus domains were merged together to create the global model that is represented in Figure 2.1.

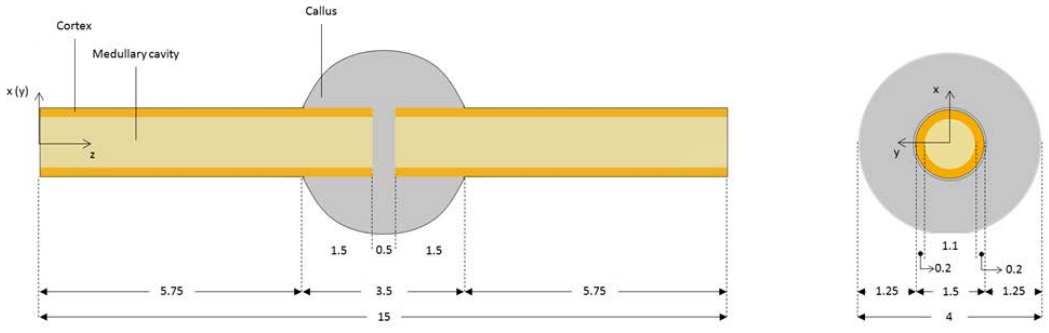

Figure 2.1. – FE model geometry of a 0.5 mm mouse osteotomy. Lateral (left) and axial (right) views are here reported with all the dimensions (in mm) and references to the different parts of the model.

Mouse rigid/semirigid external fixator

To investigate the influence of mechanics on bone healing in mice, two different external fixators were used to stabilize the osteotomy: rigid and semirigid. To reproduce the same conditions investigated *in vivo* [86], three-dimensional FE models of the rigid and semirigid external fixators were created with the same dimensions as the ones used in the experiments. The rigid and the semirigid fixators were both composed of a fixator structure (a bar) and 4 nails to connect the bar with the bone. The difference between the two fixator stiffness lied in the geometries of the bar structure. All the dimensions were measured from the external fixators used *in vivo* and are reported in Figure 2.2.

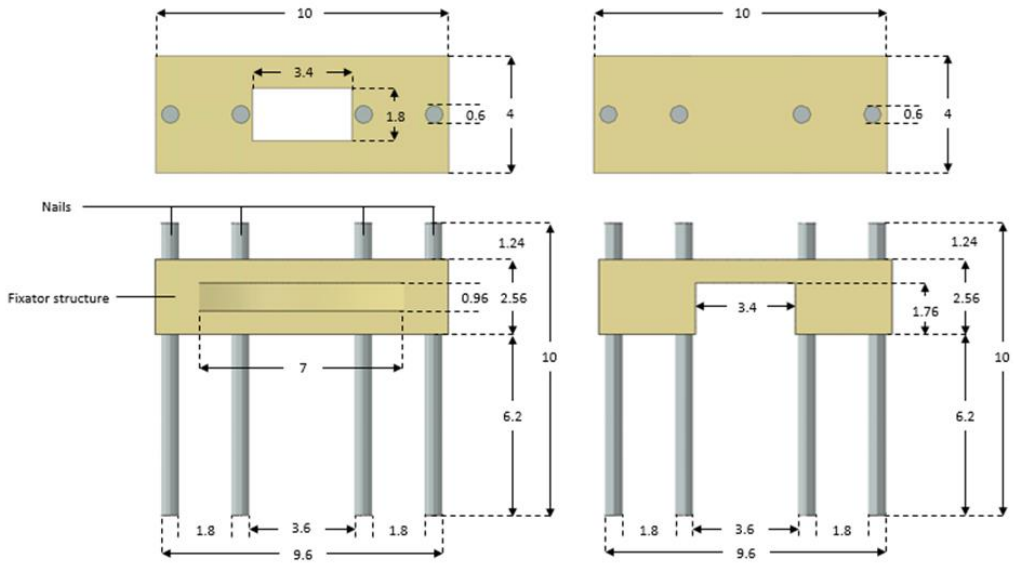

Figure 2.2. – FE model geometry of the two external fixators used to stabilize mouse bone osteotomies (right: rigid, left: semirigid). Axial (top) and lateral (bottom) views are here reported with all the dimensions (in mm) and references to the different parts of the model.

The connection of the fixators to the mouse osteotomy models was provided by the presence of four nails. The nails geometries were approximated to a cylinder and their size was measured from the surgical nails used for the *in vivo* experiment. Each nail had a diameter of 0.6 mm and a length of 10 mm

(Figure 2.2.). The distance between the nails was also measured from the *in vivo* setup (Figure 2.2.). Mouse osteotomy model and rigid/semirigid external fixator were assembled together as shown in Figure 2.3.

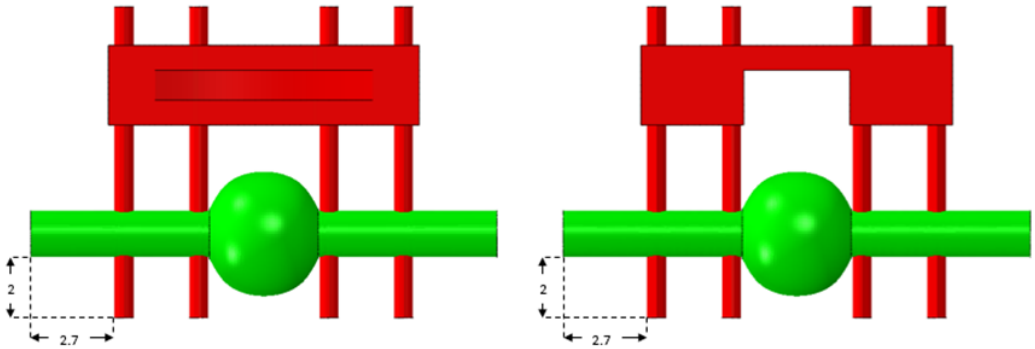

Figure 2.3. – FE assembly of the model under rigid (left) and semirigid (right) fixator. Mouse osteotomy model (green) and fixator (red) relative distances are reported in mm.

The stability provided by the fixators was validated *in silico* by simulating an axial stiffness test as the one performed by Kruck et al. (2018) [86]. For the realistic setup of the test, the callus domain was removed from the bone model. A compression force of 0.82 N was homogeneously distributed on one surface of the bone cortex, while the other extremity was encastred. The mean displacement of the bone surface at the point of force application was obtained. The ratio between the applied force and the displacement was determined as the axial stiffness of both fixators *in silico*. The results were compared with the analogues measured *in vivo* [86].

Rat osteotomy model

The FE model of the rat osteotomy was obtained from the previous *in silico* work of Checa et al. (2011) [61]. The bone model was approximated as a hollow cylinder with internal radius of 1 mm and cortical bone width of 1 mm. A total bone length of 30 mm was imposed and the osteotomy was opened in

the middle point. The original model was used to investigate mechano-regulation in a small osteotomy (1 mm gap), in this study the defect was widened to 5 mm to simulate a large bone defect. The callus domain was designed as a 6 mm axis ellipsoid. A callus length of 7.2 mm was imposed in the longitudinal direction. These dimensions prevented overlap with the elements that characterized the external fixator and allowed a wide investigation of the mechanics in the surroundings of periosteum. The rat osteotomy model and its dimensions are reported in Figure 2.4.

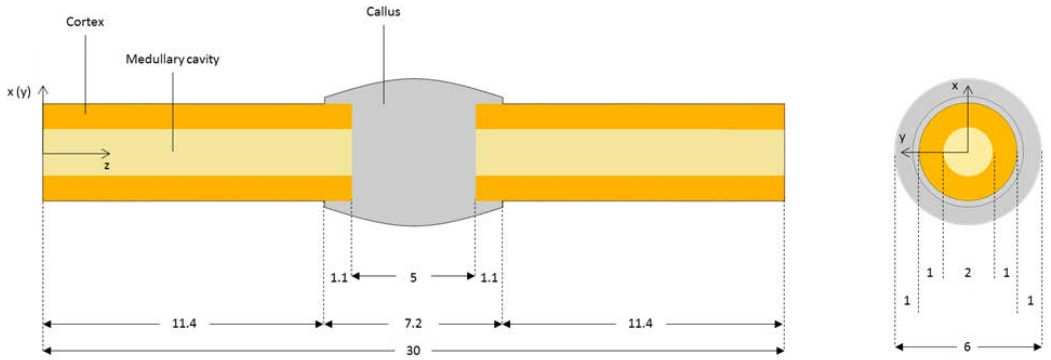

Figure 2.4. – FE model geometry of 5 mm defect model in rat. Lateral (left) and axial (right) views are here reported with all the dimensions (in mm) and references to the different parts of the model.

Rat external fixator

The stabilization of the defect in the rat osteotomy model was provided with an external fixator characterized by larger dimensions compared to the one used for the mouse osteotomy model. The same fixator was used in all the case studies of rat osteotomy healing investigated with this model. The structure of the fixator was composed of two parts with the shape of a parallelepiped, each of which holds two nails over a total of four. An intermediate fixator bridge connects the two parts to form a unique fixator structure. The bridge was removed under certain conditions, as it also happened during the experiments [45]. The dimensions of the fixator are reported in Figure 2.5.

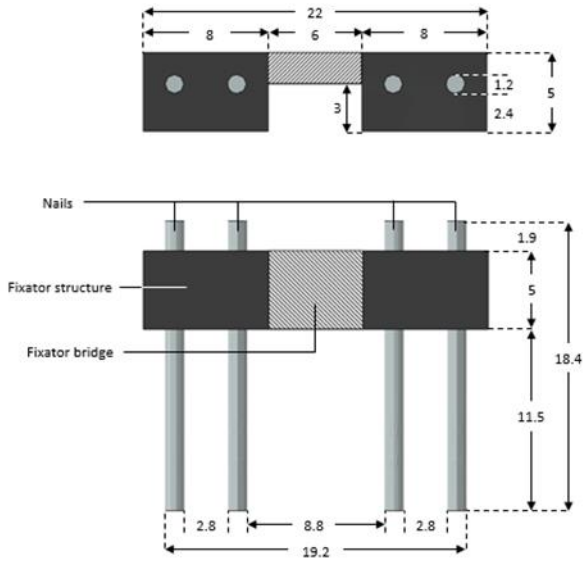

Figure 2.5. – FE model geometry of the external fixator used to stabilize the rat osteotomy. Axial (top) and lateral (bottom) views are here reported with all the dimensions (in mm) and references to the different parts of the model.

Four nail models were created to connect the external fixator to the bone. In order to reproduce the dimensions of the surgical nails used in the experiments, four cylinders with 1.2 mm radius and 18.4 mm axial length were modelled. The distance between the center of the nails was measured *in vivo* and reproduced in the computer model (Figure 2.5). Rat osteotomy model and the external fixation were assembled together as shown in Figure 2.6.

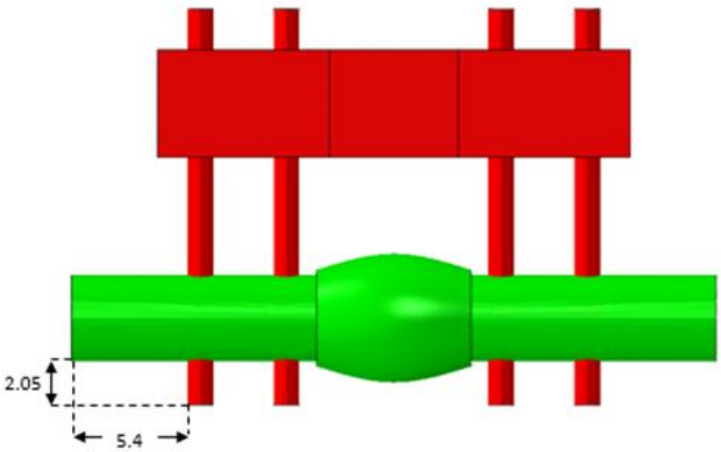

Figure 2.6. – FE assembly of the model. Rat osteotomy model (green) and fixator (red) relative distances are reported in mm.

2.1.2. Material properties

The geometry of the models alone was not enough to describe the mechanics within the healing region, the material properties of the different parts of the models had to be defined. *Abaqus* allowed to assign to each element of the FE models specific material mechanical properties to describe their behavior under mechanical stimulation. In both mouse and rat models, material properties that did not change through the entire bone healing simulation were defined for the bone cortex, the medullary cavity, the external fixator and the nails. The callus domain was assigned with material properties that dynamically changed with time, simulating in this way bone healing progression. All the parts of the rat bone defect model were considered to be biphasic consisting of a solid and a liquid phase, while the fixator was characterized by the only solid phase. All the materials were considered linear elastic.

Initial material properties

As described above, the bone structure was approximated as a hollow cylinder in both mouse and rat models. The external structure represents the bone cortex, therefore cortical bone mechanical properties were assigned to it. The inner structure represents the medullary cavity, therefore bone marrow material properties were assigned to this region. It was hypothesized that the callus domain is initially filled with granulation tissue [87]. Material properties representative of the mechanical behavior of granulation tissue were hence selected to describe this part of the model. The mechanical properties of Polyether-ether-ketone (PEEK) were assigned to all the external fixator structures. The difference in the stiffness of the devices was only provided by their geometry, not by the mechanical properties of the material. The nails were characterized by the material mechanical properties of titanium. The initial distribution of the materials in both the mouse and rat osteotomy models is shown in Figure 2.7.

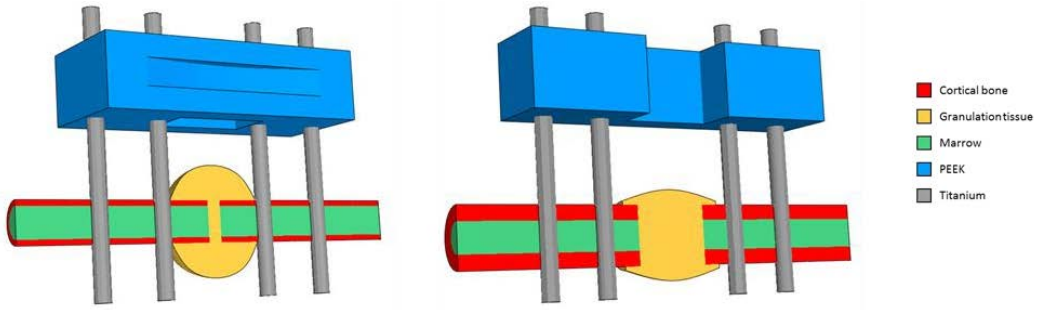

Figure 2.7. – Material assignment to the different parts of the mouse (left) and rat (right) osteotomy models. The same materials were defined for both the models in this study: cortical bone (red), granulation tissue (dark yellow), marrow (green), PEEK (blue) and titanium alloy (grey).

Each material was described in *Abaqus/CAE* and their properties were edited as elastic and permeable. Moreover, all the assigned material mechanical properties were considered isotropic. The biphasic nature of the model required to assign both solid and fluid characteristics to the different materials. For the properties describing the solid part, Young's modulus and Poisson's ratio were specified for each material. In addition, to consider the fluid phase contribution to the mechanical properties of the different tissues, interstitial fluid was simulated to flow through the tissue pores. The bone, the medullary canal and the callus tissues were characterized by different permeability and bulk modulus. The permeability describes the pressure gradient required by the interstitial fluid to diffuse through the material at a certain flow speed. The bulk modulus describes the fluid resistance response to compression stress. In this model, the bulk modulus was assigned also to the solid part of the material, under the name of grain bulk modulus. Mechanical properties of water were chosen to describe the interstitial fluid. The specific weight of the interstitial fluid was considered 9.8×10^3 N m^{-3} and its inertial drag coefficient 0.14. All the values were assigned following Checa et al. (2011) [61] and are summarized in Table 2.1.

		Granulation tissue	Cortical bone	Marrow
Solid phase	**Young's modulus** *MPa*	0.2	5000	2
	Poisson's ratio -	0.167	0.3	0.167
	Bulk modulus grain *MPa*	2300	13920	2300
Fluid phase	**Permeability** $10^{-14}\ m^4\ N^{-1}\ s^{-1}$	1	0.001	1
	Bulk modulus fluid *MPa*	2300	2300	2300

Table 2.1. – Material properties used to describe the mouse and rat osteotomy models.

The mechanical properties of the external fixator parts were taken from matweb database [88]. Monophasic, isotropic and elastic linear properties were assigned to the fixator structure and to the nails. PEEK was modelled with Young's modulus of 3800 MPa and Poisson's ratio of 0.38. The titanium, material assigned to the nails, was assigned Young's modulus of 170000 MPa and Poisson's ratio of 0.33.

2.1.3. Mesh characterization

To perform FEA, the models created to simulate the geometry and the mechanical properties of the osteotomized bones were meshed. Meshing consists in the creation of nodes spread at average user-defined distance within the entire volume of the FE model. Each node then characterizes the position of one of the vertices of one or multiple elements, which have the role to reproduce the volume of all the parts that characterize the models. In order to follow the curvature of the bone healing models, the distribution of the nodes was adapted to provide smoothness to the meshed model geometry. For this study, 3-dimensional 8-node brick poroelastic elements (C3D8P) were

chosen. Those elements had a hexahedron shape, characterized by 6 faces, 12 edges and 8 vertices (Figure 2.8.).

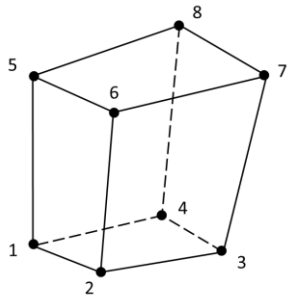

Figure 2.8. – C3D8 element shape.

The 3D shape of the C3D8P elements was observed to smoothly adapt to the geometry of the model. The fineness of the mesh was the key to obtain an accurate reproduction of the global structure of the bone osteotomy model, which was characterized by rounded surfaces. To increase the quality of the mesh, small element dimensions were required at the expense of a high computational cost. To find a compromise between the mesh refinement and the computational complexity, different element average edge sizes were investigated (*Appendix A.2.*). The parametric investigation showed that the best compromise was obtained in the mouse model when a 0.10 mm average edge length characterized the elements within the callus domain. The same mesh as in the previous *in silico* work of Checa et al. (2011) [61] was kept for the rat defect model, with element average size of 0.25 mm inside the callus domain. As the rest of the model was meant to provide the structure and was not used to investigate the mechanical behavior, larger elements were used (average size in mouse model: 0.18 mm, average size in rat model: 0.50 mm) to reduce their impact on the computational complexity. The mesh optimized for the mouse model with 0.5 mm osteotomy gap stabilized by rigid external fixator was characterized by 280,093 nodes and 263,087 elements. The 0.5 mm gap mouse osteotomy model stabilized with semirigid external fixator was characterized by 295,187 nodes and 278,874 elements. The rat large defect model was meshed with 74,765 nodes and 68,837 elements.

2.1.4. Gait load and boundary conditions

The simulation of the mechanical stimuli within the osteotomy gap was obtained *in silico* as the result of habitual gait both in mice and in rats. A combination of a compression load and a bending moment was used to describe this habitual load. In both, the mouse and rat models, the gait loading was simulated by the application of the mechanical loads in one extreme of the bone and imposing an embedding boundary condition on the other. The boundary condition fixed the non-loaded extremity to allow the distribution of the compression and bending stresses through the entire bone shaft. The loading magnitudes were obtained from the literature [60] and scaled to the mass of mouse and rat. Body weight (BW) of mouse was assumed equal to 0.025 Kg in this model, as the average value measured in experimental samples. Rat average BW was measured to be 0.25 kg. Both models were loaded with a combination of 6 BW compressive force and 10.7 BW mm bending moment at the femoral mid-shaft [60]. Compression force was uniformly distributed on the whole cortex surface of the loaded extremity of the bone model. The orientation of this force followed the longitudinal axis of the bone. Mouse bone cortex cross-sectional area was 0.8 mm^2 and, in order to simulate 6 BW (equal to 1.5 N compressive force), a 1.8 MPa uniformly distributed pressure was applied on the surface. Rat bone cortex cross-sectional area was 9.4 mm^2, in order to simulate 6 BW (equal to 14.7 N compressive force) a 1.6 MPa uniformly distributed pressure was imposed on the surface of the bone. Two bending moments were imposed on the bone shaft by applying concentrated shear forces in the center of the loaded bone surface. Both bending forces were perpendicular to the longitudinal axis of the bone. One bending moment generated tension on the surface of the bone that faces the external fixator. For this reason, the concentrated force that produced this moment was oriented in the medial direction (fixator on the lateral side). The bending load was determined to obtain a bending moment of 10.7 BW mm on the intact bone when measured at the femoral mid-shaft point. In the mouse model, this point is 7.5 mm distant from the moment application

point. To achieve this magnitude on the mouse model, a concentrated force of 0.3 N was applied. In the rat model, the center of the mid-shaft was distant 15 mm and a concentrated force of 1.8 N was necessary. A second moment was created on the model to generate bending in the antero/posterior direction. To generate this moment, a force oriented in the anterior direction was created with the same magnitude of the concentrated force that generated the medial bending previously described. As both concentrated forces were used to simulate bending, the application point of each force was constrained with the loaded surface. In this way, the effect of the concentrated force was extended to the whole loaded surface and not to the single point. The non-loaded extremity of the bone was fixed with clamped boundary conditions. The clamp is a superficial boundary condition that embedds (fixes) all the nodes that belong to the bounded surface. Those nodes were not allowed to move from their initial position in any of the 3 axis directions. Moreover, all the element edges that lay on the embedded surface were constrained to maintain the same length. The clamp allowed the distribution of the stress on the bone shaft as a response to the imposed mechanical loadings. An additional boundary condition was imposed on the external surface of the callus domain: the interstitial fluid was not allowed to flow through the callus domain surface. This second boundary condition was created assigning 0 μm s^{-1} to the fluid flow velocity on all the points that belonged to the callus domain surface. The schematic distribution of the loads and boundary conditions applied to the models is shown in Figure 2.9.

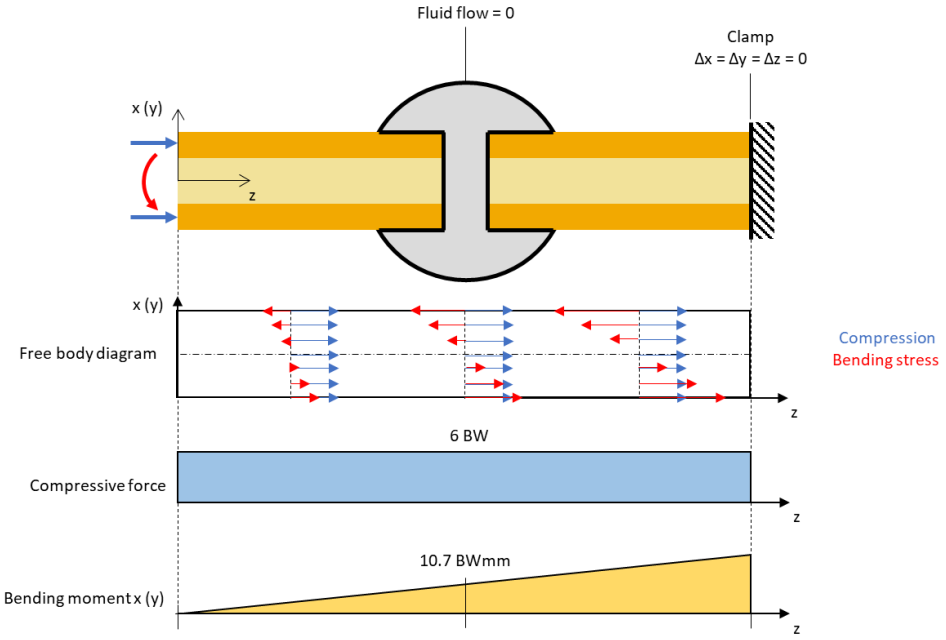

Figure 2.9. – Schematic representation of the loads and boundary conditions applied to the mouse and rat healthy bone FE models. Free body diagram, compressive force and bending moment are reported through the axial direction.

In the rat model, the *in vivo* case study was reproduced, where external mechanical loading was applied through the external fixator to investigate the contribution of mechanics to bone healing. To replicate the experimental scenario, the model loading scenario was integrated with a weekly addition of 0.5 mm compressive displacement (10% of the osteotomy gap) [45]. The displacement was imposed on the surface of the external fixator and it was oriented in axial direction to generate compression. In addition, to reproduce the experimental settings, the fixator bridge of the rat external fixator was removed during the application of this load (Figure 2.10.).

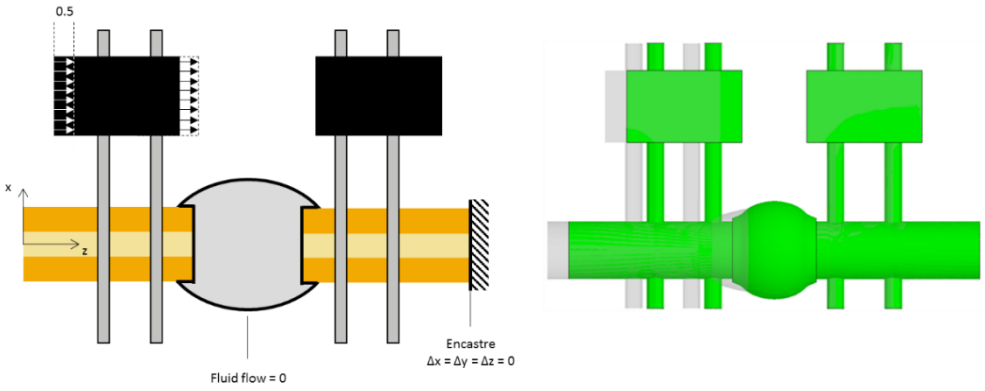

Figure 2.10. – Schematic distribution of loads and boundary conditions during the weekly displacement in axial direction under external mechanical loading treatment in rat defect healing. The effect of the displacement is shown in the image on the right side (grey: initial condition, green: displacement effect).

2.2. Cellular distribution agent-based model

The multiscale platform used in this project couples a FE model and two agent-based models to investigate bone healing progression taking into account mechanical and biological factors at different scales. An agent-based model is a three-dimensional matrix of points (agents) with specific coordinates, according to their relative position. To each agent of the matrix, three coordinates and one parametric value were associated. Those four values together described the distribution in the Cartesian space of a certain parameter. In this project, one agent-based model was used to investigate the distribution of the cells within the callus domain. Each agent of the agent-based was characterized by a parametric value that described the phenotype of the cell associated with that agent, in addition to the three coordinate values needed to identify its position in the space. The aim of the agent-based model was to dynamically simulate the spatial distribution of all the cells within the callus and to distinguish between the different phenotypes. In the mouse model, the cellular distribution agent-based model was characterized by 400 (x), 400 (y) and 350 (z) agents in the three Cartesian directions, for a total of 56,000,000 agents. In the rat models, the cellular distribution agent-based model was characterized by 600 (x), 600 (y) and 880 (z) agents for a total of 316,800,000 agents. In both mouse and rat models, 10 μm diameter size was associated with each agent to represent one single cell. To merge it with the FE model, the cellular distribution agent-based model was moved to couple its center with the center of the callus domain. Moreover, the agent-based model was rotated to orient its z-axis with the longitudinal axis of the bone. The agent-based model dimensions were decided in order to fit with the dimensions of the FE callus. Only in the rat model, the agent-based model exceeded 0.8 mm longitudinally in both proximal and distal osteotomy extremities to extend the investigation to a larger section of the medullary cavity. In Figure 2.11. the relative position between the agent-based model and the mouse and rat bone healing FE models is presented.

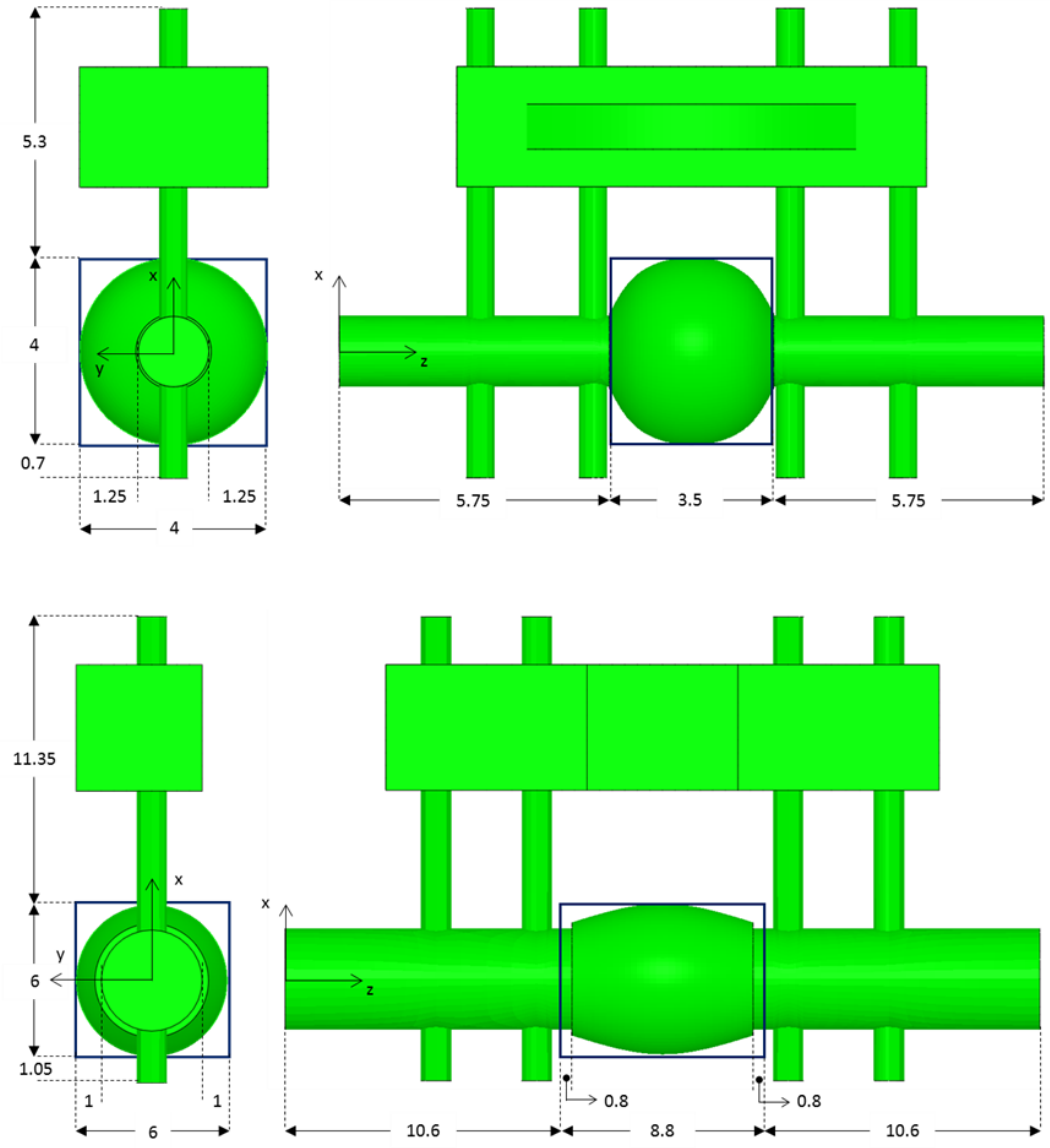

Figure 2.11. – Dimensions in mm of the cell distribution agent-based model (blue box) and its relative position compared to the FE model of mouse osteotomy (top) and rat defect (bottom).

The analysis of the dynamics within the agent-based model was performed by creating a *C++* project in *DEV/C++* [89]. The project consisted in the main file (*main.cpp*) that called subordinated *.cpp* files to perform the analysis. By running the main, the 3D agent-based model was generated and initialized in first instance. Then an iterative loop simulated the biological activities within the agent-based model by updating the distribution of cells at every iteration.

The execution of the simulation was run with an *.exe* file generated from the compilation of the project through *G++* (GNU Compiler Collection) [90].

2.2.1. Cell phenotypes

In the cellular distribution agent-based model, five different cell phenotypes were taken into consideration both for mouse and rat models. A parametric value was associated with each kind of cell: 1–MSC, 2–mature osteoblast, 3–immature osteoblast, 4–chondrocyte, 5–fibroblast. This value is the parameter associated with each agent to identify the phenotype of the cell in a specific position. The absence of a cell in a specific agent was tagged with value 0. The distribution of those parametric values in the three-dimensional space gave an overview of the dynamics of the cells involved in the healing simulation. Some agents were excluded from the analysis as they were outside of the FE model geometry. In addition, the positions that overlapped the bone cortex were excluded from the investigation. A buffer value was assigned to the parameter value of all the positions that were not included in the investigation, in order to consider them unavailable.

The agent matrix was initialized in a preparation step, to reproduce the cell distribution situation immediately after surgery. Only MSCs were seeded in the agent matrix during the initial step. According to Fan et al. (2008), the MSCs were initialized by filling 30% of the agent matrix available positions within the marrow cavity and the periosteum zone [91]. The algorithm counted the number of available positions on the agent-based model that overlapped the medullary cavity of the bone. This quantity was multiplied by 0.3 to quantify the number of cells to seed. The MSCs were seeded randomly within the medullary volume by choosing a random combination of position coordinates. If the random position was not occupied by a previous seeded cell, the cell phenotype parameter relative to that position was changed to 1–MSC. The seeding was done iteratively one cell per iteration until 30% of the medullary space was occupied. An analogous procedure was followed to seed the

periosteum. In this model, the periosteum was considered the volume that surrounds the external surface of the bone cortex with the width of a single cell (10 μm). After counting the number of available positions in the periosteal zone, 30% of these positions were randomly selected and seeded with MSCs. Figure 2.12. shows the regions within the medullary cavity and the periosteum where MSCs were seeded in mouse and rat models.

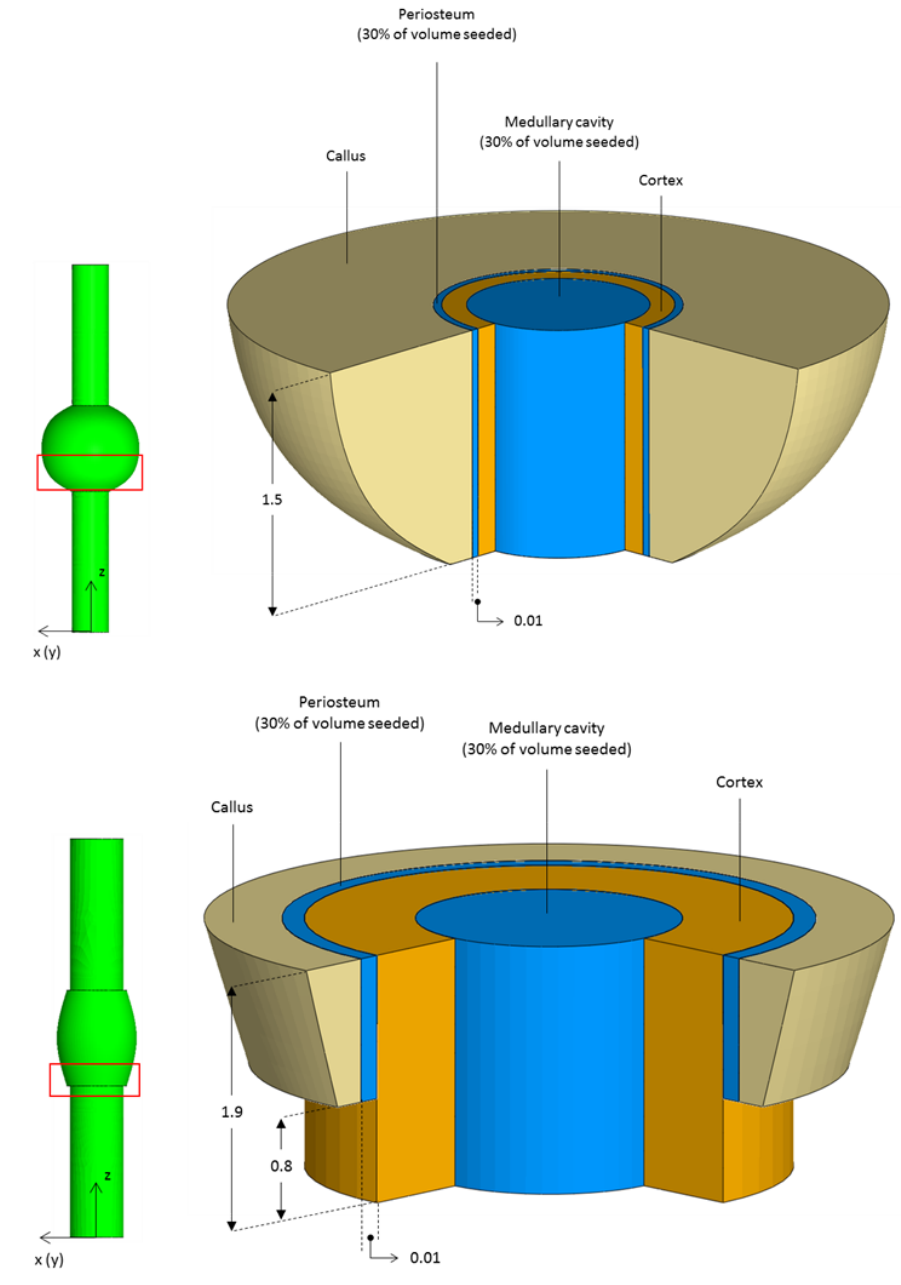

Figure 2.12. – Initial MSC seeding zones (blue) in mouse (top) and rat (bottom) osteotomy models. Dimensions in mm.

To each position of the cellular distribution agent-based model occupied by a cell a supplementary parameter that represented the age of the cell (in days) was assigned. Each agent-based position was then characterized by five parameters (*x*, *y*, *z*, phenotype, age). The value was initialized to 1 for every MSC seeded in the initial stage. This age value was increased by 1 every 24 hours (after 1 complete iteration in the mouse model or 12 complete iterations in the rat model). Cellular age was used to set a maturation threshold, i.e. only cells with an age above that threshold were considered ready to differentiate.

2.2.2. Cellular activities

The biological dynamics at the cellular level was investigated with the agent-based model by tracking how the positions of the cells and their phenotype iteratively changed through the bone healing process. All the cells in the model were subject to different ratio-dependent activities: migration, proliferation, differentiation and apoptosis. Multiple algorithms were implemented in the *C++* code to update the cell positions and simulate their change of phenotype. As previously mentioned, every iteration in the mouse model simulated the biological events of 1 day, while the rat model was characterized by 2 hours iterations. The reduction of iteration time favored the precision of simulated BMP-2 dynamics, which only was investigated in the rat model, at the expense of computational time. In the next paragraphs, the cellular activity ratios are reported in day^{-1} ($\mu m\ day^{-1}$ for migration ratio) to fit one iteration in the mouse model. To convert the activity ratios to one iteration in the rat model, the values were divided by 12.

Cell migration

Cellular migration is a process that characterizes the ability of the cells to move within the extracellular matrix. Some cell phenotypes are capable of moving in the space by creating protrusions and generating traction forces. Migration

plays an important role in bone healing as cells like MSCs are required to move to the osteotomy opening to trigger the events that result in its healing. In the model, cellular migration allowed MSCs to move to the osteotomy gap, differentiate and then form the different tissues. For this study, cell migration was an exclusive capacity of MSCs and fibroblasts [61], since chondrocytes and osteoblasts have very limited migration potential [92]. Their migration speeds are reported in Table 2.2.

	MSC	**Fibroblast**	**Chondrocyte**	**Osteoblast**
Migration speed *μm day^{-1}*	720	720	0	0

Table 2.2. – Cellular migration speed.

The movement associated with cellular migration was based on iterative changes ("jumps") on the local position of the cell within the agent-based model: each cell changed its position in the cellular distribution agent-based model by "jumping" in its adjacent surroundings. The migration was characterized by 6 degrees of freedom: 2 possible ways (forward and backward) for each of the 3 directions (x, y, z) in the space. In this way, the cell migrated to one of its 6 surrounding positions at every jump. The jump was considered done only if the new position was available. An available position was identified in the agent-based model by the phenotype value 0, which meant that the position was not already occupied by another cell and it was within the callus domain. As a size of 10 μm was associated with each position in the agent-based model, it was considered that for each jump the cell migrated 10 μm. This meant that MSCs and fibroblasts, which migrated 720 μm day^{-1}, made 72 jumps in total in one mouse model iteration (24 hours). In the rat model, each iteration (2 hours) was characterized by 6 jumps of each migrating cell. All MSCs and fibroblasts tried to migrate at every iteration by its specific number of jumps. The algorithm randomly chose a cell in the agent-based model between all the migrating cells. Then all the six surrounding positions around the selected cell were checked to find the available positions.

If there were no available positions, the cell did not further migrate for that iteration. If the cell had available positions in its surroundings, the algorithm chose randomly one of them and assigned the cell phenotype value and the age of the cell as parameters of the new position. The previous position became available by assigning phenotype value 0 and age 0. When all the jumps were done, the cell was marked as already migrated, to avoid the cell to be randomly chosen again to migrate during the same iteration. When all the cells have performed all jumps in one iteration, the mark as migrated cell was removed. The cellular migration procedure was considered terminated after this last step. A schematic representation of one cellular migration jump is shown in Figure 2.13.

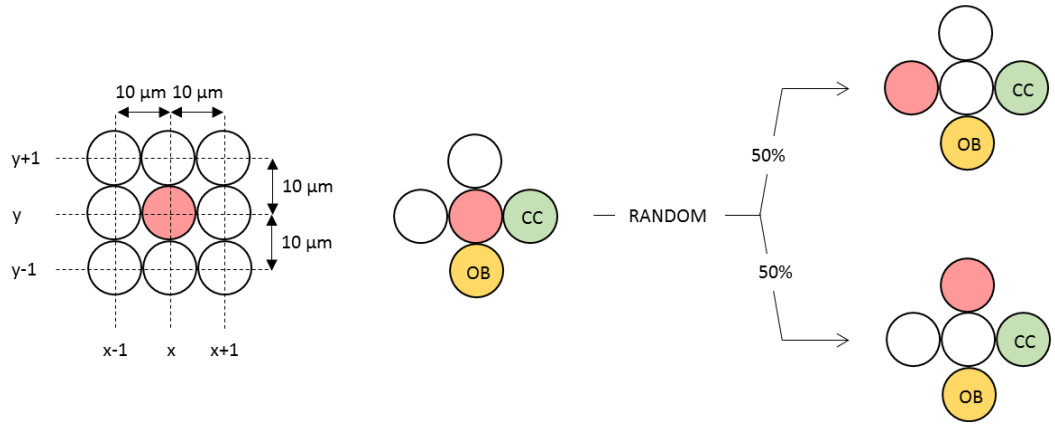

Figure 2.13. – Schematic representation of one migration jump of a cell (pink).

Cell proliferation

The proliferation algorithm was based on the duplication of a cell with the creation of a daughter cell that shared the same phenotype. All the cells were able to proliferate but, to respect proliferation ratios found in Checa et al. (2011) [61], the algorithm duplicated only a defined number of cells for each phenotype at every iteration, according to proliferation ratios reported in Table 2.3. For example, every daily iteration, 20% of the entire chondrocyte population proliferated due to chondrocyte proliferation (Table 2.3.).

	MSC	Fibroblast	Chondrocyte	Osteoblast
Proliferation ratio *day^{-1}*	0.60	0.55	0.20	0.30

Table 2.3. – Cellular proliferation ratio.

The proliferation algorithm created a copy of the proliferating cell with the same phenotype. The newly formed cell was positioned in the immediate surroundings, according to availability. The algorithm steps were analogous to the ones of cellular migration but the original cell position was not vacated. At the end of the proliferation process, a new cell was seeded in the agent-based model, increasing the population of the specific phenotype by +1. This meant that for the MSC population, characterized by a proliferation ratio of 0.60 day^{-1}, there was an increment up to 60% for every daily iteration (1 complete iteration for mouse model, 12 complete iterations for rat model). In this model, the proliferation algorithm began right after the migration of all the cells was completed. All the cells of the same phenotype were counted and, according to their specific proliferation ratio, a certain amount of them proliferated. The cells were randomly chosen within the agent-based model and declared as ready to proliferate in the current iteration. For each ready to proliferate cell, an examination of the surroundings was performed to investigate the available positions. The algorithm chose randomly one of the available positions where to spawn one daughter cell with the same phenotype and age 1. If no positions were available, the cell did not proliferate during the current iteration: the mother cell stayed in its original position and neither its phenotype nor age was affected. Mother and daughter cells were subject to a blocking condition to prevent their involvement in proliferation within the same iteration. When all the cells proliferated, the blocking condition was removed. A schematic example of proliferation is shown in Figure 2.14.

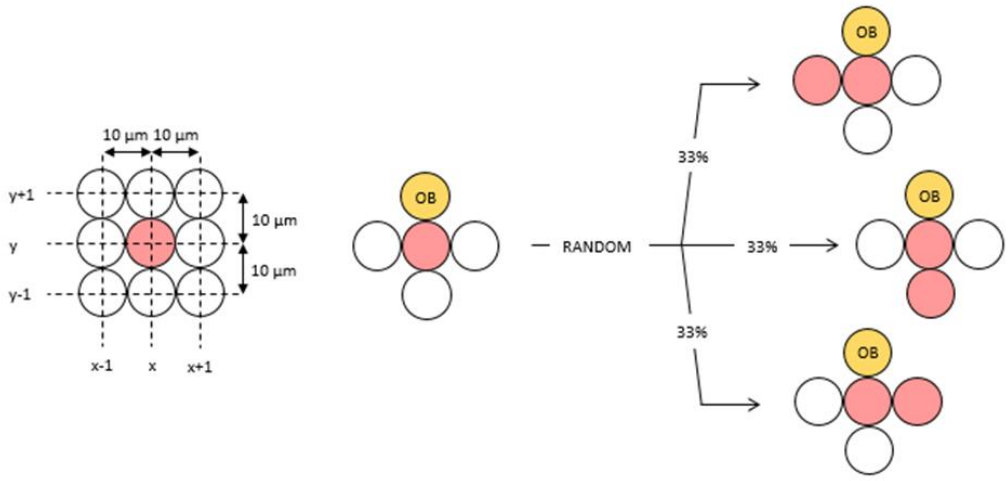

Figure 2.14. – Schematic representation of one cell (pink) proliferation.

Cell differentiation

Cellular differentiation is the change in cell phenotype. In the models, the interfragmentary mechanical environment stimulates mature MSCs to differentiate into fibroblasts, chondrocytes or osteoblasts. In these models, cellular differentiation involved only MSCs characterized by more than 6 days of age, which was imposed as maturation age for MSCs [93]. The algorithm was divided into two phases. The first phase happened at the beginning of every iteration, when the mechanics within the FE model callus domain was investigated. During the second phase, a new phenotype was assigned to mature MSCs as a function of the mechanical environment. Differentiation followed in this model the Prendergast et al. (1997) differentiation theory, which describes cell differentiation as a function of octahedral shear strain and fluid flow velocity [57]. The output of the previously described FE model quantified the mechanical environment within the callus region. A linear relationship between octahedral shear strain and fluid flow velocity was used to evaluate the stimuli that regulated cellular differentiation:

$$S = \frac{\gamma}{a} + \frac{v}{b} \tag{1}$$

In Eq. 1, S represents the global mechanical stimulus that regulated cell differentiation. The magnitude of the octahedral shear strain and fluid flow velcoity were identified by γ and v, respectively. Moreover, a = 0.0375 and b = 3 μm s^{-1} according to Huiskes et al. (1997) [94]. The FE model did not output the value of the octahedral shear strain but it predicted axial strain in the three Cartesian directions (e_{11}, e_{22}, e_{33}) and the shear strain between each pair (e_{12}, e_{23}, e_{13}). Octahedral shear strain (γ) was obtained from those values according to the following formula:

$$\gamma = \frac{2}{3}\sqrt{(e_{11}-e_{22})^2+(e_{22}-e_{33})^2+(e_{11}-e_{33})^2+6e_{12}+6e_{23}+6e_{13}} \quad (2)$$

Fluid flow velocity (v) was predicted directly from the FE model. In this project, the general mechano-regulatory theory, which was shown to correctly reproduce bone healing in small mammals [61], was used to investigate the mechanical regulation of bone healing in mice and rats. The differentiation boundaries for the S values were taken from Checa et al. (2011) [61]:

Mature Osteoblast	Immature Osteoblast	Chondrocyte	Fibroblast
$S \leq 2.53$	$2.53 < S \leq 3.00$	$3.00 < S \leq 5.00$	$S > 5.00$

Table 2.4. – Mechanical stimuli (S) differentiation boundaries in rat osteotomy model.

Moreover, in this model also bone resorption was taken into consideration. This process plays a main role in the bone healing remodeling phase. In this model, resorption of tissue was characterized by mechanical stimuli $S \leq 0.50$. A silent zone of differentiation, characterized by a range of mechanical stimuli that did not promote cellular differentiation, was set in the range $0.50 < S \leq 0.80$. These ranges were obtained from Lacroix and Prendergast (2002) [95] and adapted to higher mechanical stimuli. A graphic representation of the global mechano-regulatory theory is represented in Figure 2.15.

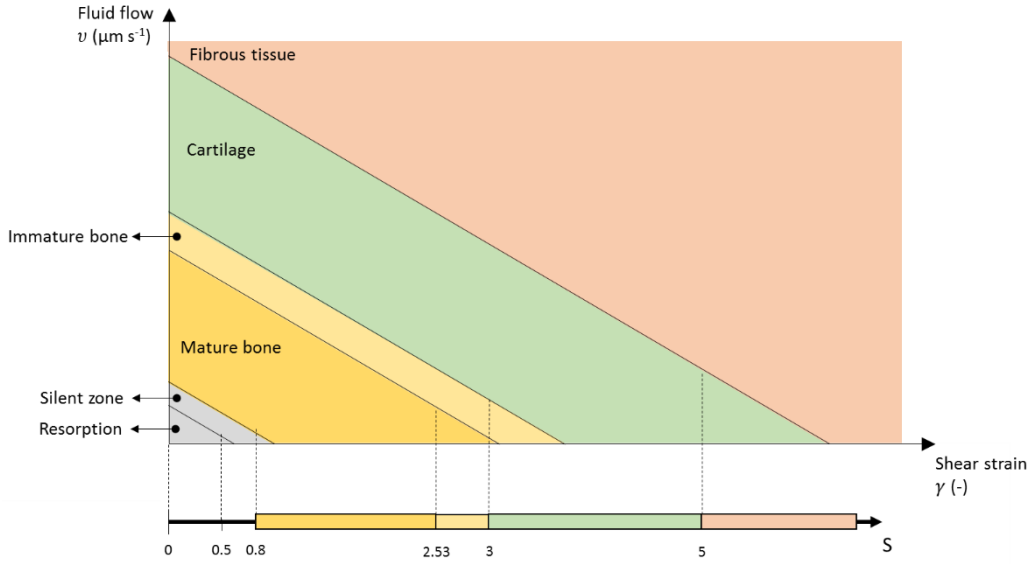

Figure 2.15. – Graphic representation of how octahedral shear strain and fluid flow velocity drove MSC mechano-regulated differentiation [95].

Within this project, it was shown that bone healing in mice happens under higher mechanical stimuli compared to rats (*§ 3.1.2*.). Therefore, since the differentiation theory was derived from the rat *in vivo* experiments, it was necessary to modify the mechano-regulatory theory to describe bone healing in the mouse model. To do this, the boundaries of the mechanical stimulus S were shifted to higher values. Many different values for the S boundaries were tested with the aim to match *in silico* predictions of tissue patterning during bone healing and *in vivo* observations (*Appendix B*). The investigation showed that higher mechanical stimuli could explain tissue differentiation during the bone healing progression in mice (Table 2.5.):

Resorption	**Silent zone**	**Mature Osteoblast**	**Immature Osteoblast**	**Chondrocyte**	**Fibroblast**
$S \leq 0.80$	$0.80 < S \leq 1.00$	$1.00 < S \leq 6.00$	$6.00 < S \leq 13.00$	$13.00 < S \leq 35.00$	$S > 35$

Table 2.5. – Proposed mechanical stimuli (S) differentiation boundaries in mouse osteotomy model.

As previously mentioned, the cellular differentiation algorithm was divided into two phases. In the first phase, the distribution of the mechanical stimuli obtained from the FE model was discretized in the space domain of the cellular distribution agent-based model. As result, the value of stimulus S was assigned as an additional parameter to each cell position in the agent-based model, for a total of 6 parameters. In the second phase, the cell differentiation algorithm counted the mature MSCs within the agent-based model. As the differentiation process involves 30% of the mature MSCs every day [61], the total number of mature MSCs was multiplied by 0.30 (or 0.30/12 in case of 2h iteration in rat model) to quantify the number of cells ready to differentiate. Then, this amount of mature MSCs were randomly chosen to differentiate. The differentiation of the MSCs was performed by changing their phenotype value from 1–MSC to one of the values associated with the other phenotypes (2-mature osteoblast, 3–immature osteoblast, 4–chondrocyte, 5-fibroblast), taking into account the mechanical environment assigned to the position of the agent-based model during the first phase. The phenotype value was the only parameter affected by the differentiation in the agent-based model: the cell position and its age did not change. A schematic representation of the differentiation of MSCs is presented in Figure 2.16.

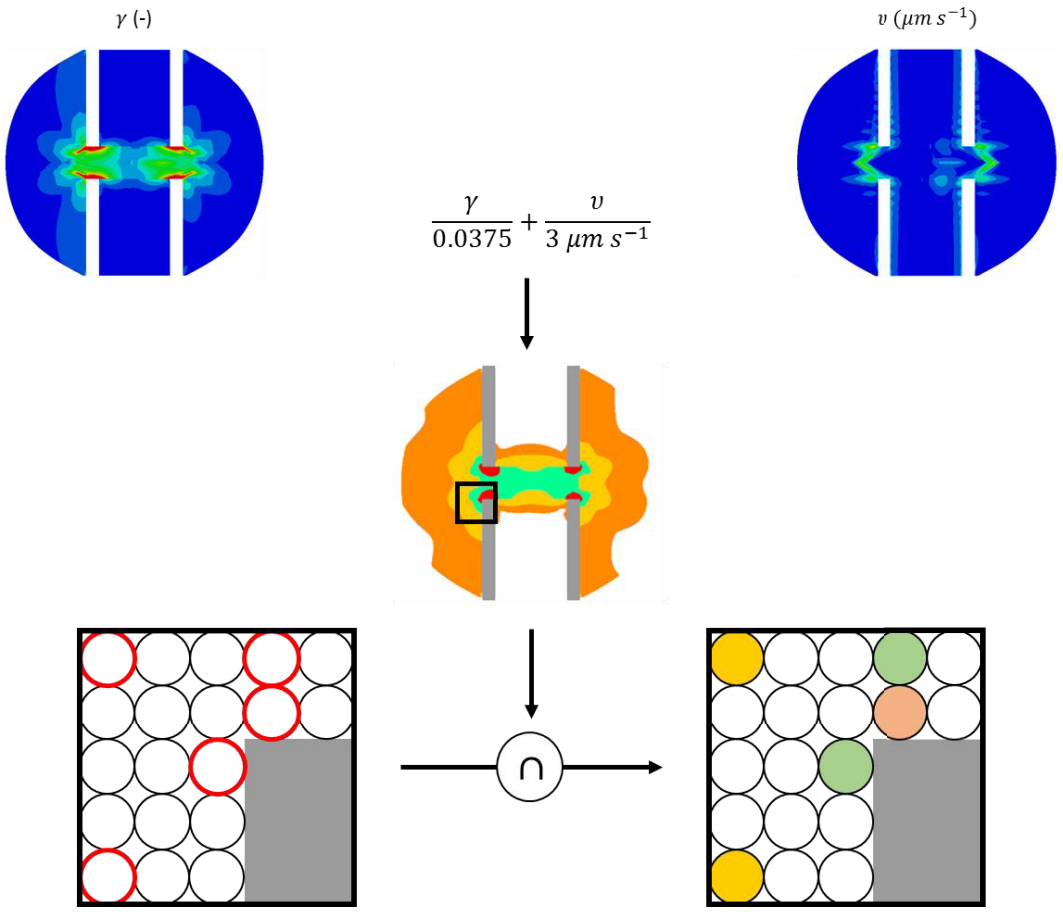

Figure 2.16. – Schematic representation of how mechano-regulation of bone healing was simulated. Combination of octaheadral shear strain and fluid flow velocity designed the differentiation zones within the callus domain. Randomly chosen mature MSCs (red circled) differentiated into new phenotypes, according to the mechanical stimulus S. γ: octahedral shear strain, v: fluid flow velocity.

Cell apoptosis

Cellular apoptosis is the programmed death of cells and it was simulated, in the agent-based model, at the end of every iteration. It was characterized by the removal of cells to create available positions for migration and proliferation in future iterations. The cells were subject to apoptosis according to the following ratios [61]:

	MSC	**Fibroblast**	**Chondrocyte**	**Osteoblast**
Apoptosis ratio *day-1*	0.05	0.05	0.10	0.16

Table 2.6. – Cellular apoptosis ratio.

The apoptosis algorithm counted, as initial step, the number of cells of each phenotype. A part of these cells, represented by the correspondent apoptosis ratio, was randomly selected within the callus domain and processed to apoptosis. The age of the cells did not influence the process of selection, which was random. To avoid the apoptosis of recently differentiated cells, mechanical stimulation played a role in the selection of the cells to remove. Following the distribution of mechanical stimuli within the agent-based model, if the cell was characterized by a S parameter that allowed the apoptosis of the corresponding cell phenotype (Figure 2.17.), then the selected cell was assigned the phenotype value 0 and age 0. Otherwise, if the stimuli did not allow apoptosis, the cell kept its phenotype and age and another position was randomly selected.

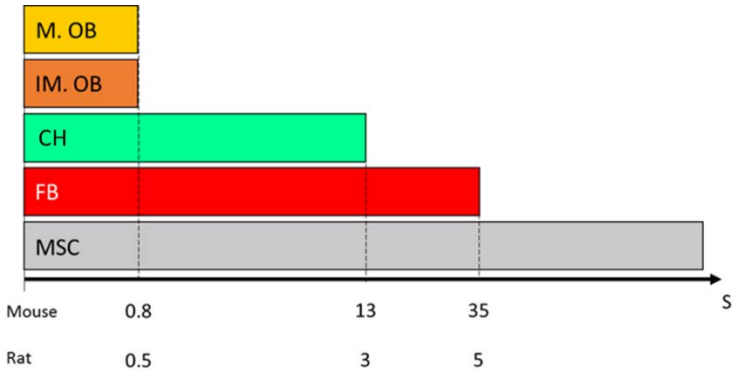

Figure 2.17. – Mechanical stimuli (S) ranges within the different cell phenotypes are subject to apoptosis. M. OB: mature osteoblast, IM. OB: immature osteoblast, CH: chondrocyte, FB: fibroblast. MSCs are always subject to apoptosis, regardless of the mechanical stimuli. Note: the mechanical stimuli axis reports both values for the mouse (top) and the rat (bottom) models.

When all the cells subject to apoptosis were removed, the process was considered concluded. Cellular apoptosis was the last phase that influenced the cell distribution in the agent-based model at each iteration.

Tissue matrix production and degradation

Bone, cartilage and fibrous tissue production and degradation were included in the model dynamics. Their presence within the callus was included in the same agent-based model used to simulate cellular distribution. To represent the tissue level in the agent-based model, additional phenotype values were chosen: 12-bone tissue, 14-cartilage, 15-fibrous tissue. Like cells, also tissues occupy positions within the cellular distribution agent-based model. When tissue formed at a certain position, the corresponding tissue value was assigned to that position; when it degraded, the parameter value of the position was set back to empty (0). Tissue could form only on available positions and only pre-existent tissue degraded. The different tissue matrices volumes were produced and degraded according to literature data rates [96]:

	Fibrous tissue	**Cartilage**	**Bone tissue**
Production ratio $\mu m^3\ cell^{-1}\ day^{-1}$	5000	5000	3000
Degradation ratio $\mu m^3\ cell^{-1}\ day^{-1}$	5000	5000	5000

Table 2.7. – Cellular tissue matrix production and degradation.

Tissue formation was simulated in the immediate surroundings of the cell that produce that kind of tissue. 12-bone tissue was produced by 2-mature osteoblast, 14-cartilage was produced by 4-chondrocyte and 15-fibrous tissue was produced by 5-fibroblast. 1-MSC and 3-immature osteoblast did not produce tissues in this model. The mechanical environment was additionally included in the tissue matrix production algorithm. In fact, only cells belonging to elements under their phenotype-specific mechanical stimuli range were considered able to produce tissue matrix [57] [96] *(§ 2.2.2., Cell differentiation*). At every iteration, each cell generated an amount of matrix in the surrounding positions according to the specific production ratio. In the cellular distribution agent-based model, tissue formation was discretized in one agent assigned to the new tissue phenotype every 1000 μm^3 of newly

formed tissue. When tissue was determined to form in a specific position, an additional test was performed by counting the number of positions (n_{tiss}) in the agent-based model occupied by the tissue inside a 5 x 5 x 5 cube with the center in the position where the tissue was going to form. The probability of the tissue to form in that position (P_{tiss}) linearly decreased with the increase of the spaces occupied by the same tissue:

$$P_{tiss} = 100\% * \left(1 - \frac{n_{tiss}}{125}\right) \quad (3)$$

If the tissue matrix was produced, the specific tissue phenotype value was assigned to that position. That position was not available for other cells to migrate/proliferate and for tissue to form in the following iterations, until it became empty again due to tissue matrix degradation.

Tissue degradation was simulated by removing tissues from the spaces of the agent-based model. The degradation ratio quantified the amount of tissue removed at each iteration. The mechanical environment played a role in this algorithm as the cells involved in the process were only the ones that belonged to finite elements under mechanical stimuli different from the specific cell differentiation range [57] [96] (*§ 2.2.2., Cell differentiation*). The number of cells that respected the condition was calculated for each phenotype and multiplied by the degradation ratio of the tissue. The resulted volume was divided by 1000 μm^3 to translate it into the number of agents of the model where tissue degradation happened. That amount of agents was randomly chosen from the ones occupied by that specific tissue, under specific mechanical conditions. Empty value (0) was assigned to the phenotype value of the agent-based model space where degradation happened.

2.2.3. Interaction with finite element model

The multiscale platform used to simulate bone healing at different length- and time-scales took its strength from the capacity to couple models that investigated both mechanical and biological features (*Appendix C*). While the FE model investigated mechanics, the behavior of the cells within the bone healing was simulated with the agent-based model. As previously described, there was a double-way relationship between the two models: tissue distribution determined the mechanical properties within the callus domain while the mechanics affected the differentiation of the cells and the extracellular matrix production and degradation. The interaction between the two models was based on the spatial location of the elements of the bone healing FE model and the distribution of cells within the agent-based model. Each agent-based model cell was included inside the volume of an element of the FE model. The cell was considered to belong to that specific element. As every element had an average side length of 0.10 mm and each agent cell was characterized by a diameter of 0.01 mm, in each element it was on average possible to fit 1000 cells from the agent-based model. To evaluate whether a specific cell belonged to an element, the equations of the six surfaces that characterized the hexahedron element were determined:

$$Ax + By + Cz + D = 0 \tag{4}$$

Where A, B, C and D depends on the coordinates of the nodes that characterize the vertices of the surface. The agent at position ($x0$, $y0$, $z0$) belonged to the element if the condition

$$A\ x0 + B\ y0 + C\ z0 + D \geq 0 \tag{5}$$

was respected for all the six surfaces of the element. Each cell was associated with only one element and each element was associated with multiple cells. All the cells that belonged to an element were characterized by the mechanical stimuli associated with it. Differentiation of the cells in those positions was driven to the specific phenotype (*§ 2.2.2., Cell differentiation*). Vice versa,

material properties of the element were determined based on the phenotype of the tissues that belonged to it, as described in the following section.

Update of FE material properties

The FE models developed in this study to investigate the mechano-regulation of bone healing dynamically change their mechanical properties within the healing region. In order to represent the progressive stiffening of the callus due to tissue formation, the material properties within the callus domain changed through the entire process as a function of the tissue patterning evolution. The material properties that characterized the callus were initialized as granulation tissue. As a function of the dynamical variation of tissue distribution inside the callus domain, each element iteratively updated its material properties. The material properties of each tissue simulated in this work are reported in Table 2.8.

		Fibrous tissue	**Cartilage**	**Immature bone**	**Mature bone**
Solid phase	**Young's modulus** *MPa*	2	10	1000	5000
	Poisson's ratio -	0.167	0.3	0.3	0.3
	Bulk modulus grain *MPa*	2300	3700	13940	13940
Fluid phase	**Permeability** $10^{-14}\ m^4\ N^{-1}\ s^{-1}$	1	0.5	10	37
	Bulk modulus fluid *MPa*	2300	2300	2300	2300

Table 2.8. – Material properties of the tissues simulated within the callus domain.

The elements weighted their mechanical properties values based on the number of agent-based model positions occupied by the tissues that belonged to the element.

In Eq. 6, the equation that calculated the Young's modulus in every element (E_{elem}) is reported.

$$E_{elem} = \frac{\sum_i \ n(i) * E(i)}{\sum_i \ n(i)} \tag{6}$$

The value i identified the four tissues used in this study: granulation tissue (i = 11), bone (i = 12), cartilage (i = 14), fibrous tissue (i = 15). $E(i)$ represented the Young's modulus of the specific material. According to this definition, it can be observed in Table 2.8. that, for example, $E(14)$ = 10 MPa is Young's modulus of cartilage. The value $n(i)$ is the number of agents of the specific tissue phenotype i inside the considered element. Under condition i =11 (granulation tissue), $n(i)$ was the number of spaces of the agent-based model occupied by MSCs or empty. To take into account the tissue consolidation through time, each element's Young's modulus was averaged with the values predicted by the model in the previous ten iterations. If less than ten iterations were performed, all the iterations until day 0 were taken into consideration.

$$E_{elem}(t) = \begin{cases} \frac{\sum_{k=t-10}^{t-1} E(k) + E_{elem}}{10} & if\ t > 10 \\ \frac{\sum_{k=0}^{t-1} E(k) + E_{elem}}{t-1} & if\ t \leq 10 \end{cases} \tag{7}$$

Analogous algorithms updated also the other material properties (Poisson's ratio, permeability, bulk modulus). The model mechanical behavior was updated by creating new materials for each element inside the callus domain. Each element was entirely characterized by the mechanical properties of the newly assigned material.

2.3. BMP-2 agent-based model

In the rat model, the effect of BMP-2 concentration on cellular behavior was investigated. For this reason, a second agent-based model was developed to simulate the dynamics of the protein within the callus domain. As the cellular distribution agent-based model, also protein dynamics was simulated within a 3D matrix. Each element of the matrix was associated with a triplet of Cartesian coordinates (x, y, z) and a parameter that represented the concentration of BMP-2 (ng mL^{-1}) in that position. The main difference with the cellular distribution agent-based model concerned the size of each element. In the BMP-2 concentration agent-based model, each agent was considered to represent 50 μm-size cubic volume. The global dimension of the matrix was kept similar to the cell distribution agent-based model: 6 mm (x), 6 mm (y), 8.8 mm (z). Consequently, the number of agents in the three dimensions of the BMP-2 matrix was 120 (x), 120 (y) and 176 (z). The BMP-2 agent-based model was characterized by 2,534,400 agents.

2.3.1. BMP-2 dynamics

The agent-based model of BMP-2 simulated the dynamics of the growth factor concentration within the callus. The parameter associated with each agent of the model quantified BMP-2 concentration in ng mL^{-1}. Iteratively, the values varied according to BMP-2 diffusion and degradation. Moreover, with the aim of investigating the multiscale relationship with the cellular level, the cellular distribution matrix was coupled with the BMP-2 matrix to include the capacity of cells to produce and consume BMP-2. To initialize the matrix, all the positions were assigned the physiological value of 0.008 ng mL^{-1} [74]. To reduce the investigation to the FE callus domain, the buffer value -1 was assigned to all the positions that were excluded from the region of interest.

For the simulation of the case studies where rat bone healing was enhanced with BMP-2, a "release region" was located within the agent-based model. This region was identified within the osteotomy gap as a cylinder that separated

the bone defect extremities and its dimensions were adapted to the size of the bone cortex cross section (Figure 2.18.).

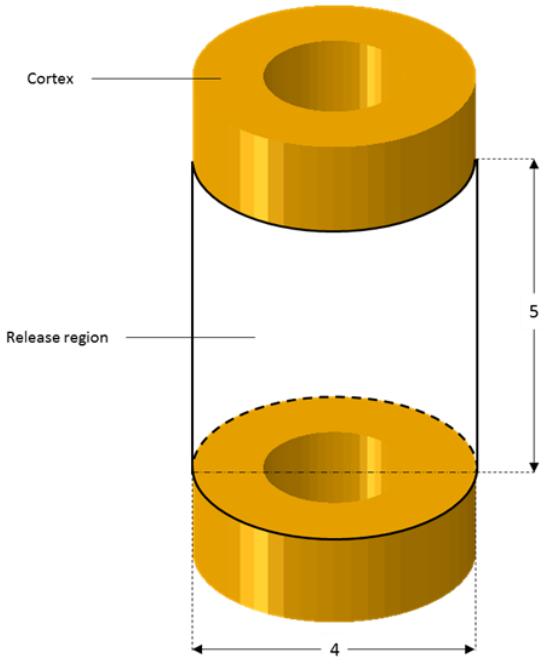

Figure 2.18. – Position of the BMP-2 release region within the defect gap. Dimensions in mm.

Two different release models were applied to the dynamics of BMP-2: instantaneous and gradual release. When BMP-2 was released instantaneously, the entire quantity of BMP-2 within the release region was immediately available to regulate the cellular behavior. Under gradual release conditions, which will be extensively explained in *§ 2.3.2.*, the agent-based model was characterized by an initially encapsulated quantity of BMP-2 within the release region. The encapsulated BMP-2 was gradually released and made available to regulate cellular behavior. This process aimed to simulate the encapsulation of BMP-2 within a collagen sponge, like the one used in the *in vivo* experiment [45]. BMP-2 specific release ratio and collagen degradation factor were implemented in the model to simulate the presence of the sponge *(§ 2.3.2.*).

Cellular distribution and BMP-2 concentration agent-based models interacted between them. Cellular presence played a role in the production and consumption of BMP-2 and, vice versa, the concentration of BMP-2 influenced the cellular behavior by influencing the migration and proliferation capacity (*Appendix C*). The concentration value that characterized each agent of the BMP-2 concentration model affected the behavior of all the cells that shared the same position or its surroundings. In this model, the BMP-2 concentration value associated with a specific region within the BMP-2 agent-based model regulated the activities of all the cells of the cellular distribution agent-based model inside that region. In fact, as 10 μm diameter was assigned as the size of each cell in the specific agent-based model, the same BMP-2 concentration region (50 μm size) was shared by 5 cells for each direction, for a total of 125 cells contained in each BMP-2 concentration region (Figure 2.19.).

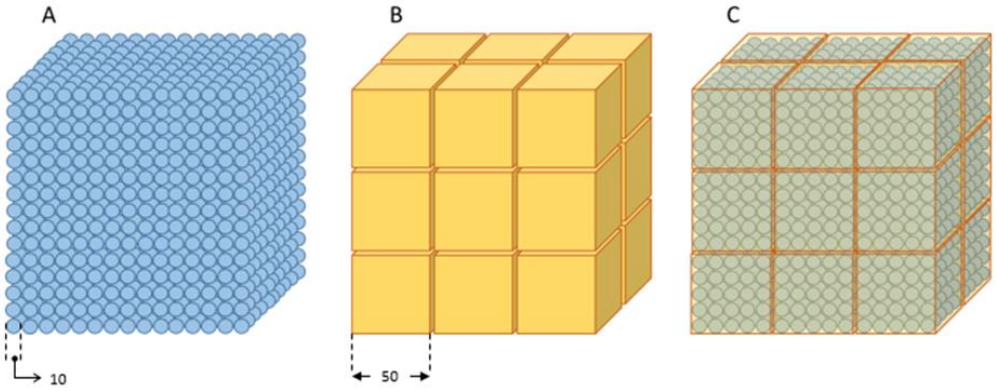

Figure 2.19. – Schematic representation and dimensions (in mm) of agents of the cellular distribution agent-based model (A) and regions of BMP-2 concentration agent-based model (B). They are positioned so that each region of the BMP-2 model contained 125 agents of the cellular model, as shown in C.

BMP-2 cellular production

BMP-2 production within the healing region was regulated by the presence of cells. MSCs and osteoblasts were simulated as the main producers of BMP-2 [74]. A rule was defined to increase the quantity of BMP-2 within a certain region of the agent-based model according to the local concentration of MSCs (c_s) and osteoblasts (c_b). Those two values were obtained from the quantity of MSCs and osteoblasts in the cell distribution agent-based model that were contained in each region of the BMP-2 matrix. In this model, all the processes were discretized in space (prerogative of the agent-based model domain, which is discrete) and in time (every update is evaluated after a discrete period of time). The equation of BMP-2 production term [74] was adapted to describe the increase of BMP-2 concentration ($[BMP2]$ in ng mL^{-1}) in the discrete period of time of 1 iteration: Δt = 2 h = 1/12 day.

$$d[BMP2]\,(x,y,z,t)_{prod} = \alpha_{prod} * \frac{c_s(x,y,z,t) + c_b(x,y,z,t)}{\gamma * [BMP2]\,(x,y,z,t) + \gamma_0} * \Delta t \qquad (8)$$

Eq. 8 describes the variation of BMP-2 concentration at position (x, y, z) and iteration t due to cellular production of BMP-2. Two variables (the quantity of MSCs and osteoblasts in the surroundings) and the previous state of the BMP-2 concentration influence the total production. The rest of the parameters were fixed and adopted from Ribeiro et al. (2015) [74]:

$\alpha_{prod} = 2 * 10^{-9}\ ng\ mL^{-1}\ cell^{-1}\ day^{-1}$

$\gamma = 15\ mL\ ng^{-1}$

$\gamma_0 = 0.01$

BMP-2 cellular consumption

Cellular properties, such as migration speed and proliferative capacity, were regulated by the presence of BMP-2 (*§ 2.3.3.*). The use of the growth factor results in its consumption. This depletion was indeed included in the

agent-based model as a reduction of BMP-2 concentration in the zones where MSCs and osteoblasts were present [74]. As in the BMP-2 production algorithm, the consumption entity depended on the number of cells belonging to the region of the BMP-2 agent-based model. The same variables previously described for the BMP-2 production algorithm were used to quantify the number of cells within the element: c_s (MSCs) and c_b (osteoblast). As the name suggests, cellular consumption was represented in the agent-based model as a reduction of BMP-2 concentration. The equation that quantifies this decrease was adapted from Ribeiro et al. (2015) [74] to describe the variation of BMP-2 concentration ($[BMP2]$ in ng mL^{-1}) in a discrete period of time of 1 iteration: Δt = 2 h = 1/12 day.

$$d[BMP2]\,(x,y,z,t)_{cons} = -\frac{V * \left(c_s(x,y,z,t) + c_b(x,y,z,t)\right)}{K_m^a + [BMP2]\,(x,y,z,t)} * [BMP2]\,(x,y,z,t) * \Delta t \qquad (9)$$

Eq. 9 describes the reduction of BMP-2 concentration at position (x, y, z) and iteration t due to BMP-2 cellular consumption. Two variables, the quantity of MSCs and osteoblasts in the surroundings and the previous state of the BMP-2 concentration, influenced the amount of BMP-2 consumed, together with the fixed parameters obtained from the literature [74]:

$V = 1.43 * 10^{-7}\ ng\ mL^{-1}\ cell^{-1}\ day^{-1}$

$K_m^a = 11.01\ ng\ mL^{-1}$

BMP-2 diffusion

BMP-2 dynamics was not only dependent on the distribution of cells within the callus domain. The BMP-2 agent-based model was also regulated by the movement of the substance due to diffusion. In this model, Fick's law of diffusion [97] was adapted to simulate the diffusion of the molecules as a function of their concentration within the callus domain. The diffusion homogenized the distribution of BMP-2 in the space by moving BMP-2 from high-concentration to low-concentration regions. BMP-2 diffusion coefficient

(D = 8.64 mm^2 day^{-1} [74]) described the speed of the process. The diffusion law was adapted to a discrete domain by varying the concentration of each element in the agent-based model according to the concentration of BMP-2 in the surrounding elements. In the algorithm, 24 surrounding agents were checked to describe the diffusion equation. The position of those agents is reported in Figure 2.20.

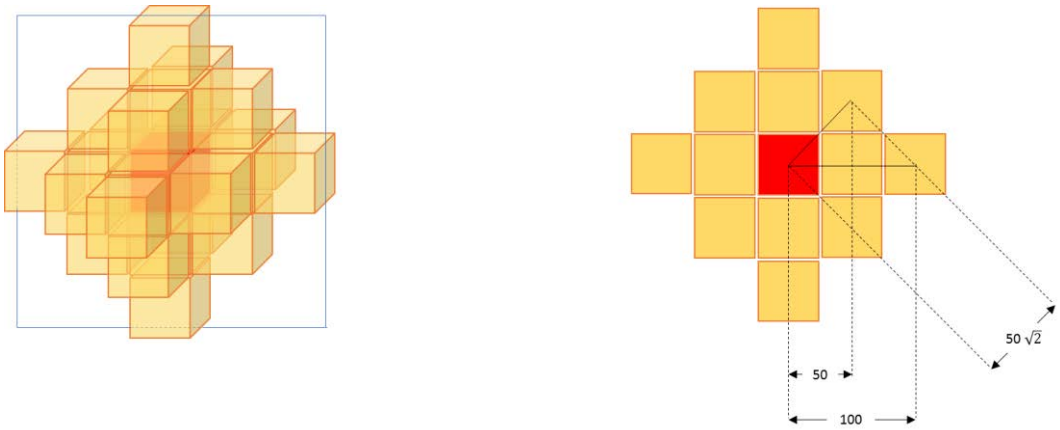

Figure 2.20. – Three-dimensional representation (left) and cross section (right) of all the elements involved in the diffusion of BMP-2 within the red element. The effect of BMP-2 concentration of the yellow spaces on the diffusion gradient was weighted on the distance between the centers of the elements (reported in mm).

The contribution to each BMP-2 agent-based region from its surroundings was included in the diffusion equation to describe the variation in concentration. The contribution of each agent was inversely weighted according to its distance to the element under investigation, which Cartesian coordinates were (x, y, z). The processed used in this model to describe the variation of BMP-2 concentration due to diffusion can be summarized in this equation:

$$d[BMP2]\,(x,y,z,t)_{diff} = D * \frac{dx + dy + dz + dd}{6 * e^{-1} + 6 * e^{-2} + 12 * e^{-\sqrt{2}}} * \Delta t \qquad (10)$$

Where:

$$dx = \sum_{i=-1}^{1} \sum_{j=-1\,(j\neq 0)}^{1} \left([BMP2]\,(x+i, y+j, z, t) - [BMP2]\,(x, y, z, t)\right) * e^{-\sqrt{i^2+j^2}}$$

$$dy = \sum_{j=-1}^{1} \sum_{k=-1\,(k\neq 0)}^{1} \left([BMP2]\,(x, y+j, z+k, t) - [BMP2]\,(x, y, z, t)\right) * e^{-\sqrt{j^2+k^2}}$$

$$dz = \sum_{k=-1}^{1} \sum_{i=-1\,(i\neq 0)}^{1} \left([BMP2]\,(x+i, y, z+k, t) - [BMP2]\,(x, y, z, t)\right) * e^{-\sqrt{i^2+k^2}}$$

$$\begin{aligned} dd = \Big(\big([BMP2]\,(x+2, y, z, t) + [BMP2]\,(x-2, y, z, t) + [BMP2]\,(x, y+2, z, t) \\ + [BMP2]\,(x, y-2, z, t) + [BMP2]\,(x, y, z+2, t) + [BMP2]\,(x, y, z-2, t)\big) \\ - 6 * [BMP2]\,(x, y, z, t)\Big) * e^{-2} \end{aligned}$$

The algorithm pushed BMP-2 from high concentration zones to low concentration, without changing the global amount of it. For this reason, the value of $d[BMP2]\,(x, y, z, t)_{diff}$ could be either positive or negative. Dirichlet boundary conditions were imposed on the algorithm when the positions closer to the borders were investigated: the same BMP-2 concentration as the border was given to the regions outside the callus to avoid diffusion.

BMP-2 degradation

Degradation of BMP-2 was also modelled. BMP-2 exponentially decayed with a half-life $t_{\frac{1}{2}}$ = 0.42 days [74] and this behavior is synthesized in the following equation:

$$d[BMP2]\,(x, y, z, t)_{deg} = [BMP2]\,(x, y, z, t) * \left(1 - 2^{-\frac{\Delta t}{t_{\frac{1}{2}}}}\right) \qquad (11)$$

The degradation of BMP-2 in each agent only depended on its previous concentration. The BMP-2 degradation dynamics is shown in Figure 2.21.

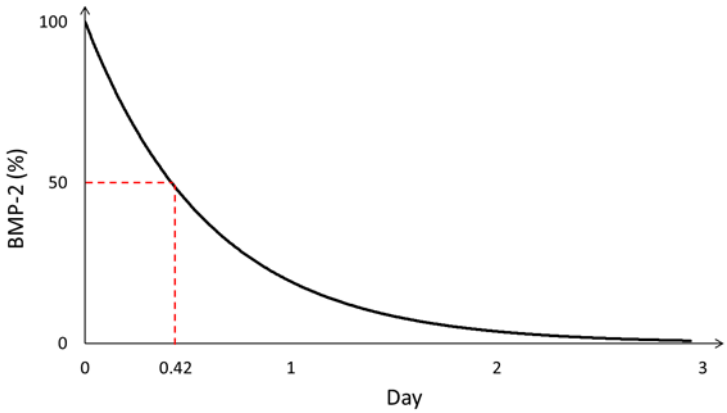

Figure 2.21. – Degradation effect on BMP-2 concentration.

The BMP-2 concentration in each agent was updated at every iteration according to the following equation:

$$[BMP2]\,(x,y,z,t+\Delta t) = [BMP2]\,(x,y,z,t) + d[BMP2]\,(x,y,z,t)_{prod} - d[BMP2]\,(x,y,z,t)_{cons} + d[BMP2]\,(x,y,z,t)_{diff} - d[BMP2]\,(x,y,z,t)_{deg} \quad (12)$$

The new state $[BMP2]\,(x,y,z,t+\Delta t)$ was then used as the initial state for the following iteration.

2.3.2. Collagen sponge

Collagen sponges are typically used *in vivo* to carry growth factors and other substances within the bone osteotomy to guarantee a gradual release. To reproduce the presence of a collagen sponge within the osteotomy gap, a different algorithm was created to simulate BMP-2 dynamics. The sponge was not added as an additional element of the model, but a "release zone" was designed to include all the positions of the agent model within the volume occupied by the sponge. Differently from the immediate release case study, where the whole BMP-2 treatment was simulated to be free within the release zone since the first iteration, the free BMP-2 agent-based model was initialized to 0 ng mL^{-1} within the collagen sponge. The BMP-2 substance was simulated to be entirely encapsulated within the collagen sponge and, at every iteration,

a certain amount of BMP-2 was released from the sponge [98]. The released BMP-2 was homogeneously distributed within the release region and the agent model increased the concentration of each agent within the release zone, according to the released BMP-2 quantity. The same mass of BMP-2 was, of course, removed from the collagen sponge reservoir amount. Only the released BMP-2 was subject to the BMP-2 dynamics described before. Moreover, the cells and tissues were only subject to the effect of the released BMP-2.

In the model, BMP-2 was subject to exponential decay also when encapsulated. However, its degradation was simulated to happen slowly, as the half-life time of encapsulated BMP-2 ($t_{\frac{1}{2}}$ = 3.25 days) [74] is longer than the free BMP-2 ($t_{\frac{1}{2}}$ = 0.42 day) [74]. Over the degradation, encapsulated BMP-2 was not subject to cellular production, consumption and diffusion. Those processes affected only released BMP-2 as previously described.

BMP-2 release

The process of BMP-2 release was simulated as a gradual reduction of BMP-2 concentration within the encapsulated BMP-2 agent model and the equal increase of free BMP-2 concentration at the analogous position in the BMP-2 agent model. The release was gradual and it followed the following two equations:

$$[BMP2]_{caps}\,(x,y,z,t) = [BMP2]_{caps}\,(x,y,z)_0 * \lambda_{rel}(t) \tag{13}$$

$$[BMP2]\,(x,y,z,t+\Delta t) = [BMP2]\,(x,y,z,t) + [BMP2]_{caps}(x,y,z,t) - [BMP2]_{caps}(x,y,z,t+\Delta t) \tag{14}$$

Where $[BMP2]_{caps}\,(x,y,z,t)$ identified the concentration of scaffold encapsulated BMP-2 at position (x,y,z) at time step t. $[BMP2]_{caps}\,(x,y,z)_0$ is the initial concentration of BMP-2 capsulated within the collagen sponge. Only the agents of the BMP-2 model within the release region were subject to concentration rise due to capsulated BMP-2 release. The gradual release of

BMP-2 was regulated by the collagen scaffold release rate $\lambda_{rel}(t)$, which dynamically varied through the entire healing process:

$$\lambda_{rel}(t) = 0.68\, e^{-0.012*t} + 0.221 e^{-0.00006*t} \quad (15)$$

This time-dependent function was derived from experimental data on collagen sponge BMP-2 adsorption [98] (Figure 2.22.).

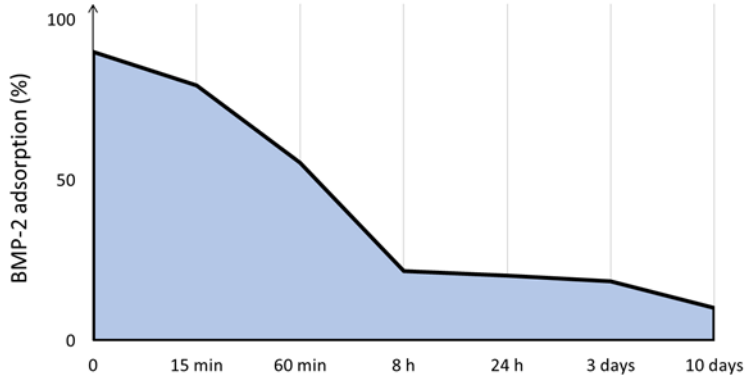

Figure 2.22. – Collagen sponge BMP-2 adsorption dynamics. Adapted from Fujioka-Kobayashi et al. (2017) [98].

As $\lambda_{rel}(0)$ = 0.901, it is possible to observe that 9.9% of the BMP-2 provision is retained from the sponge and it was not released during the healing process.

2.3.3. BMP-2 enhancement of biological activities

BMP-2 driven enhancement of cellular activity was simulated to investigate its role in the promotion of bone defect healing. Ribeiro et al. (2015) described the relationships between cell activity and the relative BMP-2 concentration in the surroundings [74]. In first instance, BMP-2 influenced MSCs and osteoblasts migration according to a dose-dependent law, which is characterized by maximum effect at BMP-2 concentration of 1 ng mL^{-1} [74] (Figure 2.23.). The proliferation of MSCs was also upregulated by the presence of BMP-2, with a peak at 200 ng mL^{-1} [74] (Figure 2.23.). Moreover, the capacity of osteoblasts to produce bone tissue was upregulated by BMP-2. In this latter case, BMP-2 efficacy grows with its concentration until reaching a steady-state at concentrations over 100 ng mL^{-1} [74] (Figure 2.23.).

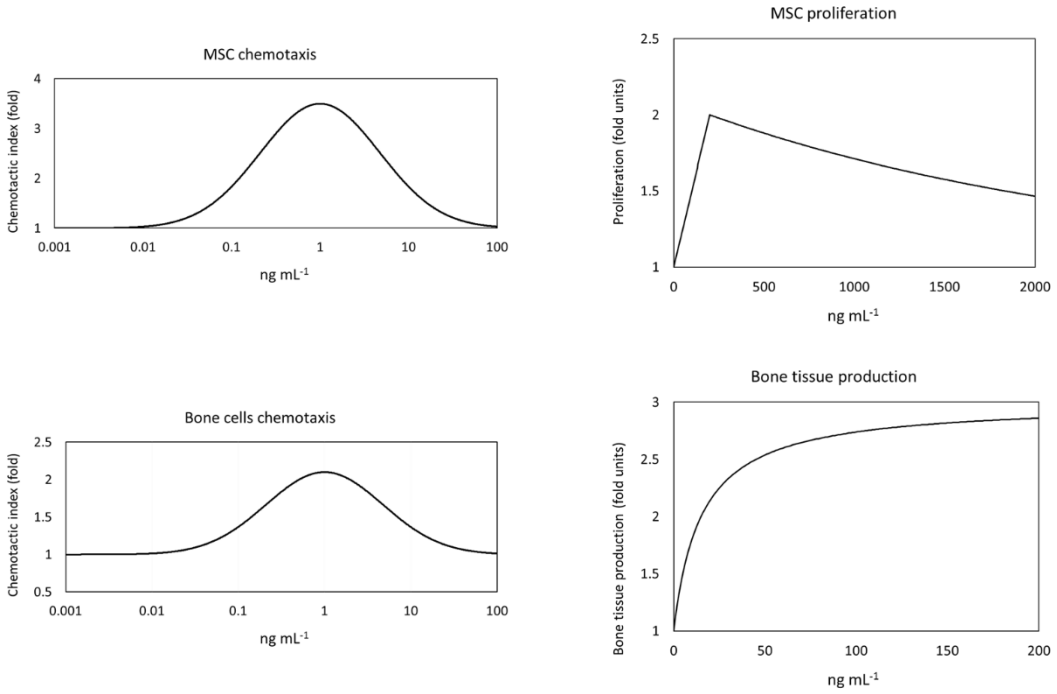

Figure 2.23. – BMP-2 concentration effect on multiple aspects at cellular level. Adapted from Ribeiro et al. (2015) [74].

BMP-2 effect on cell migration and proliferation were implemented in the cellular distribution agent model. The chemotaxis and proliferation ratio of the cells dynamically varied during the simulation, depending on the BMP-2 concentration model. To implement this, another parameter was assigned to each cell of the agent model: the value of BMP-2 concentration at that location, calculated in the BMP-2 model ($[BMP2]$). All the 125 cells that belonged to the same BMP-2 agent were characterized by the same $[BMP2]$ value.

BMP-2 chemotaxis was implemented as an attractive effect on cells to migrate to regions where the BMP-2 chemotactic index was higher. The algorithms that described the chemotactic effect on MSCs and osteoblasts were both adapted from Ribeiro et al. (2015) [74]. BMP-2 was observed to have a maximum effect when its concentration is 1 ng mL^{-3} [48]. At this concentration, BMP-2 produces 3.5 and 2.2-fold increase in the chemotactic index of MSCs and osteoblasts, respectively. The algorithm evaluated the influence of BMP-2 concentration on cell chemotaxis by assigning a chemotactic factor ($c.f.$) to each agent of the BMP-2 model. This factor depended exclusively on the concentration of BMP-2 associated with that element [74]:

$$c.f._{MSC}\,(x,y,z,t) = 1\ + 2.5 * \left(e^{-\left(\frac{\log([BMP2](x,y,z,t))}{2.5}\right)^2} \right) \qquad (16)$$

$$c.f._{OB}\,(x,y,z,t) = 1\ + 1.1 * \left(e^{-\left(\frac{\log([BMP2](x,y,z,t))}{2.5}\right)^2} \right) \qquad (17)$$

Before the cellular migration process (*§ 2.2.2., Cellular migration*) began, the algorithm checked the $c.f.$ of the agent the cell belonged to. It was compared with the values of the six agents in its immediate surroundings. If one of the surrounding agents had a higher $c.f.$ value than the agent the cell belonged to, the cell migrated in the direction of that agent. Otherwise, if the cell belonged to the agent with maximum $c.f.$, it did not migrate at all. If more agents shared the maximum value of $c.f.$, with an allowance range of 10%, the migration direction was randomly chosen only between those elements (Figure 2.24.).

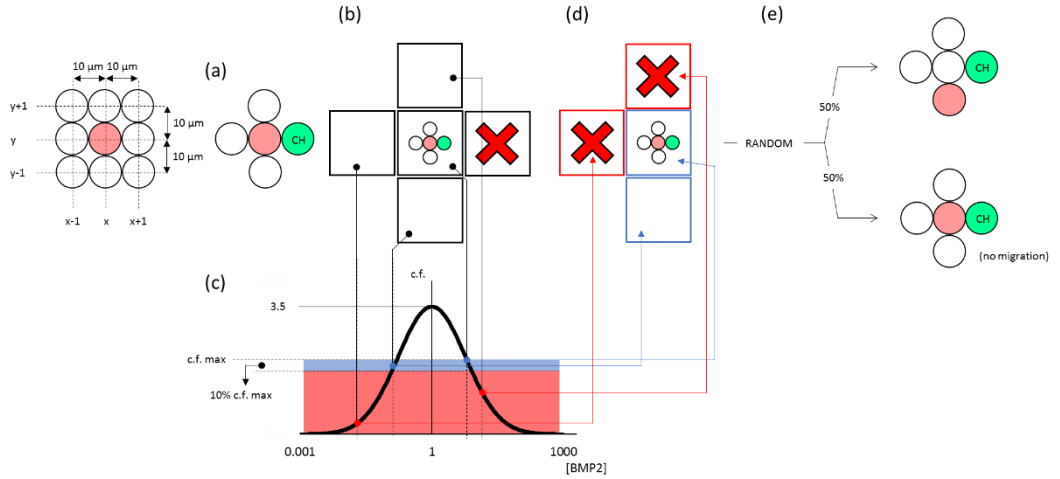

Figure 2.24. – Schematic representation of how the effect of BMP-2 chemotaxis was applied in this model. (a): The migrating cell (pink) checks its surroundings for available spaces (white) in the cell distribution agent-based model; (b): BMP-2 concentration was obtained from the adjacent agent-based model regions and from the one where the migrating cell belongs. The regions in direction of unavailable migration (red cross due to chondrocyte CH presence) were excluded; (c): Chemotaxis factor ($c.f.$) was determined for each region according to specific BMP-2 concentration [74] and maximum value was determined ($c.f.max$); (d): The BMP-2 regions where $c.f.$ was lower than 90% $c.f.max$ were further excluded (red crosses); (e): Migration was randomly assigned in the directions of the remaining BMP-2 regions. The cell could also not migrate if $c.f.$ of the actual BMP-2 region is higher than 90% of the $c.f.max$. Note: The representation is simplified in two dimensions.

Additionally, the proliferation ratio of MSCs was upregulated for each cell as a function of the specific $[BMP2]_{cell}$. To integrate this, the proliferation algorithm was modified where the proliferation ratio was transformed into a proliferation probability. This change was necessary because the proliferation ratio was affecting the global behavior at the cellular level: with a proliferation ratio of 0.60, 60% of all the cells were randomly chosen and proliferated. The proliferation probability allowed to be specific for each cell and to affect its capacity to proliferate as a function of its specific $[BMP2]_{cell}$. In this way, the number of proliferated cells depended on the local BMP-2 concentration.

The rule that regulated MSC proliferation probability (π_{prol}) was derived from Ribeiro et al. (2015) [74]:

$$\pi_{prol} = \begin{cases} 0.6 + \dfrac{[BMP2]_{cell} * 0.4}{200\dfrac{ng}{cm^3}} & if\ [BMP2]_{cell} \leq 200\dfrac{ng}{cm^3} \\ 0.6 + 0.4 * 1.0443^{\frac{-[BMP2]_{cell} - 200\frac{ng}{cm^3}}{100\frac{ng}{cm^3}}} & if\ [BMP2]_{cell} > 200\dfrac{ng}{cm^3}{}^3 \end{cases} \quad (18)$$

The proliferation probability for MSCs spanned between 60% to 100% (Figure 2.25.).

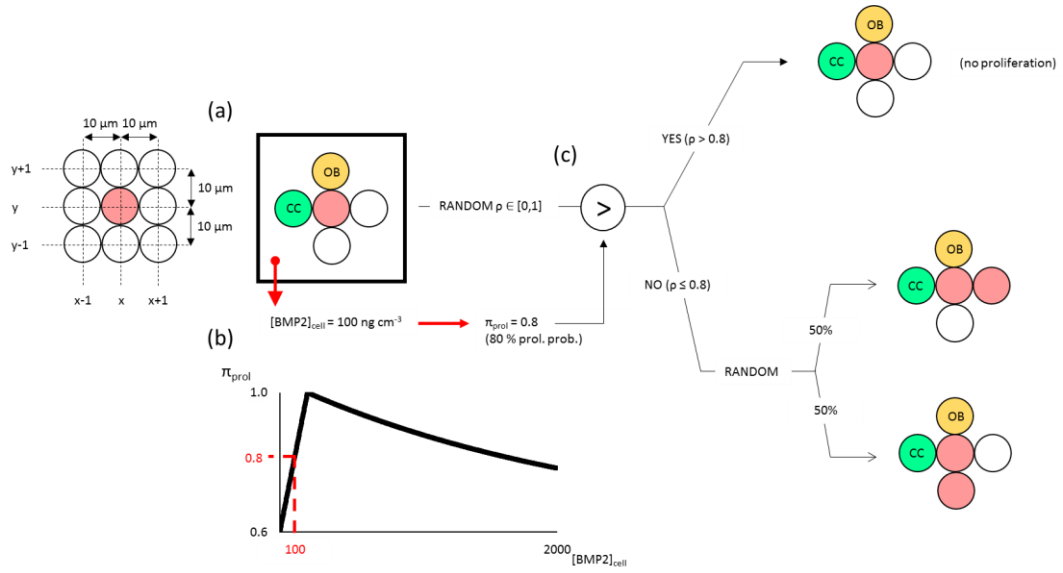

Figure 2.25. – Schematic representation of how the effect of BMP-2 on cellular proliferation enhancement was applied in this model. (a): The BMP-2 concentration ($[BMP2]_{cell}$) was obtained from the region including the proliferating cell (pink) position; (b): According to Ribeiro et al. (2015), [BMP2]cell determined the proliferation probability (π_{prol}) [74]; (c): Random value ρ was randomly picked between 0 and 1 and compared with π_{prol} to determine if the cell was allowed to proliferate ($\rho \leq \pi_{prol}$) or not ($\rho > \pi_{prol}$). Note: The representation is simplified in two dimensions.

The algorithm randomly chose one MSC and evaluated its proliferation probability π_{prol} according to its specific $[BMP2]_{cell}$. To test the cell proliferation capacity, a value ρ between 0.00 and 1.00 was randomly chosen. A new ρ value was randomly obtained for every test performed. If $\rho > \pi_{prol}$, the cell did not proliferate. Otherwise, if $\rho \leq \pi_{prol}$, the cell proliferated

according to the aforementioned rules (*§ 2.2.2., Cellular proliferation*). The algorithm checked the proliferation capacity of all the MSCs and osteoblasts within the agent-based model. The π_{prol} minimum values were adapted from the proliferation daily-ratio used when no BMP-2 effect was investigated (*§ 2.2.2., Cellular proliferation*). The value of π_{prol} had to be reduced by a proper factor if the iteration period was shorter than one day (when 2-hour iteration period was investigated, π_{prol} value was divided by a factor 12).

To include the effect of BMP-2 on promoted bone tissue production, the concentration of BMP-2 regulated the quantity of bone tissue produced by osteoblasts. The bone tissue production rate dynamically changed for each osteoblast. The following rule, derived by Ribeiro et al. (2015) [74], defines how the production quantity increased according to $[BMP2]_{OB}$:

$$BTP_{OB}\ (f.u.) = 1 + \frac{2 * [BMP2]_{OB}}{15\frac{ng}{cm^3} + [BMP2]_{OB}} \tag{19}$$

The BTP_{OB} value was then multiplied by the bone tissue matrix production ratio to evaluate the amount of tissue produced by the osteoblast during the iteration under the BMP-2 conditions.

2.4. Computer models set-up

The multiscale computer models investigated mechanical and biological factors influencing the bone healing process in two different compromised conditions: 1) aging approach and 2) critical size defect. In addition, the mechano-regulation of large bone defect healing augmented with BMP-2 was investigated.

2.4.1. Mechano-regulation of bone healing in mice

Bone healing is a process driven by the mechanical environment within the callus region. Many *in vivo* studies investigated the differences in healing progression under different mechanical conditions such as fixator stiffness, gap size or allowed interfragmentary movement. *In vivo*, it is experimentally challenging to measure the distribution of the mechanical stimuli within the callus region. In this study, a FE model was developed to study temporal changes in the mechanical conditions within the callus in a 0.5 mm mouse osteotomy. The aim was to predict the strain and fluid flow distribution within the healing region. The Prendergast et al. (1997) biomechanical regulatory model [57], observed to correctly predict bone healing in rats [61], was implemented in the model to regulate cell differentiation in mice under both rigid and semirigid fixation conditions. Predicted tissue distributions at day 7, 14 and 21 post-operation were compared to histological experimental data from adult mice (26-week old) [86].

2.4.2. Age-related alterations in the mechanobiological regulation of bone healing

Many biological processes (migration, proliferation, etc.) at the cellular level have been reported to be influenced by aging. To investigate the relative role of age-related alterations at the cellular level on tissue patterning over the course of healing, a DOE method [99] was used. The method combined the age-related effects of multiple factors on the global outcome of the bone healing model, allowing to identify the ones playing a major role in affecting the process. An orthogonal array was used to reduce the number of experiments (simulations in this case) needed. Fifteen age-related cellular factors (P1 – P15) were selected to investigate their role at the tissue level alteration of bone healing with aging (Table 2.9.). Two levels were associated with each parameter: adult (*+1*) and elderly (*-1*). The values that were previously reported to describe the cellular distribution agent-based model (*§ 2.2.2.*) were used as input values for the adult level. To simulate the compromising effect of aging, the parameter values were either halved (migration, proliferation and differentiation rates, and initial cell density) or doubled (apoptosis rate) in the elderly level (Table 2.9.).

	Parameter	Level	
		Adult (*+1*)	Elderly (*-1*)
Initial MSC density			
%			
Periosteal	P1	30	15
Marrow	P2	30	15
Migration rate			
μm day^{-1}			
MSCs	P3	720	360
Fibroblasts	P4	720	360
Differentiation rate			
day^{-1}			
MSCs	P5	0.30	0.15
Proliferation rate			
day^{-1}			
MSCs	P6	0.60	0.30
Fibroblasts	P7	0.55	0.275
Chondrocytes	P8	0.20	0.10
Osteoblasts	P9	0.30	0.15
Apoptosis rate			
day^{-1}			
MSCs	P10	0.05	0.10
Fibroblasts	P11	0.05	0.10
Chondrocytes	P12	0.10	0.20
Osteoblasts	P13	0.16	0.32

Table 2.9. – Cellular activity parameters investigated on two levels: adult (+1) and elderly (-1).

Two parameters were further investigated to include the effect of aging on tissue stiffening and on reduced cellular mechanosensitivity. Age-related tissue stiffening (P14) was investigated by increasing the baseline Young's modulus of all the biological materials by +20%. Reduced cellular mechanosensitivity (P15) was simulated in the elderly level by moving to higher mechanical stimuli the boundaries of the MSC differentiation rule (*Appendix D*).

Taguchi orthogonal arrays combine the two-levels parameters on each experiment [99]. This method minimizes the number of simulations necessary to investigate the interactions between all the parameters. Sixteen different simulations (S1 to S16) were designed to investigate the contribution of fifteen cellular parameters to alterations on tissue patterning over the course of healing. Each one of the simulations was characterized by a combination of parameters associated with their adult (*+1*) or elderly level (*-1*), as reported in Table 2.10.

	P1	P2	P3	P4	P5	P6	P7	P8	P9	P10	P11	P12	P13	P14	P15
S1	*-1*	*-1*	*-1*	*-1*	*-1*	*-1*	*-1*	*-1*	*-1*	*-1*	*-1*	*-1*	*-1*	*-1*	*-1*
S2	*-1*	*-1*	*-1*	*-1*	*-1*	*-1*	*-1*	*+1*	*+1*	*+1*	*+1*	*+1*	*+1*	*+1*	*+1*
S3	*-1*	*-1*	*-1*	*+1*	*+1*	*+1*	*+1*	*-1*	*-1*	*-1*	*-1*	*+1*	*+1*	*+1*	*+1*
S4	*-1*	*-1*	*-1*	*+1*	*+1*	*+1*	*+1*	*+1*	*+1*	*+1*	*+1*	*-1*	*-1*	*-1*	*-1*
S5	*-1*	*+1*	*+1*	*-1*	*-1*	*+1*	*+1*	*-1*	*-1*	*+1*	*+1*	*-1*	*-1*	*+1*	*+1*
S6	*-1*	*+1*	*+1*	*-1*	*-1*	*+1*	*+1*	*+1*	*+1*	*-1*	*-1*	*+1*	*+1*	*-1*	*-1*
S7	*-1*	*+1*	*+1*	*+1*	*+1*	*-1*	*-1*	*-1*	*-1*	*+1*	*+1*	*+1*	*+1*	*-1*	*-1*
S8	*-1*	*+1*	*+1*	*+1*	*+1*	*-1*	*-1*	*+1*	*+1*	*-1*	*-1*	*-1*	*-1*	*+1*	*+1*
S9	*+1*	*-1*	*+1*	*-1*	*+1*	*-1*	*+1*	*-1*	*+1*	*-1*	*+1*	*-1*	*+1*	*-1*	*+1*
S10	*+1*	*-1*	*+1*	*-1*	*+1*	*-1*	*+1*	*+1*	*-1*	*+1*	*-1*	*+1*	*-1*	*+1*	*-1*
S11	*+1*	*-1*	*+1*	*+1*	*-1*	*+1*	*-1*	*-1*	*+1*	*-1*	*+1*	*+1*	*-1*	*+1*	*-1*
S12	*+1*	*-1*	*+1*	*+1*	*-1*	*+1*	*-1*	*+1*	*-1*	*+1*	*-1*	*-1*	*+1*	*-1*	*+1*
S13	*+1*	*+1*	*-1*	*-1*	*+1*	*+1*	*-1*	*-1*	*+1*	*+1*	*-1*	*-1*	*+1*	*+1*	*-1*
S14	*+1*	*+1*	*-1*	*-1*	*+1*	*+1*	*-1*	*+1*	*-1*	*-1*	*+1*	*+1*	*-1*	*-1*	*+1*
S15	*+1*	*+1*	*-1*	*+1*	*-1*	*-1*	*+1*	*-1*	*+1*	*+1*	*-1*	*+1*	*-1*	*-1*	*+1*
S16	*+1*	*+1*	*-1*	*+1*	*-1*	*-1*	*+1*	*+1*	*-1*	*-1*	*+1*	*-1*	*+1*	*+1*	*-1*

Table 2.10. – Orthogonal matrix with the 16 simulation conditions as combination of the parameters on two levels.

The mouse osteotomy model was run for each of the sixteen experiments under both rigid and semirigid fixator conditions. The combination of adult and elderly values for the parameters involved in the investigation followed the orthogonal arrays reported in Table 2.10. [99]. For example, S1 was characterized by all the fifteen parameters altered due to aging (level *-1*) while

S2 was characterized by parameters P1 to P7 set to elderly level values (*-1*) and the parameters P8 to P15 kept unaltered to adult level values (*+1*).

Analysis of variance was performed on bone tissue area predicted by the *in silico* model at 7, 14 and 21 days for each of the sixteen simulations under both rigid and semirigid conditions. This allowed to quantify each parameter contribution to the alteration of bone tissue formation in elderly mice. The sum of the squares of deviation about the mean (SSP) was calculated as follows:

$$SSP = \sum_{i=1}^{n} N_{P,i}\left(\bar{y}_{P,i} - \bar{y}\right)^2 \tag{20}$$

Where n is the number of levels considered for the DOE, in this case n = 2 (adult and elderly level). $N_{P,i}$ is the number of experiments where the specific parameter P is set to level i. In this study the value is always set to eight, as each one of the parameters is set to the adult level (i = *+1*) in eight experiments and set to the elderly level (i = *+1*) in eight experiments. $\bar{y}_{P,i}$ is the average value of the investigated factor (bone tissue area in mm^2, in this case) between all the results of the experiments in which the parameter P was set to level i. $\bar{y}$ is the average value of the investigated factor of all the experiments. In addition, the percentage of the total sum of squares (TSS) was calculated for each parameter:

$$TSS = 100\% * \frac{SSP}{\sum_{i=1}^{N}(y_i - \bar{y})^2} \tag{21}$$

Where N is the number of experiments, in this case N = 16. y_i is the value of the investigated factor (bone tissue area in mm^2) as result of experiment i. The TSS weighted the contribution of every single parameter to the variance and measured the "importance" of each parameter on the alteration of bone healing [100].

At each time-point and under both fixator conditions, the three parameters with the highest TSS values were identified as the most influential ones. Thereafter, the comparison with *in vivo* data was performed from a qualitative

and quantitative point of view by running extra bone healing models where all the parameters were assigned to their adult level value except for combinations of two or all the three most influential parameters, which were assigned to their specific elderly level value. Bone and cartilage area were predicted for each time-point and compared with experimental data from elderly mice. Simulation results and experimental histological data at day 7, 14 and 21 post-operation under both rigid and semirigid external fixation were compared.

2.4.3. Investigation of BMP-2 effect on bone defect healing in rats

To investigate the biological role of BMP-2 to compromised bone defect healing in rats, an *in silico* model reproduced the case scenarios investigated *in vivo* by Schwarz et al. (2013) [45]. The model was characterized by a 5 mm critical bone defect to simulate the same challenging healing conditions of the *in vivo* study. Four different case studies were examined, following the conditions of the experiment: (a) *control case*, (b) *only load*, (c) *only BMP-2*, (d) *BMP-2 + load*. Case studies (b) and (d) were characterized by additional application of 500 μm displacement of the bone in the axial direction (compression) every 7 complete day-iterations to simulate external mechanical stimulation on weekly basis [45]. The fixator bridge was temporarily removed from the model during the external mechanical stimulation, as described in the experimental setup [45]. For case studies (c) and (d) an initial exogenous BMP-2 concentration of 50 μg was provided within the osteotomy gap, simulating the conditions of BMP-2 treatment [45]. BMP-2 was gradually dosed according to simulate collagen sponge release. An additional model was run for the case study (c) considering free BMP-2 since the first iteration to investigate the importance of the collagen sponge on defect healing. The interaction between bone healing promoters was investigated on multiple length- and time-scales to highlight the role of BMP-2 and mechanical treatments on the successful regeneration of critical defects. Spatial distribution of bone tissue predicted at 2, 4 and 6 weeks post-operation

for all the case studies was compared with μCT images obtained experimentally [45]. In addition, histomorphometry data at 6 weeks post-operation was quantitatively confronted with bone tissue area predicted at the same time-point. In addition, two further models were developed to investigate the behaviors observed *in vivo* that the current models were not able to predict. The alternative models are described in the following sections.

External loading regulation of BMP-2 release and diffusion

To investigate the mechanical effect of external loading on BMP-2 dynamics, increased release and faster diffusion of BMP-2 were simulated within the callus when weekly when mechanical loading was provided. In the original model, the mechanical stimulation only operated at the cellular level by regulating MSC differentiation. In the first alternative model, the collagen sponge gradual release of BMP-2 followed a different algorithm. The additional compressive stress provided by the extra mechanical stimulation led to a higher release of BMP-2. Over the normal release dynamics [98], every weekly iteration, the sponge released a higher quantity of BMP-2 to simulate the increased compressive stress. The additional release was dependent to the fold-increase compressive stress due to additional stimulation. This resulted in stepped dynamics as reported in Figure 2.26.

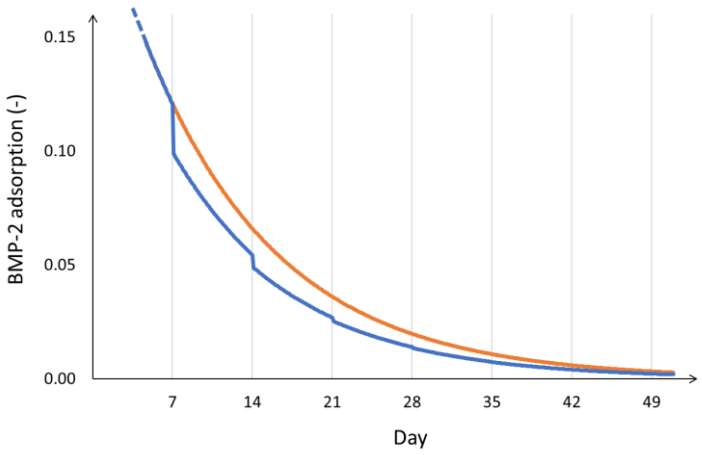

Figure 2.26. – Dynamics of BMP-2 adsorption over time for a normal collagen sponge (orange) and a mechanically stimulated sponge release (blue).

Additionally, the new model implemented the effect of the compression on the BMP-2 motion within the tissues inside the defect opening. In detail, at the time-points when additional loading was provided, the diffusion coefficient D, which regulated the spatial diffusion of BMP-2, was doubled. The diffusion coefficient was not affected in the iterations when normal gait mechanics were simulated. The magnitude of the additional release and the 2-fold increase in diffusivity were arbitrarily chosen to test the mechano-driven regulation of BMP-2 mobility in the tissues.

Limited cellular migration and proliferation in large bone defect healing

Based on experimental observations on the lack of cellular activity due to impaired vascularization in large bone defects [101] [102], the biological activities at the cellular level were downregulated in the large defect model. In fact, in the main model, the defect size influenced healing only from a mechanic point of view. The second alternative model was characterized by a compromised biological environment at the cellular level due to the critical healing conditions. To implement it, the cellular activities in the agent-based model were limited to happen only in the first stages of healing. A test was performed in the model by limiting cellular migration and proliferation to the first 10 days post-operation. In detail, all the cellular migration and proliferation ratios were set to zero after 10 days of simulation. This meant that, after that time-point, all the cells within the defect opening were not able to migrate and proliferate anymore. Under BMP-2 treatment, the condition was valid only in the regions where BMP-2 was not having any sort of effect on migration and proliferation. In the regions where these processes were enhanced by BMP-2 presence, the algorithm was adapted to have cellular null ratio at BMP-2 physiological concentration.

3
RESULTS

3.1. Age-related alterations in the mechanical regulation of bone healing

3.1.1. Over two times higher mechanical stimuli within a mouse osteotomy under semirigid compared with rigid fixation conditions

In the mouse FE model, under gait mechanical loading conditions, predicted compressive strains and fluid flow velocities were highest within the osteotomy gap, while lower magnitudes were predicted at the periosteal side. Immediately post-osteotomy, average compressive principal strains within the endosteal region were predicted to be 0.179±0.045 in calluses stabilized by rigid fixation (Figure 3.1A). Under semirigid external fixation, the average compressive principal strains in the endosteal region were more than two times higher (0.480±0.155) (Figure 3.1B). Slightly higher strains were predicted inter-cortically in the medial side compared with the lateral side (fixator side), both under rigid and semi-rigid fixation. Also in the intercortical region, average FE-estimated compressive strains were more than two times higher under semirigid than under rigid fixation (rigid fixator intercortical medial side: 0.260±0.047, rigid fixator intercortical lateral side: 0.225±0.049, semi-rigid fixator intercortical medial side: 0.701±0.143, semi-rigid fixator intracortical lateral side: 0.613±0.141) (Figure 3.1.). Lower mechanical stimuli were predicted in the periosteal region. Compressive principal strains in the periosteal region showed three-fold increase under semi-rigid compared with rigid fixation (rigid fixator periosteal medial side: 0.135±0.060, rigid fixator periosteal lateral side: 0.115±0.052, semi-rigid fixator periosteal medial side: 0.473±0.167, semi-rigid fixator periosteal lateral side: 0.409±0.162) (Figure 3.1.).

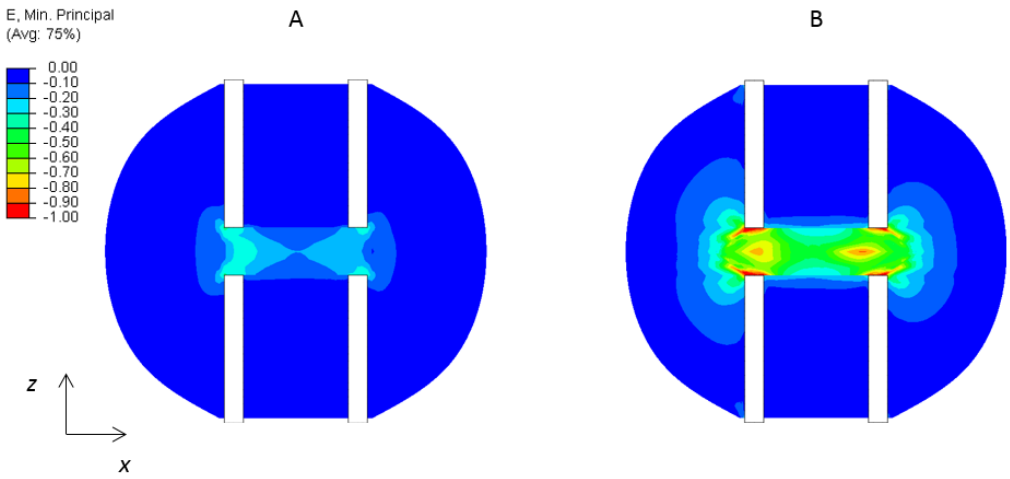

Figure 3.1. – Compressive principal strain distribution predicted within the callus immediately after surgery under rigid (A) and semirigid (B) external fixator stabilization.

Under rigid conditions, predicted fluid flow velocity was characterized by a symmetrical distribution where the position of the external fixator did not have an influence on the induced fluid flow velocity (intercortical medial side: 0.0018±0.0011 μm s^{-1}, intercortical lateral side: 0.0016±0.0010 μm s^{-1}, periosteal medial side: 0.0014±0.0011 μm s^{-1}, periosteal lateral side: 0.0013±0.0009 μm s^{-1}) (Figure 3.2A). Under semirigid conditions, the higher compressive stresses favored the movement of interstitial liquid within the osteotomy gap. Two-time faster fluid motion was predicted intercortically under semirigid conditions (intercortical medial side: 0.0036±0.0032 μm s^{-1}, intercortical lateral side: 0.0038±0.0037 μm s^{-1}) (Figure 3.2B). Moreover, three-time higher values characterized fluid flow velocity in periosteal elements under more flexible conditions (periosteal medial side: 0.0061±0.0035 μm s^{-1}, periosteal lateral side: 0.0071±0.0046 μm s^{-1}) (Figure 3.2B).

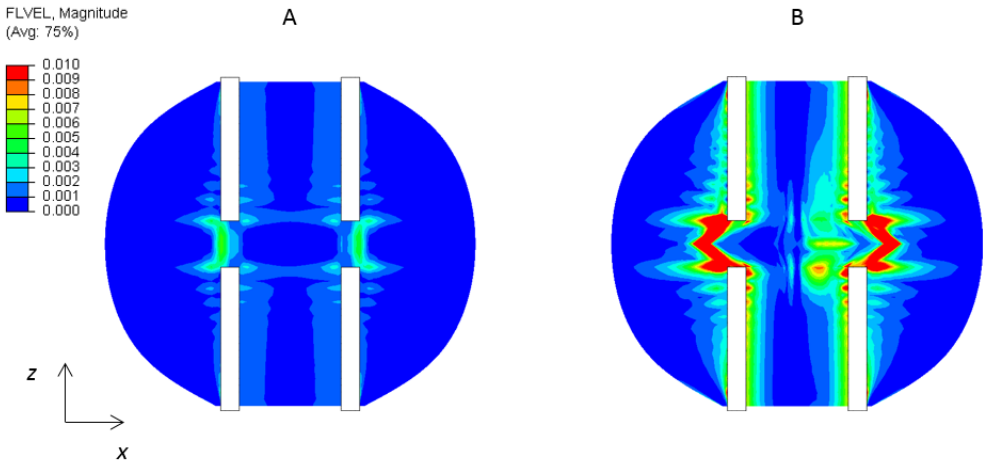

Figure 3.2. – Interstitial fluid flow velocity (µm s^{-1}) predicted within the osteotomy gap post-surgery under rigid (A) and semirigid (B) external fixator stabilization.

Due to its challenging nature, the mechanical environment within the osteotomy gap was not investigated *in vivo*. However, the experimental mechanical testing conditions used to evaluate the stiffness of the external fixators were recreated *in silico* to validate their effect on the mechanical stabilization of the osteotomy. *In silico*, an axial stiffness of 18.22 N mm^{-1} was predicted for the rigid fixator, while for the semirigid fixator an axial stiffness of 2.65 N mm^{-1} was predicted. These results agree with the experimental data [86]: rigid: 16.94±0.87 N mm^{-1}; semirigid: 2.82±0.09 N mm^{-1} (Figure 3.3.).

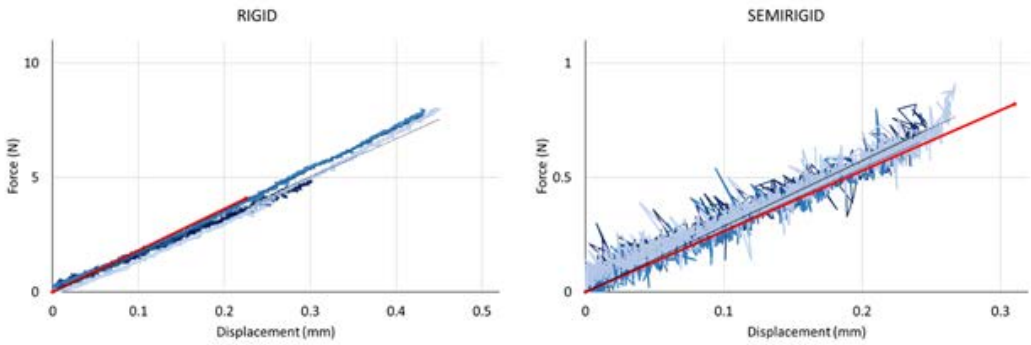

Figure 3.3. – Quantitative comparison between in silico *(red) and* in vivo *(blue shades [86]) measurements of axial stiffness of rigid (left) and semirigid (right) fixators.*

3.1.2. Bone healing occurs under higher mechanical stimuli in mice than in larger animals

The general mechano-regulatory rule, which correctly predicted bone healing in rat [61] was not able to reproduce the tissue dynamics in the mouse model. The ranges of mechanical stimuli that were able to explain tissue differentiation in rats were higher in mice [61]. This difference resulted in the incorrect prediction of a high amount of fibrous tissue within the osteotomy gap under rigid external fixation at 14 and 21 weeks post-operation (Figure 3.4.). The non-union condition shown by the *in silico* model did not reproduce the healing results observed experimentally [103]. Under rigid fixation, mice bone osteotomies were observed to heal within weeks without excessive fibrous tissue production within the osteotomy gap. Moreover, the *in silico* model showed periosteal cartilage formation at the initial stages (Figure 3.4.), which was not observed in histological data.

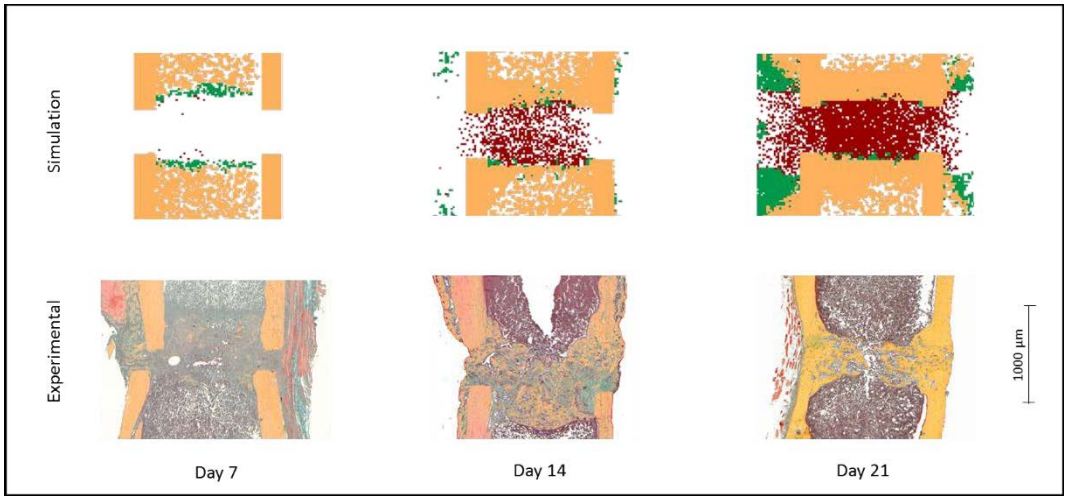

Figure 3.4. – Top: Tissue patterning predicted in mouse osteotomy healing model under standard mechano-regulation rules according to Prendergast et al. (1997) [57]. Bottom: Histological images from adult mice. Results are shown at 7, 14 and 21 days post-osteotomy under rigid fixation conditions. Prediction tissue patterning colors were chosen analogously to histology staining: dark yellow: bone; green: cartilage; dark red: fibrous tissue.

Quantitative results showed increasing fibrous tissue production during the first 6 weeks post-operation under rigid conditions (Figure 3.5.). From week 6 on, the predicted fibrous tissue area remained almost constant and bone tissue formation became preponderant (Figure 3.5.).

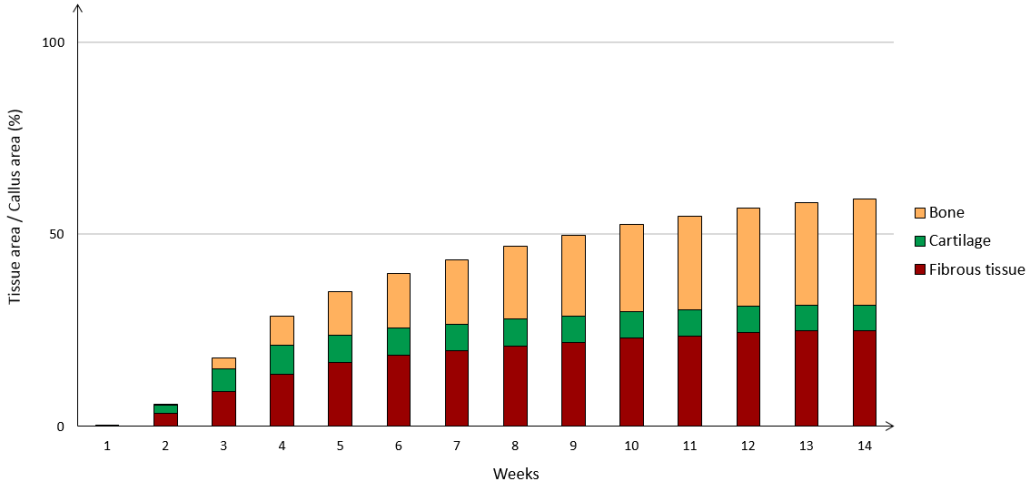

Figure 3.5. – Quantitative results of tissue ratios within the callus domain predicted weekly until week 14 post-operation.

Mechano-regulation of mouse bone healing under semirigid conditions was omitted from the investigation as even higher mechanical stimuli were predicted within the callus gap under those conditions. Under higher mechanical stimuli, the use of the investigated mechano-regulation rules would favor even more the differentiation of MSCs into fibroblasts and the consequent production of fibrous tissue within the osteotomy.

3.1.3. Bone healing is predicted in silico when the mechano-regulation rules are adapted to higher mechanical stimuli

Experimentally observed bone healing in mice was successfully predicted *in silico* by varying the mechano-regulatory rules that explained bone healing in larger animals [61], where MSC differentiation took place under higher mechanical stimuli. Computer model simulations of the bone healing process predicted the overall progression of tissue patterning over the course of

healing in mice under both rigid and semirigid fixation for the first 21 days post-operation.

Under rigid fixation, the model predicted initial endosteal bone formation and the formation of cartilage within the osteotomy gap during the first 14 days post-surgery. No substantial differences were observed, *in silico*, in tissue patterning between days 14 and 21 (Figure 3.7A). Qualitative comparison between *in vivo* and *in silico* tissue patterning showed good correspondence of the increasing production of bone within the endosteal cavity in the first 2 weeks post-operation (Figure 3.7A).

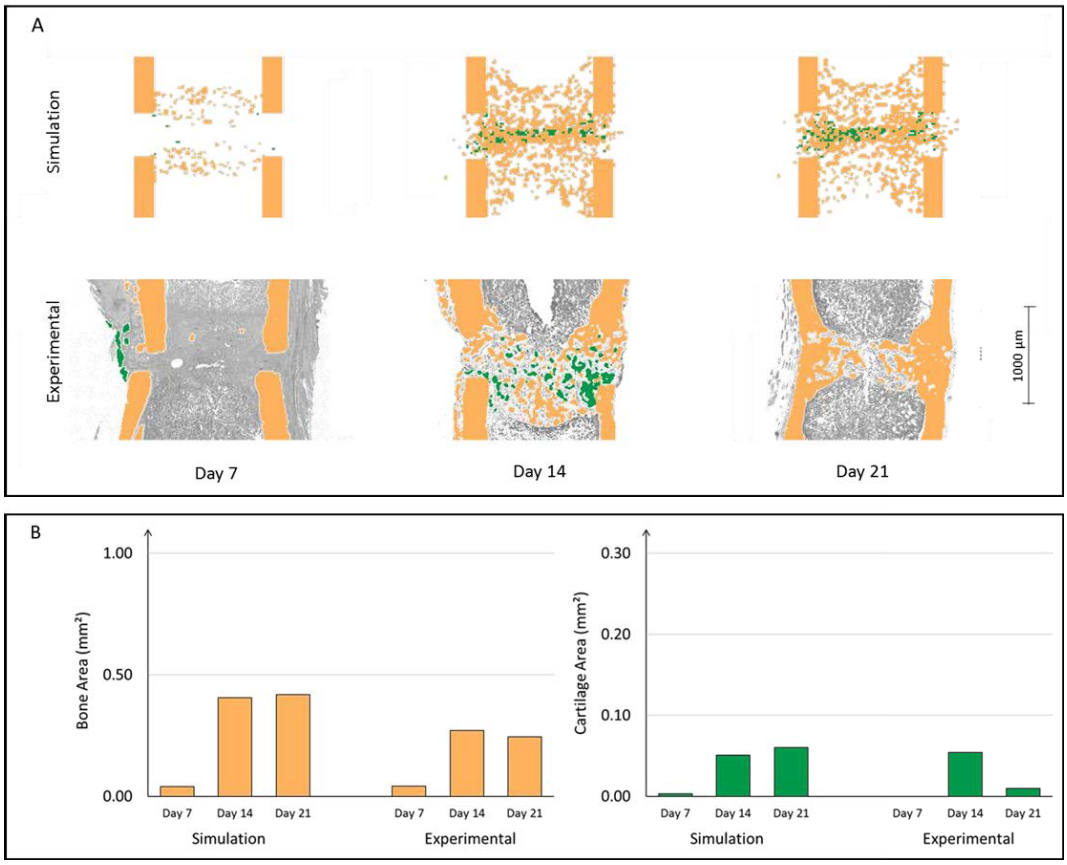

Figure 3.6. – Comparison between simulation and experimental tissue distribution (A) and tissue area extension (B) within the osteotomy gap of bone osteotomy healing in mice under rigid conditions at 7, 14 and 21 days post-operation. Prediction tissue patterning colors were chosen analogously to histology staining: dark yellow: bone; green: cartilage.

Under semirigid fixation, both *in vivo* and *in silico*, bone bridging was not achieved, as cartilage was still present inside the osteotomy gap at 21 days post-surgery (Figure 3.7A).

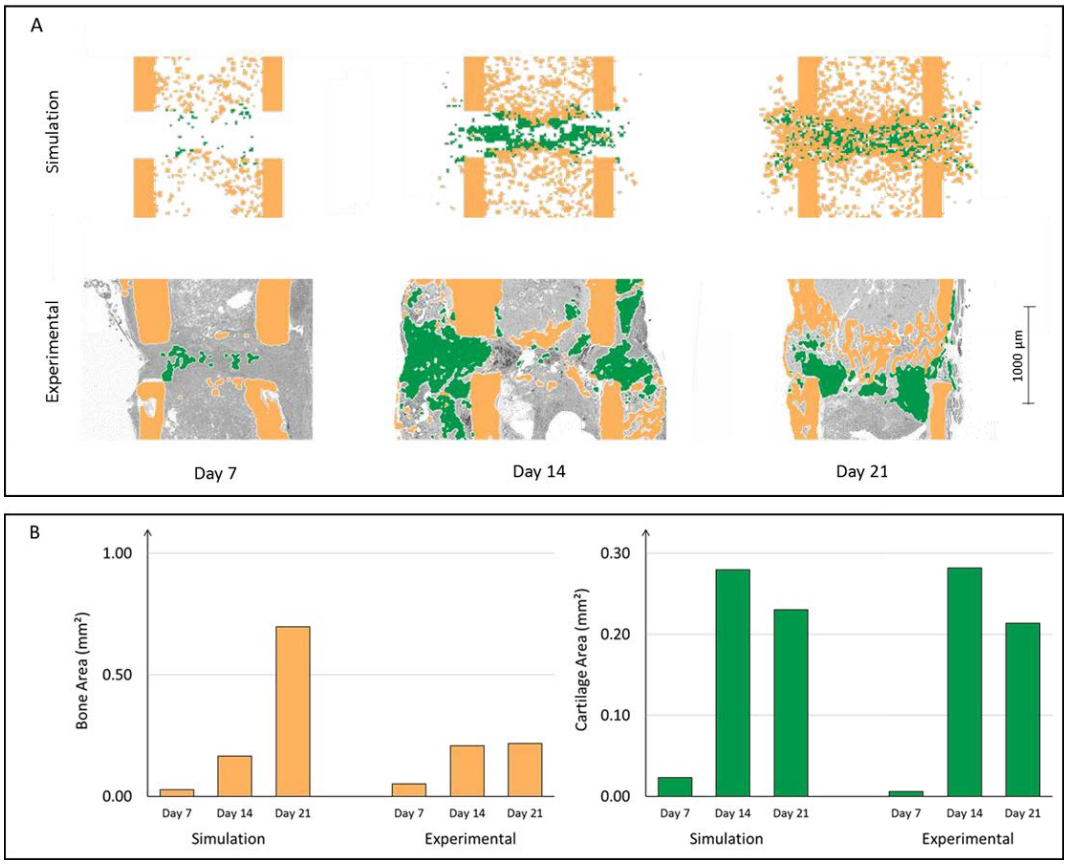

Figure 3.7. – Comparison between simulation and experimental tissue distribution (A) and tissue area extension (B) within the osteotomy gap of bone osteotomy healing in mice under semirigid conditions at 7, 14 and 21 days post-operation. Prediction tissue patterning colors were chosen analogously to histology staining: dark yellow: bone; green: cartilage.

Both *in vivo* and *in silico*, the mechanical conditions played a primary role in mouse bone healing, as the incapacity of bridging within 21 days was observed in mice only under flexible conditions. Moreover, a quantitative comparison between *in silico* predictions and experimental histomorphometry showed similar bone and cartilage tissue area increasing during the first two weeks of healing under rigid conditions (Figure 3.6B). Under semirigid conditions, quantitative results confirmed the over-estimation of bone tissue within the osteotomy gap at day 21 post-operation (*in vivo*: 0.21 mm^2, *in silico*: 0.70 mm^2)

(Figure 3.7B). Cartilage tissue area under semirigid conditions was similar *in vivo* and *in silico* at every time-point (Figure 3.7B).

3.1.4. Age-related effect on bone healing in mice can be described as a reduction of cellular mechanosensation.

A DOE approach was used to investigate the influence of age-related alterations at the cellular level on bone healing progression. Following an orthogonal array design (*§ 2.4.2.*), the most influencing parameters on the bone healing progression were identified. Bone tissue area prediction at 7, 14 and 21 days was used as a comparison between experiments and simulations, under rigid and semirigid fixator conditions. The results of all the simulations are reported in Table 3.1.

Simulation	Rigid Fixator			Semirigid Fixator		
	Day 7	Day 14	Day 21	Day 7	Day 14	Day 21
S1	0.01	0.07	0.04	0.01	0.15	0.18
S2	0.01	0.13	0.37	0.01	0.06	0.19
S3	0.11	0.36	0.30	0.02	0.14	0.50
S4	0.06	0.07	0.06	0.12	0.23	0.17
S5	0.01	0.12	0.13	0.01	0.06	0.39
S6	0.01	0.13	0.20	0.01	0.21	0.42
S7	0.01	0.06	0.07	0.01	0.10	0.32
S8	0.02	0.20	0.27	0.01	0.11	0.32
S9	0.01	0.10	0.35	0.01	0.06	0.24
S10	0.01	0.06	0.04	0.01	0.10	0.28
S11	0.01	0.10	0.10	0.01	0.16	0.30
S12	0.01	0.12	0.21	0.01	0.06	0.49
S13	0.20	0.16	0.14	0.37	0.37	0.30
S14	0.29	0.20	0.12	0.06	0.27	0.36
S15	0.08	0.24	0.15	0.01	0.10	0.45
S16	0.04	0.08	0.07	0.08	0.28	0.25

Table 3.1. - Bone tissue area (mm^2) predicted from each simulation at 7, 14 and 21 days under rigid and semirigid mechanical conditions.

Analysis of variance between the fifteen parameters used in this study highlighted the most influential parameters. The results provided as the sum of squares of the single parameter (SSP) and its percentage over the total sum of squares (TSS) are reported in Table 3.2. Higher TSS means a higher role of the parameter in the age-related alteration of predicted bone healing.

	Rigid Fixator						**Semirigid Fixator**					
	Day 7		Day 14		Day 21		Day 7		Day 14		Day 21	
	SSP mm^2	TSS %	SSP mm^2	TSS %	SSP mm^2	TSS %	SSP mm^2	TSS %	SSP mm^2	TSS %	SSP mm^2	TSS %
P1	0.01	10	0.00	0	0.00	2	0.01	6	0.01	5	0.00	1
P2	0.01	12	0.00	2	0.01	3	0.01	7	**0.02**	**13**	0.02	9
P3	**0.03**	**32**	**0.01**	**12**	0.00	1	**0.02**	**18**	**0.04**	**26**	0.01	5
P4	0.00	3	0.00	5	0.00	1	0.00	2	0.00	0	0.01	6
P5	**0.02**	**18**	0.00	4	0.00	0	**0.01**	**11**	0.01	5	0.00	1
P6	**0.02**	**16**	0.01	6	0.00	0	0.01	10	**0.02**	**13**	**0.03**	**18**
P7	0.00	3	0.00	1	0.00	0	0.00	2	0.00	0	0.00	2
P8	0.00	0	0.00	3	0.00	0	0.00	1	0.00	2	0.00	1
P9	0.00	0	0.00	0	**0.03**	**15**	0.01	6	0.00	1	0.01	6
P10	0.00	1	0.00	5	0.00	3	0.01	6	0.01	4	0.00	0
P11	0.00	0	**0.01**	**14**	0.00	0	0.00	1	0.00	0	**0.03**	**20**
P12	0.00	2	0.01	8	0.00	0	**0.01**	**11**	0.00	2	0.01	8
P13	0.00	1	0.00	1	**0.04**	**23**	0.01	4	0.00	1	0.00	2
P14	0.00	0	0.00	3	0.00	2	0.01	4	0.00	0	0.00	0
P15	0.00	3	**0.03**	**36**	**0.09**	**49**	0.01	10	**0.04**	**27**	**0.03**	**19**

Table 3.2. – Analysis of variance performed to quantify the significance of each parameter on bone tissue formation at 7, 14 and 21 days under rigid and semirigid mechanical conditions. The sum of the squares (SSP) and the percentage of the total sum of squares (TSS) is reported for each parameter. Note: the three most influential parameters at each time-point for both mechanical conditions are highlighted.

Under rigid conditions, at 7 days post-operation, the major role was played by age-related alterations in MSC migration (P3, TSS = 32%), differentiation (P5, TSS = 18%) and proliferation (P6, TSS = 16%) rates. At day 14, reduced cell mechanosensitivity played the main role (P15, TSS = 36%) followed by increased fibroblast apoptosis (P11, TSS = 14%) and decreased MSC migration (P3, TSS = 12%) rates. At day 21, the most influential aging parameter on bone tissue area was the reduction of cell mechanosensitivity (P15, TSS = 49%) followed by the increased osteoblast apoptosis ratio (P13, TSS = 23%) and the reduction of osteoblast proliferation (P9, TSS = 15%).

Under semirigid conditions, age-related alteration of MSC activities also played a primary role in the early stages of healing. At day 7, reduced MSC migration speed (P3, TSS = 18%) and differentiation rate (P5, TSS = 11%) were the most influential parameters in addition to increased chondrocyte apoptosis (P12, TSS = 11%). At day 14, reduced MSC migration speed still played a major role (P3, TSS = 27%) together with reduced cell mechanosensitivity (P15, TSS = 27%). The third most influential parameter was the reduced number of MSCs in the marrow cavity (P2, TSS = 13%). At day 21, three parameters were predicted to have similar importance in the effect on bone tissue area: reduced MSC mechanosensitivity (P15), increased fibroblast apoptosis rate (P11) and decreased MSC proliferation ratio (P6) were all characterized by TSS between 18% and 20%.

In vivo, aging had a higher effect on mouse bone healing under semirigid compared with rigid fixation. In detail, under semirigid conditions, elderly mice were characterized by enhanced healing at 21 days compared to adult mice [38]. According to this, the parameters that mostly altered bone healing under semirigid conditions were chosen as the most influential factors: reduced mechanosensitivity (P15), increased fibroblast apoptosis (P11) and reduced MSC proliferation (P6) rate. Thereafter, parameters P6, P11 and P15 were “aged” in couples (P6+P11, P6+P15, P11+P15) or as a whole triplet (P6+P11+P15), while the rest of parameters were kept to adult level. Computer simulations showed that the combinations P6+P15, P11+P15 and

P6+P11+P15 resulted in simular tissue distributions during the bone healing process, at the observation time-points. In detail, with rigid fixation, the model predicted small amounts of bone tissue (< 0.03 mm^2) and no cartilage within the callus at 7 days post-operation for all the investigated combinations (Figure 3.8.). Endosteal bone formation was observed in all the case studies at 14 days post-operation but major production characterized P6+P11 (0.31 mm^2) over the others (P6+P15: 0.16 mm^2, P11+P15: 0.20 mm^2, P6+P11+P15: 0.16 mm^2) (Figure 3.8.). Moreover, cartilage was observed at 14 days only for case P6+P11 (0.05 mm^2) (Figure 3.8.). Strong bone tissue formation was predicted to continue within the gap only for case P6+P11. In fact, at day 21 an increment of bone tissue area was observed for this case (0.40 mm^2), whereas bone area was subject to minor variations in the others (P6+P15: 0.19 mm^2, P11+P15: 0.21 mm^2, P6+P11+P15: 0.20 mm^2) (Figure 3.8.). At 21 days post-operation, the case P6+P11 was the only one that showed cartilage within the osteotomy gap (Figure 3.8.).

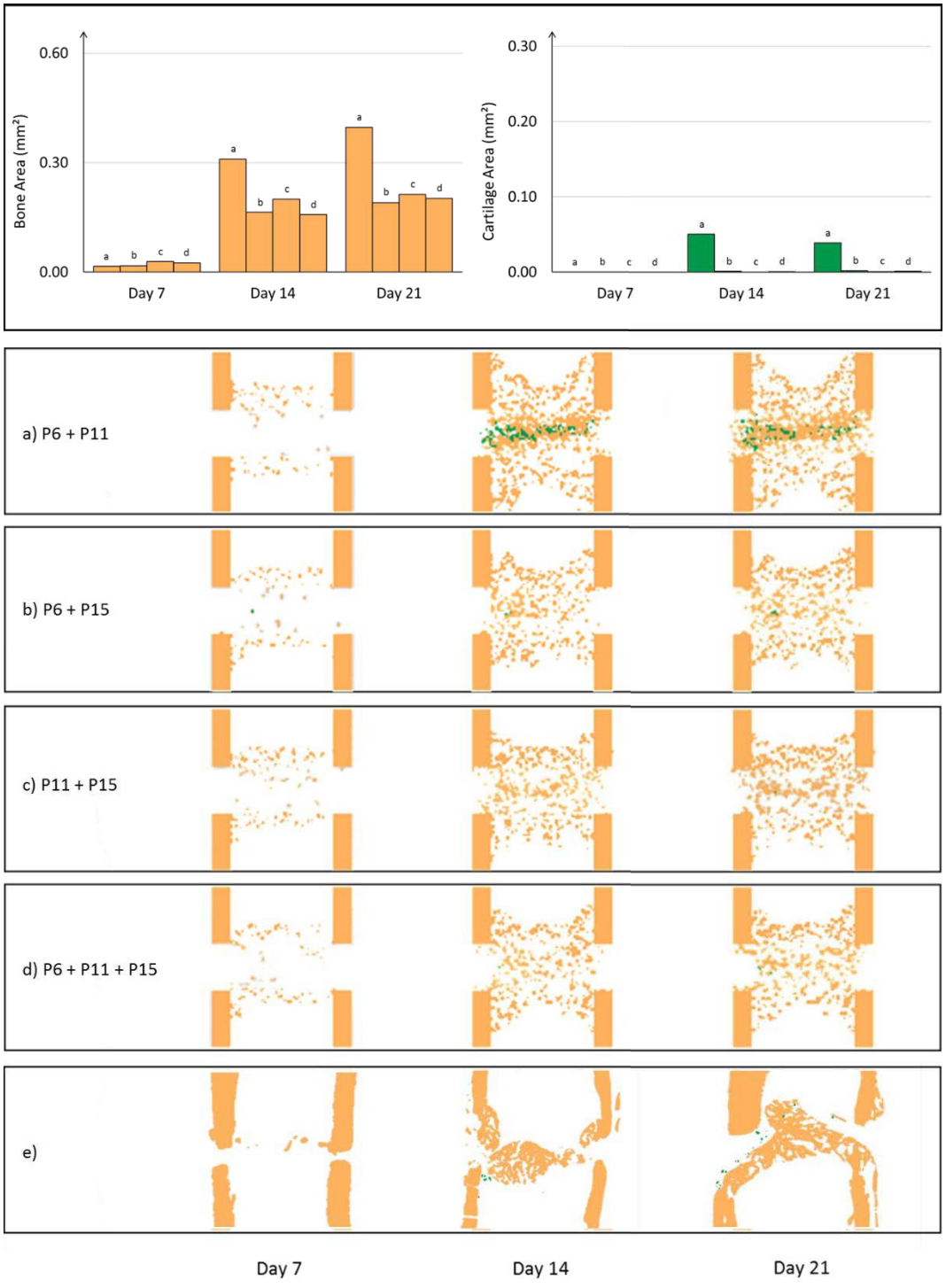

Figure 3.8. – Top: quantitative comparison in bone and cartilage area at 7, 14 and 21 days between the case studies P6+P11 (a), P6+P15 (b), P11+P15 (c), P6+P11+P15 (d) and the histological images of 78-week old mice (e) under rigid external fixation. Bottom: predicted tissue patterning at 7, 14 and 21 days under rigid external fixation. Dark yellow: bone, green: cartilage.

Likewise, under semirigid fixation, the similarity in the tissue patterning and tissue area was observed between the combinations P6+P15, P11+P15 and P6+P11+P15. In particular, for all those case studies bone formation was observed within the osteotomy gap (Figure 3.9.). Incomplete healing was predicted still at 21 days for the case study P6+P11 (Figure 3.9.). From a quantitative point of view, marked difference in cartilage area was observed between P6+P11 and the other case studies at 14 days post-operation (P6+P11: 0.19 mm^2, P6+P15: 0.07 mm^2, P11+P15: 0.06 mm^2, P6+P11+P15: 0.08 mm^2) and 21 days post-operation (P6+P11: 0.30 mm^2, P6+P15: 0.08 mm^2, P11+P15: 0.07 mm^2, P6+P11+P15: 0.05 mm^2) (Figure 3.9.). Moreover, a minor area was occupied by bone tissue within the osteotomy at 14 days post-operation for P6+P11 (0.13 mm^2) compared to the other cases (P6+P15: 0.42 mm^2, P11+P15: 0.50 mm^2, P6+P11+P15: 0.41 mm^2) (Figure 3.9.).

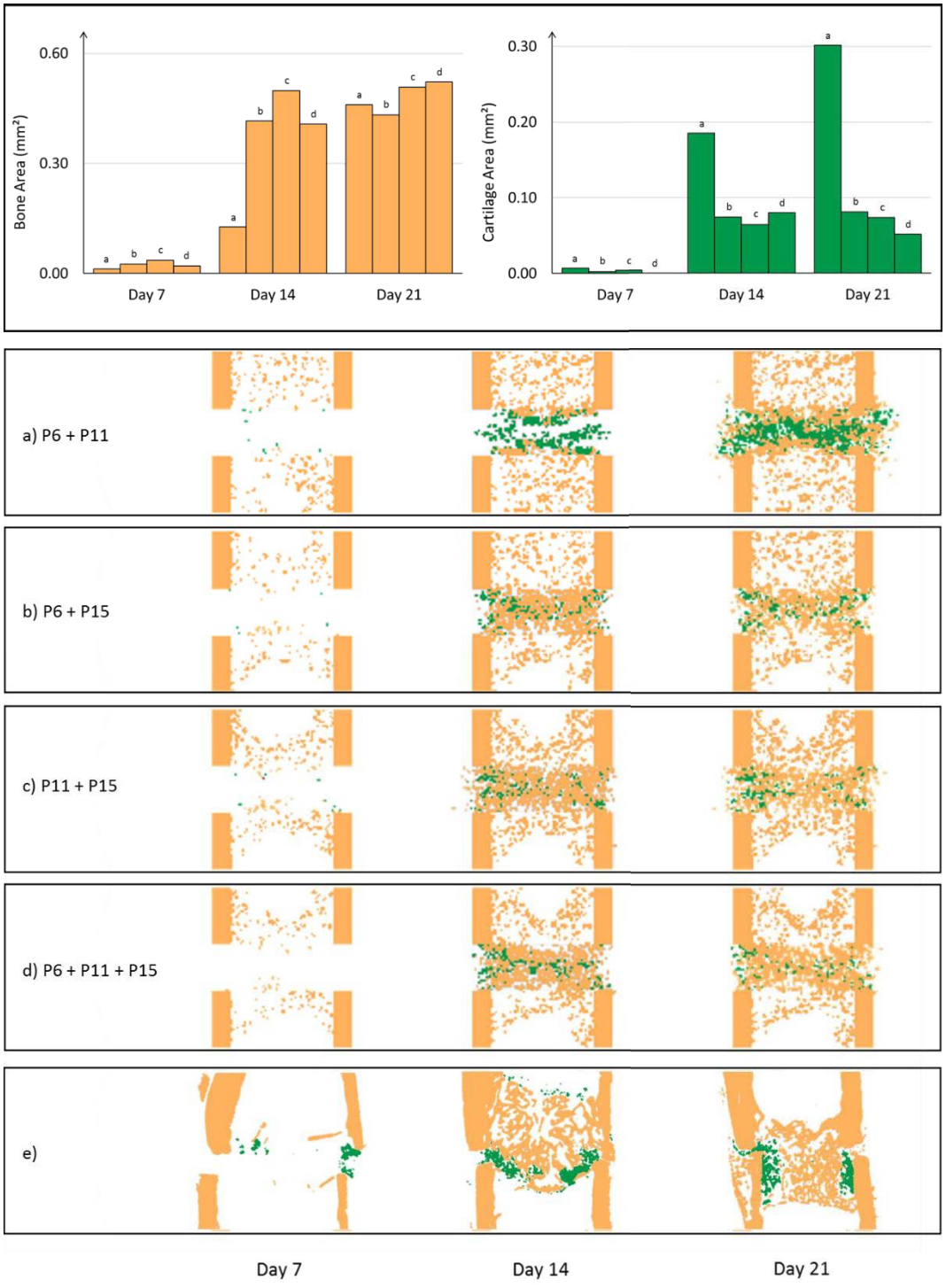

Figure 3.9. – Top: quantitative comparison in bone and cartilage area at 7, 14 and 21 days between the case studies P6+P11 (a), P6+P15 (b), P11+P15 (c), P6+P11+P15 (d) and the histological images of 78-week old mice (e) under semirigid external fixation. Bottom: predicted tissue patterning at 7, 14 and 21 days under semirigid external fixation. Dark yellow: bone, green: cartilage.

From a quantitative point of view, the parameter P15 was the one that influenced the most bone and cartilage formation when it was set to the "elderly" level. In fact, differences in tissue area were observed between the case studies that include its alteration (P6+P15, P11+P15, P6+P11+P15) and the one that did not (P6+P11) under both rigid (Figure 3.8.) and semirigid fixation (Figure 3.9.). This result highlights the age-related reduction of cellular mechanoresponse as a key contributor to age-related alterations in bone healing. Moreover, the comparison with histological images of 78-week old mice showed better agreement with tissue patterning predicted from the case studies where age-alteration of P15 was included. For example, a preponderant cartilage formation at 21 days within the gap was predicted in mouse under semirigid fixation for the case study P6+P11. The alteration of mechano-regulation (P15) was more and more highlighted as a possible explanation of the compromised healing condition in elderly mice, as its inclusion was necessary to correctly reproduce age-altered healing, as observed experimentally (Figure 3.9.). In the following paragraph, experimental data from elderly mice are compared with computer model predictions of healing with reduced cellular mechanoresponse (i.e. the parameter P15 is the only one set to the "elderly" level).

3.1.5. Comparison with experimental results

The comparison between the proposed aged mice *in silico* model and the 78-week old mice histology under rigid fixator conditions showed that bone area predicted by the elderly mouse computer model matched histomorphometry data at 7 days (*in vivo*: 0.01 mm^2, *in silico*: 0.02 mm^2) and was underestimated at 14 (*in vivo*: 0.29 mm^2, *in silico*: 0.19 mm^2) and 21 days (*in vivo*: 0.34 mm^2, *in silico*: 0.21 mm^2) (Figure 3.10.). Predicted cartilage area was almost negligible (< 0.03 mm^2) at all time-points, in agreement with experimental results (Figure 3.10.).

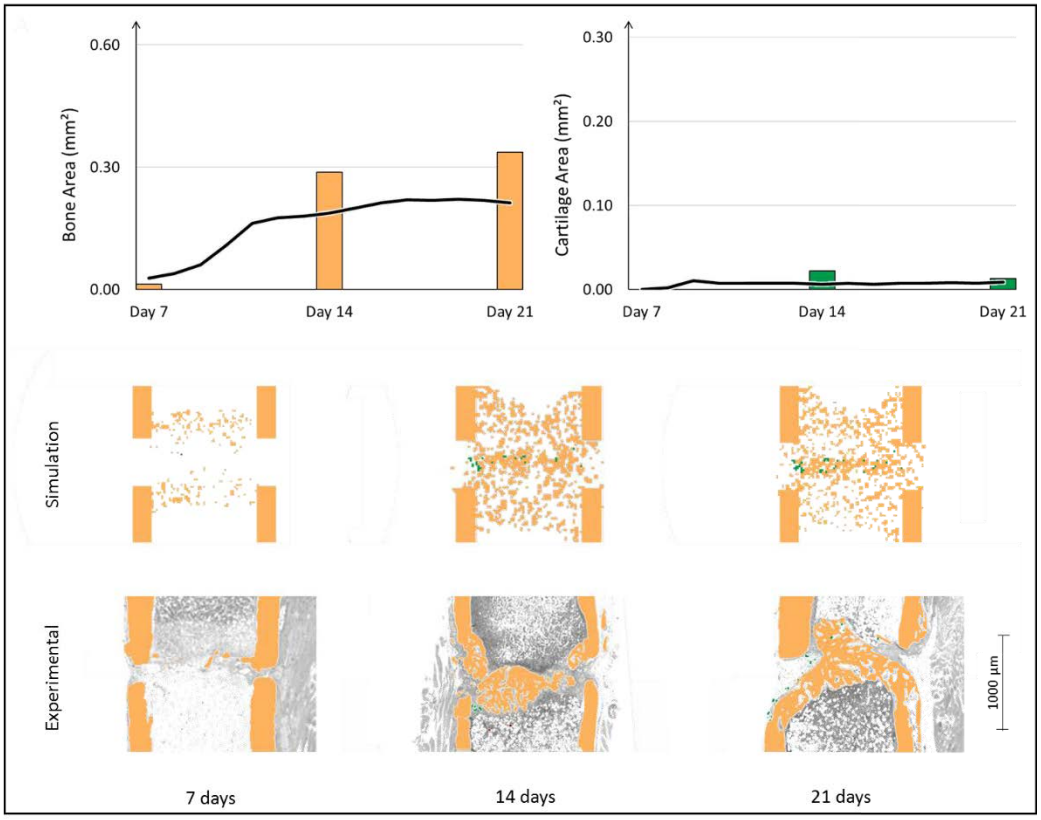

Figure 3.10. – Quantitative (top) and qualitative (bottom) comparison of bone and cartilage area between predicted (black line) and experimental (bars) results of bone healing in elderly mice under rigid fixation. In silico *results correspond to a model with reduced cellular mechanoresponse (P15).* In silico *results are daily sampled with continuity between day 7 and day 21,* in vivo *results are reported at 7, 14 and 21 days.*

Under semirigid conditions, the predicted peak cartilage area occurred at day 11 (0.12 mm^2). The comparison with *in vivo* data at day 14 (0.18 mm^2) suggested that the computer model predicted this event in advance (Figure 3.11.). Moreover, the comparison between the bone tissue area predicted at day 11 (0.29 mm^2) and at day 14 (0.47 mm^2) suggested that anticipated bone formation could explain the difference with *in vivo* measured tissue area at day 14 (0.14 mm^2) (Figure 3.11.).

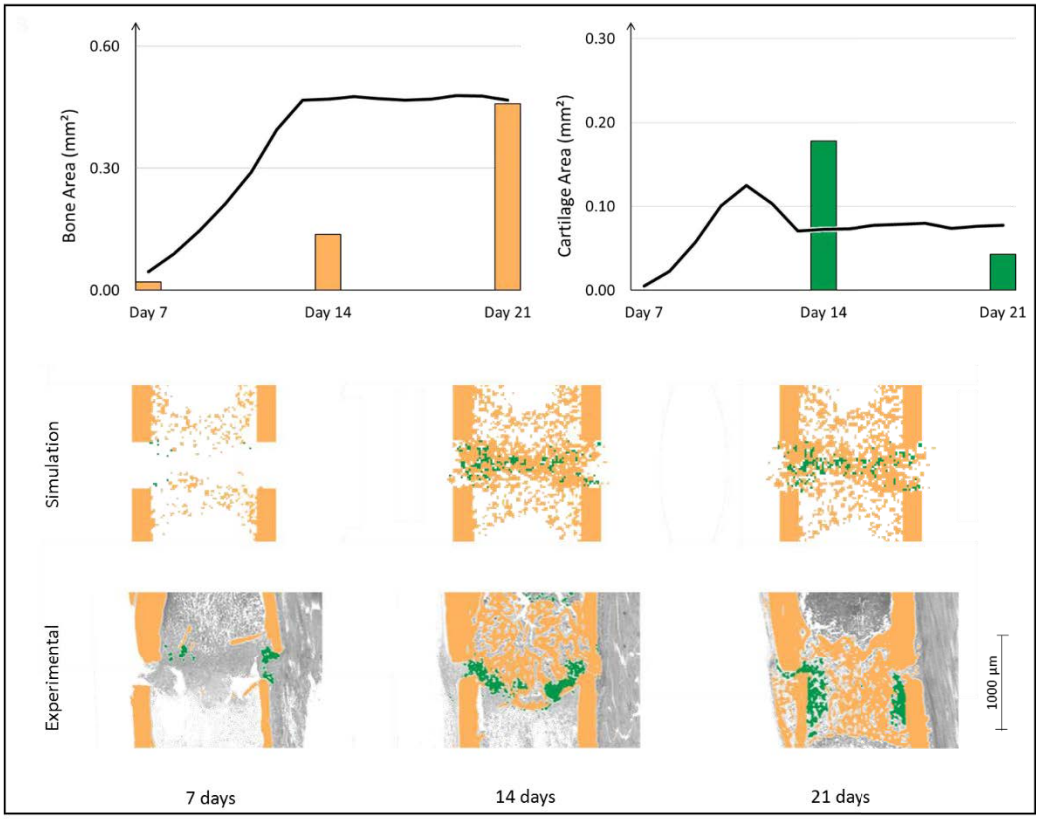

Figure 3.11. – Quantitative (top) and qualitative (bottom) comparison of bone and cartilage area between predicted (black line) and experimental (bars) results of bone healing in elderly mice under semirigid fixation. In silico *results correspond to a model with reduced cellular mechanoresponse (P15).* In silico *results are daily sampled with continuity between day 7 and day 21,* in vivo *results are reported at 7, 14 and 21 days.*

3.1.6. Discussion

Aging is known to alter the bone regeneration potential [25] [26]. In particular, different studies have shown alterations in the number and biological behavior of donor cells with aging [29]-[32] [34]. At the tissue level, aging resulted in a lack of response to changes in fixation stability. In fact, while the use of a semirigid external fixator was observed to compromise bone regeneration in adult mice [86], the healing outcome was observed to be less dependent on the osteotomy stabilization in elderly mice [38]. Here, a computer model was developed to investigate the distribution of local mechanical stimuli within the healing region, which is challenging to measure *in vivo*, and to investigate how age-alterations at the cellular level contribute to the bone healing process.

The stimulation pattern predicted within the callus in the initial phase of healing resembled the mechanical environment already observed in other computer osteotomy models, where higher mechanical strains are predicted in the intercortical compared with the periosteal region [22] [24] [56]. The comparison with a rat osteotomy model [61] showed that tissues within the mouse callus region are subject to higher mechanical stimuli.

A mechanobiological computer model able to explain bone healing in rats [61] was adapted to investigate bone healing in mice. It was observed that due to the high levels of mechanical strain post-surgery, the model was not able to predict regeneration as observed *in vivo* and, instead, a non-union was predicted. Previous studies also investigated inter-species differences in the mechanical regulation of healing, showing that different specifies respond to different ranges of mechanical stimuli [61] [71]. In Checa et al. (2011), sheep were suggested to respond to higher levels of mechanical stimuli than rats [61]. In contrast, Wehner et al. (2014) adapted a mechano-regulation algorithm validated for sheep [58] to respond to higher strains in rats [71]. In the present study, despite anatomical similarities between mouse and rat, a strong difference in the mechanical regulation of bone healing was identified.

A new mechano-regulatory rule was proposed to investigate tissue differentiation in mice, where tissue differentiation occurred under higher levels of mechanical stimuli. The new rule correctly predicted complete regeneration in a mouse femoral osteotomy under rigid fixation, avoiding interfragmentary fibrous tissue formation as predicted when rat mechano-regulatory rules were used. The rat mechano-regulatory rule, in fact, drove the differentiation into fibroblasts when high mechanical stimuli were sensed by MSCs in the mouse osteotomy model. This condition resulted in the invasion of fibrous tissue within the healing region. In analogy, the rat mechano-regulatory rule generated sharper mismatch between computer simulations and experimental images in the mouse model with semirigid external fixator, which was characterized by even larger interfragmentary mechanical stimuli. Delayed healing due to higher mechanical stimulation was already observed in other *in silico* studies that investigated the mechanical environment within the osteotomy opening under different fixator stiffness [104] [105]. The new rule, adapted to respond to higher mechanical stimuli, was then used to regulate MSC differentiation in the mouse model.

The mouse bone healing model was thereafter used as a baseline model to investigate how aging alters the mechanobiological regulation of healing. Age-related compromised cellular behavior was simulated *in silico* to investigate the effects of aging on bone regeneration. To investigate the relative role of the multiple cellular processes on bone regeneration, a DOE approach was used [99]. The DOE method allowed a multi-parametric investigation of the effect that multiple factors might have on the healing outcome. For each fixation condition (rigid and semirigid), sixteen different simulations were run to investigate the effect of fifteen parameters on two levels (adult and elderly). The elderly level of each parameter was directly obtained from the adult one by halving or doubling the ratio of the specific cellular activity, for example doubling the rate of cellular apoptosis. The two-fold factor was arbitrarily chosen with the aim to identify the relative role of each parameter on the regeneration process. Kasper et al. (2009) observed,

in vitro, a 40% reduction of migrating MSCs when the cells were collected from an old donor instead of a young one [28]. Stenderup et al. (2003) reported a 42% shorter lifespan and 44% reduced proliferation capacity of old versus young donors' MSCs [106].

Reduced mechanoresponse, simulated as a need for higher mechanical stimulation to regulate the differentiation of MSCs, was identified as the most relatable factor to explain differences in the bone healing response to changes in fixation stability between adult and elderly mice. In mice, semirigid fixation led to delayed healing in adult mice and successful healing in the elderly. The *in silico* model correctly predicted successful bone healing within 21 days under semirigid conditions only when mechano-regulation was altered. Interestingly, other parameters such as fibroblast apoptosis and MSC proliferation also showed a strong effect on bone healing progression; however, they were not able to fully explain the experimental data. Isaksson et al. (2008) also used DOE approaches to investigate the influence of model parameters on bone healing predictions. They found that the most influencing parameters at cellular level are the ones that regulate tissue production and degradation [100]; however, they did not do any comparison to experimental data.

To reduce the computational complexity, the comparison between the sixteen simulations and the baseline model was only based on the bone tissue area. Other outcomes of the *in silico* model could also have been taken into consideration to investigate additional alterations observed in elderly mice bone healing, such as callus size [37] [38] and cartilage area [38]. Although the computer model under this age-related reduction of mechanoresponse led to good agreement with experimental data in elderly mice, other mechanisms might also play a role. The role of cellular mechanoresponse alteration on additional biological parameters (e.g. callus size and tissue distribution) needs to be further investigated in the future.

Under rigid fixation, a good agreement in bone and cartilage tissue areas was found between simulation and histology images in elderly mice. Under

semirigid fixation, bone healing was predicted to happen faster *in silico* than in elderly mice, when mechanoresponse was reduced to simulate aging. The excessive formation of bone tissue predicted under semirigid conditions, which was also observed in adult mice, resulted in larger bone area predicted at day 14 post-operation, compared with *in vivo*. This phenomenon could be explained by anticipated endochondral ossification *in silico*, which resulted in reduced cartilage at 14 days post-operation. The early bone formation could be explained by the reduced capacity of the current mouse osteotomy model to fully replicate bone and cartilage remodeling under higher mechanical stimulation as it results in anticipated remodeling phase when semirigid stabilization is provided. Several computer models have previously investigated bone remodeling during the bone healing process using *in silico* approaches [107] [108]. They have shown a strong influence of the type and magnitude of external mechanical stimuli on the regulation of the remodeling response.

Under semirigid conditions, the bone area predicted *in silico* matched with experiments at 21 day post-operation. A deeper analysis of the phenomenon was performed by plotting bone area daily to observe bone and cartilage tissue area dynamics through the healing process. The maximal bone tissue area, observed only after 21 days *in vivo* in elderly mice, was already predicted *in silico* at 13 days (Figure 3.11.). From that time-point on, the area followed a steady-state dynamics until the end of the simulation. Anticipated cartilage area dynamics under semirigid fixation was also experienced *in silico*: it was predicted to peak around 11 days in the age-related reduced mechanoresponse model and maintain a steady-state dynamic from day 14 onwards, after a slight reduction (Figure 3.11.). *In vivo* histomorphometry showed maximal cartilage area at 14 days under semirigid conditions. The predicted anticipated cartilage formation could be due to the absence of oxygen tension parameter in the current model, which considered the whole callus fully oxygenated. As adult mice cartilage area predictions correctly matched experimental results under semirigid conditions, age-related

reduced callus vascularization under higher interfragmentary strains could explain why *in vivo* results showed cartilage where the computer model predicted bone formation under high mechanical stimulation. Aging was already observed to reduce vascularization of the fracture gap during healing [33]. The potential compromising effect of impaired angiogenesis should be further investigated in future models. In analogy with the outcomes of the presented model, other computer models also predicted faster bone healing than observed from experiments [109] [110]. Moreover, the strong variability in the mechano-regulation of bone healing between animals within the same experiment is a limitation that should also be considered in the future *in silico* studies [111].

In the mice osteotomy model, the amount of predicted bone tissue formed within the gap was considerably higher than the one observed experimentally. Although bone remodeling was incorporated in the model according to Lacroix and Prendergast (2002) [95], the model did not accurately capture the remodeling phase of bone healing. This limitation led to excessive formation of bone between days 14 and 21 under semirigid conditions. The mechanical regulation of the remodeling stage of bone healing in mice should be further investigated in the future. In fact, the proposed mechano-regulatory rule was based on the distribution of the mechanical stimuli predicted in the initial stages of healing, when granulation tissue characterized the callus domain. Isaksson et al. (2008) have previously investigated the bone remodeling phase during bone healing using computer models but the mechano-regulated remodeling theory was not able to replicate some aspects of the healing in the late stages [112]. It has to be taken into consideration that the remodeling phase occurs when the hard callus is formed in the later stages, when the mechanical environment within the callus region is characterized by lower magnitude stimuli [62]. For this reason, in future models the rule should be adapted to consider the variability of the tissue patterning within the healing region.

In summary, the *in silico* model of bone healing in mouse was used to investigate the effect of aging on bone healing at the cellular and tissue levels. In this study, age-related alterations were simulated at the cellular level to investigate the age-related alterations of the mechanical regulation of bone healing observed at tissue level. *In vivo*, as fixation stability was observed to play a lower role in the regulation of healing in elderly than adult mice, it was hypothesized that alteration of the mechanical regulation of cellular behavior might explain the outcomes of the experiments. To our knowledge, this is the first study that investigates age-related alterations in cellular mechanoresponse during bone healing. The role of aging on the mechano-regulation of bone formation and resorption have been extensively investigated in the context of bone adaptation [39] [41] [113]. Razi et al. (2015) showed a dysregulation in the bone remodeling response to mechanical loading with age, although it did not identify any changes in the mechanical thresholds required to initiate formation or resorption [41]. However, the effect of aging is not limited to the remodeling phase but involves the mechano-regulation of all the tissue patterning dynamics. The presented model investigated the bone healing process since the initial stages. The extensive investigation of all the mechanisms that alter mechano-regulation at different scales makes this work the only one that investigated aging effect on bone healing at cellular level. The capacity of bone to heal in elderly mice also under compromised mechanical conditions (semirigid fixation) highlighted the role of mechanics on the healing outcome. Despite the altered biological activities at cellular level in elderly mice, the age-related altered mechano-regulation contrasted the effect of semirigid fixation conditions. The selection of a correct mechanical stimulation is then more important in adult patients, whose cells are more sensitive to the mechanical environment than in the elderly.

3.2. Mechanobiological regulation of BMP-2 stimulated bone healing

3.2.1. Reduced intracortical strains in critical size defects compared with small osteotomies

Predicted mechanical strains within the critical size defect (5 mm) in rat were considerably lower than in the small osteotomy gap (1 mm). Predicted compressive strains were up to 40% lower in the large defect compared with the small gap size (Figure 3.12.). The maximal difference was observed within the intercortical region. In detail, the large gap was characterized by an average compressive strain reduction of 38.2% in the lateral intercortical region (side of the external fixator) (large gap: 0.042±0.002; small gap: 0.068±0.010). In the medial intercortical region, the difference was of 32.0% (large gap: 0.053±0.002; small gap: 0.078±0.009). The large defect was also characterized by averagely 23.7% lower compressive strains in the lateral periosteal side of the callus (large gap: 0.029±0.003; small gap: 0.038±0.005). Minor alterations in mechanical strains were observed in the endosteal region (large gap: 0.045±0.003; small gap: 0.049±0.009) and in the medial periosteal side of the callus (large gap: 0.044±0.004; small gap: 0.048±0.009).

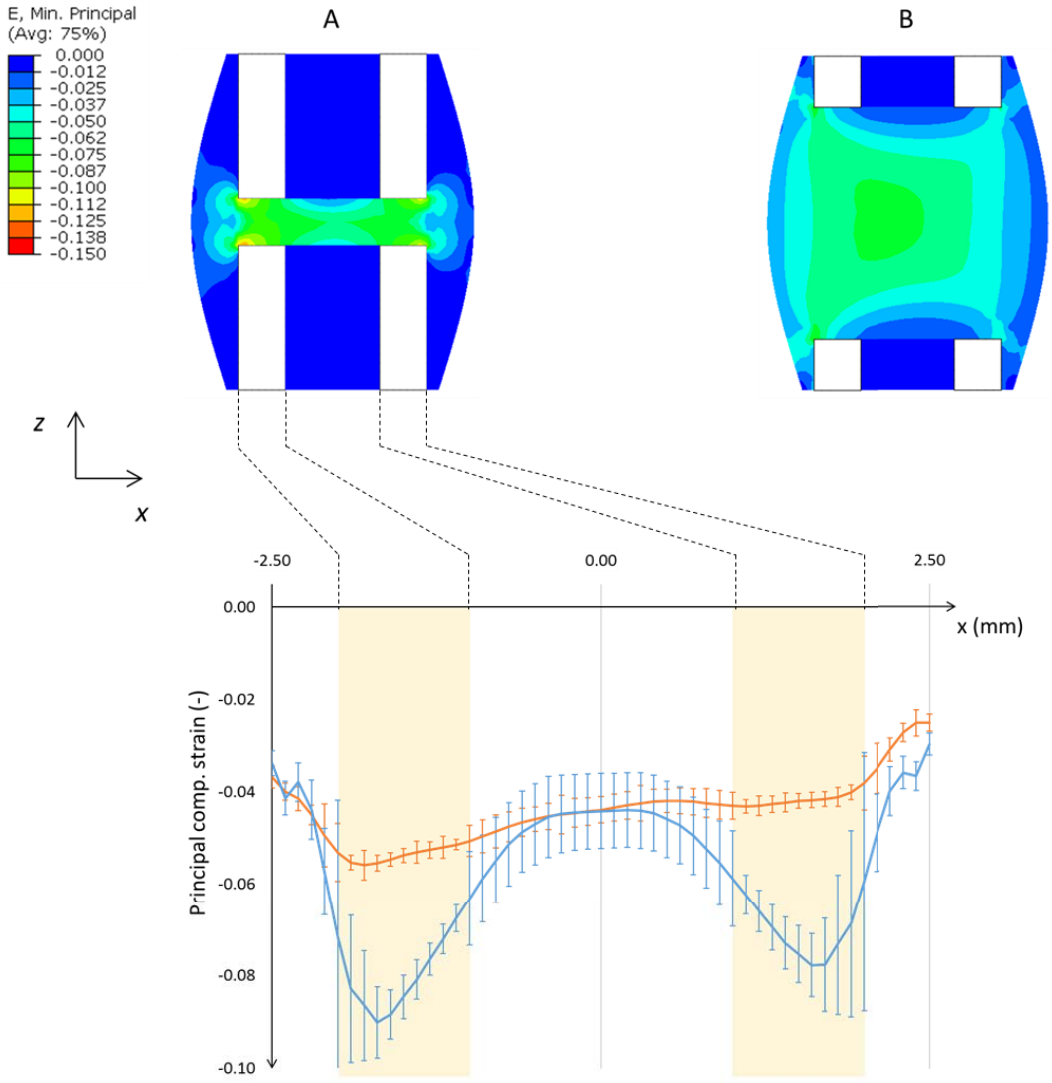

Figure 3.12. – Top: distribution of principal compressive strain within the osteotomy gap in a small (1 mm, A) and a large defect (5 mm, B). Bottom: quantitative interfragmentry strain magnitude average and standard deviation predicted within the osteotomy region along the z axis for small gap (blue line) and large defect (orange line).

3.2.2. Mechanical environment within the large defect led to bone marrow encapsulation

The mechano-regulated simulation of untreated bone defect healing resulted in incomplete defect healing still after 6 weeks post-operation. The model predicted endosteal and periosteal bone formation in the first weeks of healing (Figure 3.13.). The newly formed bone shaped a bony cap that encapsulated the medullary cavity, as observed at 4 weeks post-operation (Figure 3.13.). Bone formation continued, as observed from the predicted progression, but still no connection between the two defect extremities was experienced at week 6 (Figure 3.13.). Also *in vivo*, critical defect showed non-union when healing happened without BMP-2 treatment [45] (Figure 3.13.). The computer model correctly predicted the bone encapsulation of the medullary cavity, but bone tissue formation prediction was overestimated when compared with experiments [45] (Figure 3.13.).

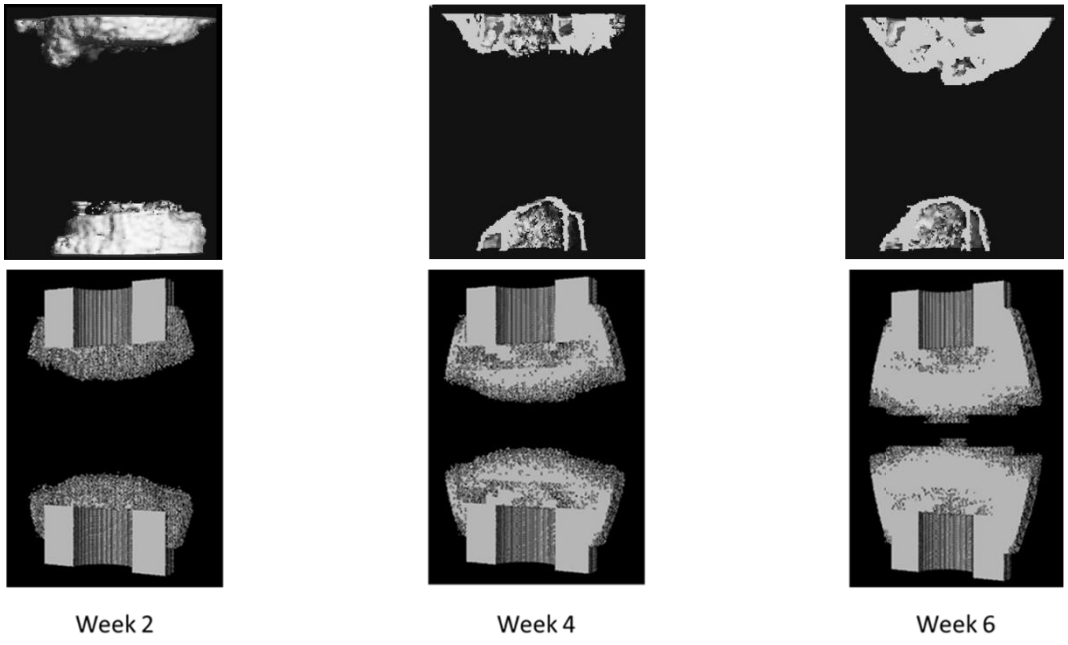

Figure 3.13. – µCT images (top) and predicted bone spatial distribution (bottom) at 2, 4 and 6 weeks post-operation under control *case conditions.*

3.2.3. Delayed healing occurs in large bone defect also under additional mechanical stimulation

In silico, weekly external mechanical stimulation showed no enhancement of bone healing under critical defect conditions. The weekly provision of external mechanical loading did not considerably alter tissue patterning when compared with the *control* case and incomplete healing was still predicted at 6 weeks post-operation. The dynamics of bone tissue evolution within the defect did not differ from the *control* case one: endosteal bone formation was predicted and incomplete healing due to marrow encapsulation was observed at 6 weeks post-operation (Figure 3.14.). Incomplete healing was observed also from μCT images when only mechanical stimulation was provided to stimulate healing in critical defect [45] (Figure 3.14.). Incomplete healing due to medullary closure was predicted also *in silico* with overestimation of bone tissue formation in comparison with experimental data [45] (Figure 3.14.).

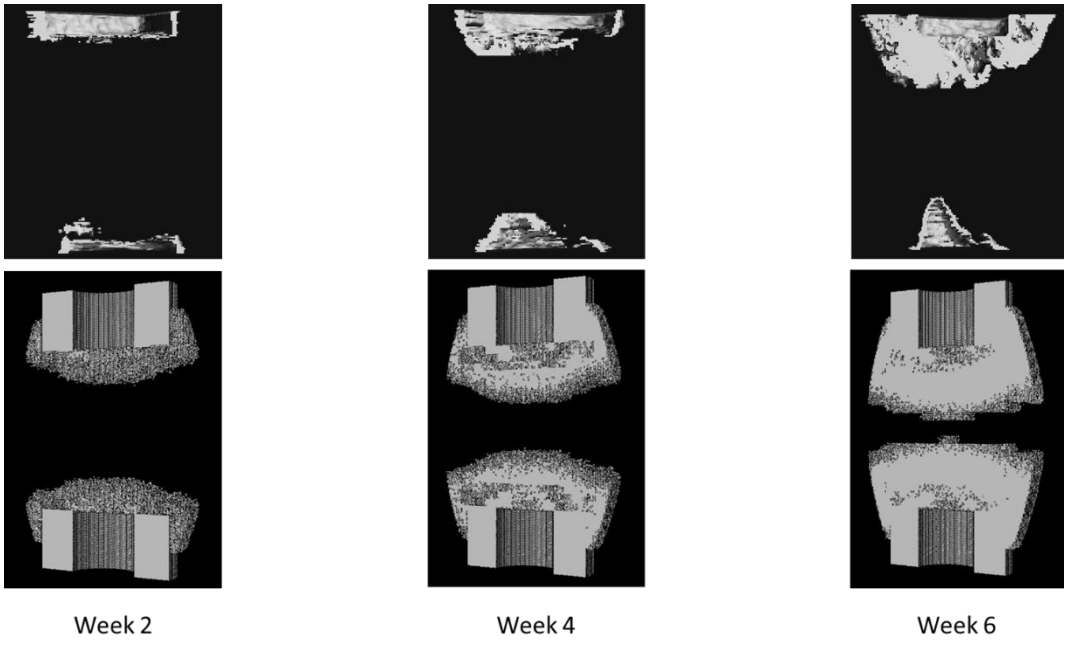

Figure 3.14. – μCT images (top) and predicted bone spatial distribution (bottom) at 2, 4 and 6 weeks post-operation under only load *case conditions.*

Differences between predicted bone tissue volume in *control* and *only load* cases were negligible at 2 weeks (*control*: 18.85 mm^3, *only load*: 18.77 mm^3), 4 weeks (*control*: 63.40 mm^3, *only load*: 63.39 mm^3) and 6 weeks (*control*: 98.27 mm^3, *only load*: 98.47 mm^3) post-operation (Figure 3.15.). Quantitative comparison of predicted bone tissue volume and µCT data [45] highlighted the model tendency to overestimate bone tissue formation within the defect through the healing process (Figure 3.15.).

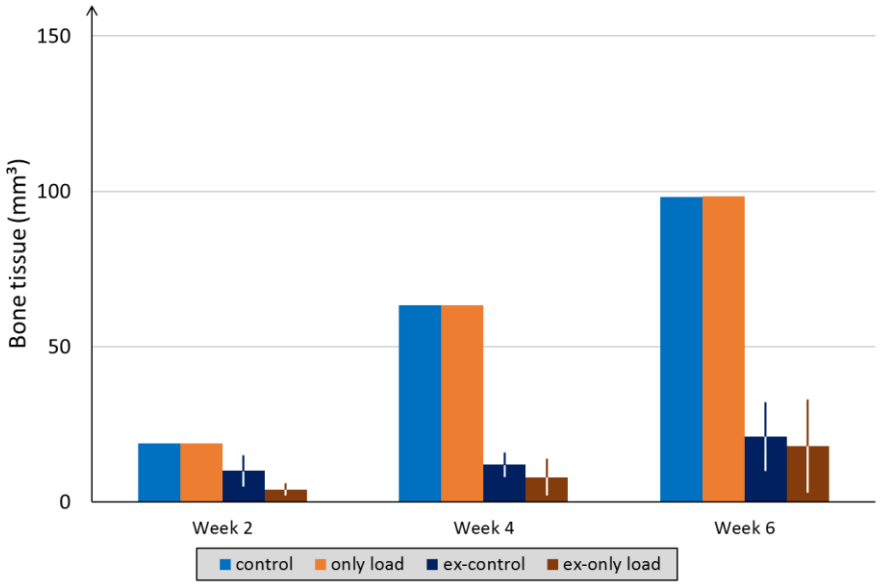

Figure 3.15. – Quantitative comparison of bone tissue volume between computer model and experimental data (average±SD) [45] at 2, 4 and 6 weeks post-operation for control *and* only load *case studies. Note: ex- prefix in legend identifies experimental data set.*

3.2.4. The concentration levels of BMP-2 within the healing region highly depend on the release kinematics

The simulation of collagen-sponge driven gradual release of BMP-2 showed the importance of a gradual release to avoid fast reduction of BMP-2 to physiological levels. The analysis of BMP-2 dynamics through the time, in fact, showed a substantial difference between gradual and immediate release models. With gradual release, the BMP-2 concentration dynamics was mostly regulated by its diffusion from the release zone (Figure 3.16.). Under gradual release, BMP-2 enhanced MSC proliferation and bone tissue formation capacities within the defect until week 2 post-operation. At this time-point, the maximal concentration within the defect reached 380 ng mL^{-1} (Figure 3.16.). At week 4 post-operation, the effect of the residual BMP-2 within the callus (maximum concentration = 13 ng mL^{-1}) was negligible for the enhancement of MSC proliferation and had a reduced effect on promoting bone tissue production (Figure 3.16.). BMP-2 effect on cellular chemotaxis followed a different trend. Its attractive effect on MSCs and osteoblasts was maximum in the periosteal side of the callus, where the BMP-2 concentration was approximately 1 ng mL^{-1} (*§ 2.3.3.*). The maximum effect was localized in the periosteal area until week 4 and it extended to the center of the defect at week 6 (Figure 3.16.). Cellular chemotaxis was the only BMP-2 effect that still played a role at the cellular level after 6 weeks post-operation, when a maximal concentration of 0.45 ng mL^{-1} was still predicted within the defect gap (Figure 3.16.). BMP-2 did not play a role in MSC proliferation and bone tissue production enhancement anymore within the callus at this time-point (Figure 3.16.).

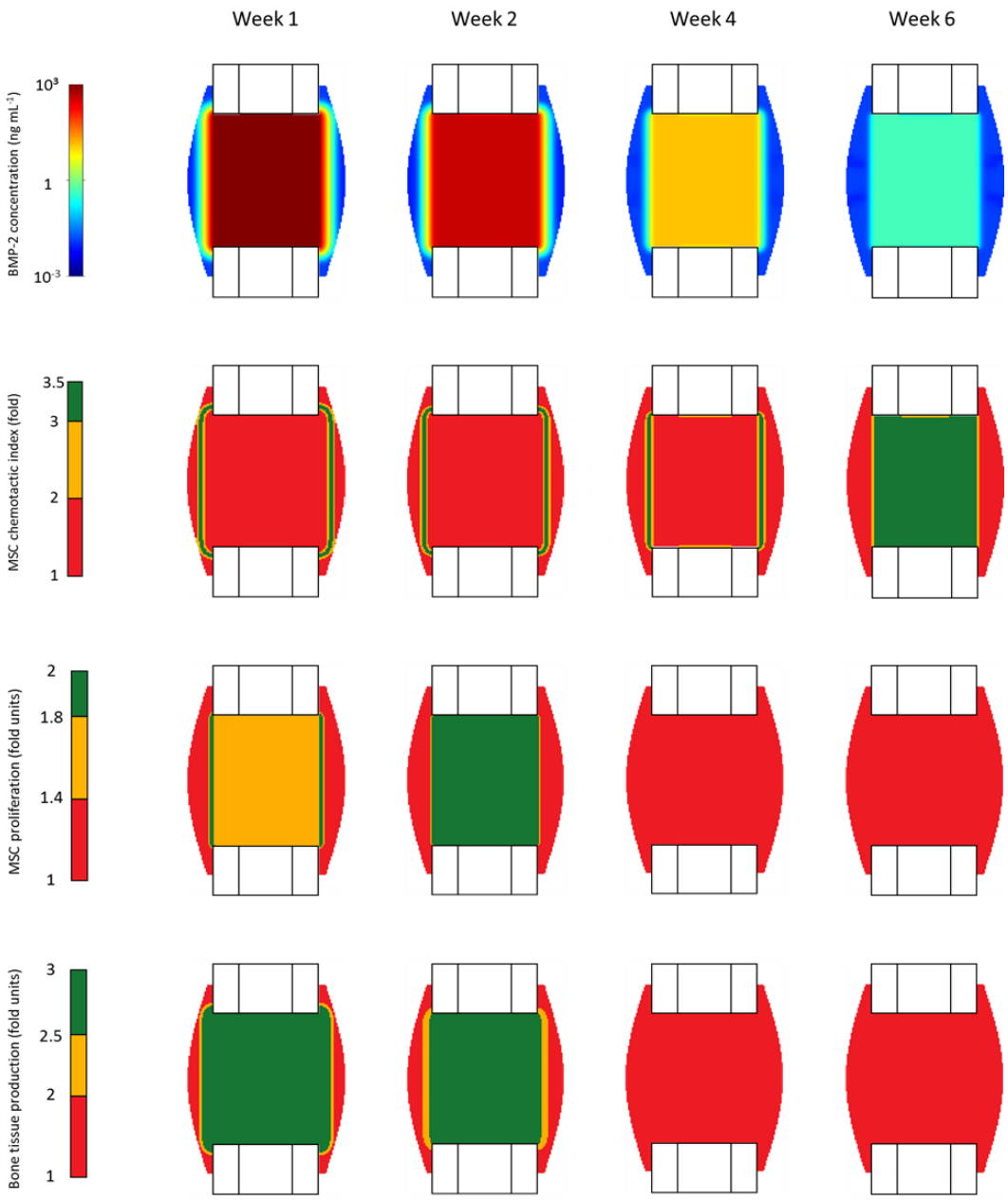

Figure 3.16. – BMP-2 concentration dynamics and its effect on the enhancement of cellular processes to promote bone healing under BMP-2 gradual release. Data were sampled at 1, 2, 4 and 6 weeks post-operation.

A different scenario was predicted when the instantaneous release was implemented in the model. Fast BMP-2 degradation was predicted from the initial iterations and BMP-2 reached a physiological concentration in 10 days (Figure 3.17.). This quick drop of BMP-2 concentration led to a cessation of the influence of BMP-2 on cellular activity already after 7 days (Figure 3.17.). Periosteal chemotaxis effect on MSCs was still observed when immediate release of BMP-2 was simulated, but its effect was limited to the first week post-operation (Figure 3.17.). MSC proliferation enhancement was favored in the periosteum at day 3 and moved to the defect gap at day 5 (Figure 3.17.). From that time-point on, the effect was negligible. Likewise, BMP-2 driven bone tissue production enhancement was maximum within the callus until day 5 and no effect was anymore predicted from day 7 on.

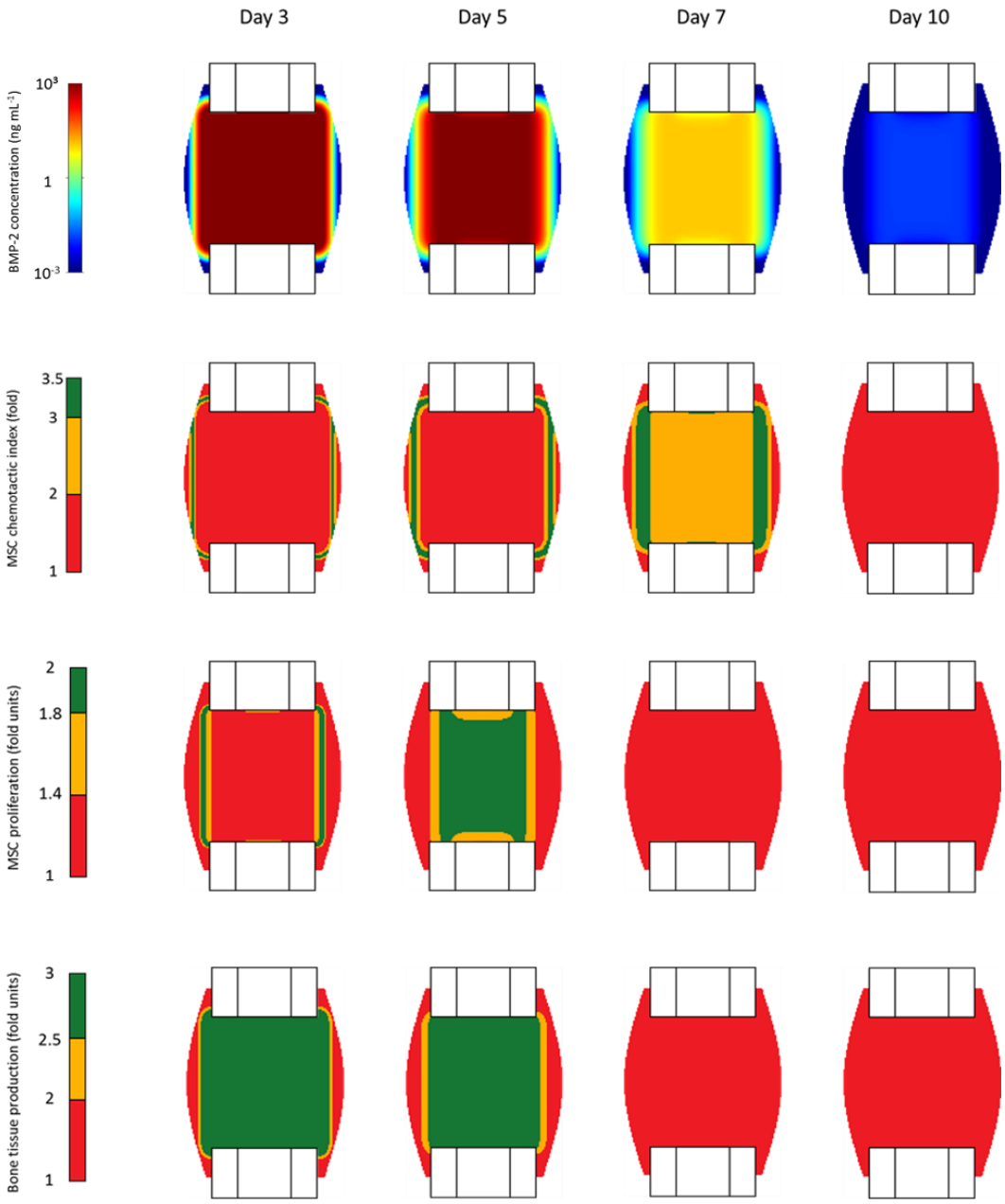

Figure 3.17. – BMP-2 concentration dynamics and its effect on the enhancement of cellular processes to promote bone healing when BMP-2 was instantaneously released. Data were sampled at 3, 5, 7 and 10 days post-operation.

3.2.5. BMP-2 chemotaxis can explain large bone defect bridging 2 weeks post-surgery

BMP-2 treatment had a central role in guaranteeing successful healing of large bone defects in rats, *in silico*. When BMP-2 effect was implemented in the model, bone bridging was predicted already after 2 weeks (Figure 3.18.). Bone tissue formed mostly in the periosteal region of the callus domain and connected the two cortex extremities of the defect. Scarce bone formation was instead observed endosteally at 2 weeks (Figure 3.18.). Tissue distribution was characterized by bone in the periosteal side of the callus. Preferential bone formation through periosteal bridging was observed also from μCT images collected at 2 week post-operation [45] (Figure 3.18.). The bony bridging which connected the defect extremities thickened week after week through the entire simulation. This resulted in a rigid callus shell at week 4, which further stabilized the defect. At the same time-point, bone deposition within the defect cavity was also observed (Figure 3.18.). A small preference of bone deposition within the medial intracortical region was predicted and a second cortex was almost completed at week 4, as observed also *in vivo* (Figure 3.18.). At week 6, almost the whole callus domain was filled with bone (Figure 3.18.). An overestimation of bone tissue formation was predicted after 6 weeks. *In vivo*, bone tissue did not completely invade the osteotomy gap, but preferentially formed bone intercortically and cancellous bone in the newly reunited medullary cavity 172 (Figure 3.18.). *In silico*, considerably high amounts of bone tissue were also predicted endosteally.

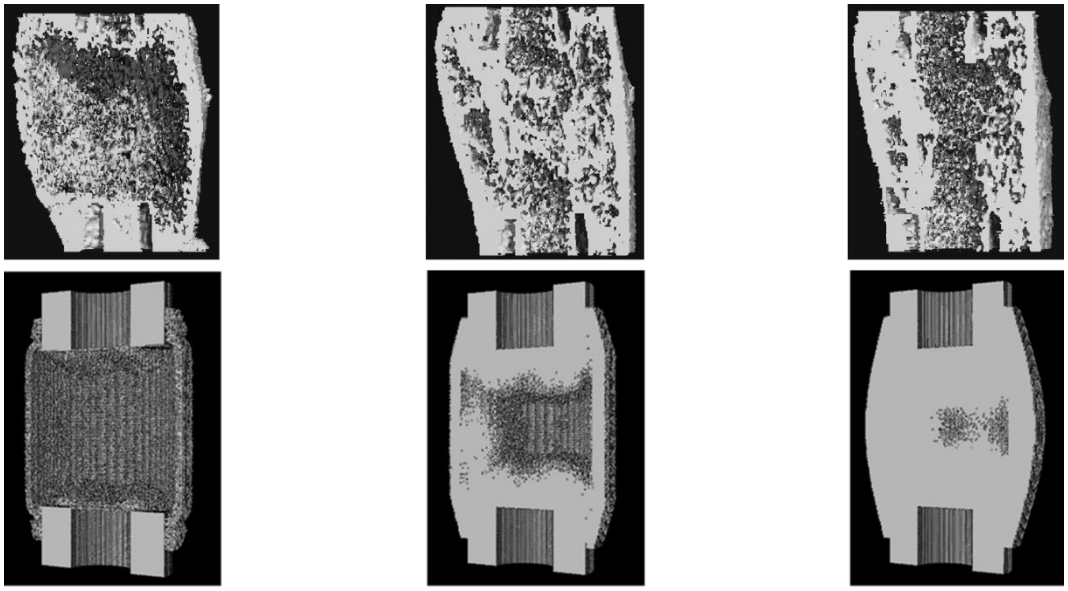

Figure 3.18. – µCT images (top) and predicted bone spatial distribution (bottom) at 2, 4 and 6 weeks post-operation under only BMP-2 *case conditions.*

3.2.6. Mechanical stimulation of BMP-2 release can explain enhanced bone formation in mechanically loaded BMP-2 bone defect healing

In silico, external mechanical stimulation did not support additional bone tissue formation in BMP-2 treated defect healing. From a qualitative point of view, bone tissue distribution through the healing process followed analogous patterns to the one predicted with BMP-2 treatment alone. Bone bridging through the periosteal region of the callus was observed to form during the first 2 weeks of healing also in this case (Figure 3.19.). Thickening of the bone bridging at 4 and 6 weeks followed analogous patterning to that observed for the *only BMP-2* case study (Figure 3.19.). Also experimentally, the contribution of additional mechanical stimulation showed minor differences in defect healing dynamics under BMP-2 treatment [45]. Bone healing happened through initial periosteal bridging followed by intracortical bone consolidation, which led to complete defect healing within 6 weeks (Figure 3.19.).

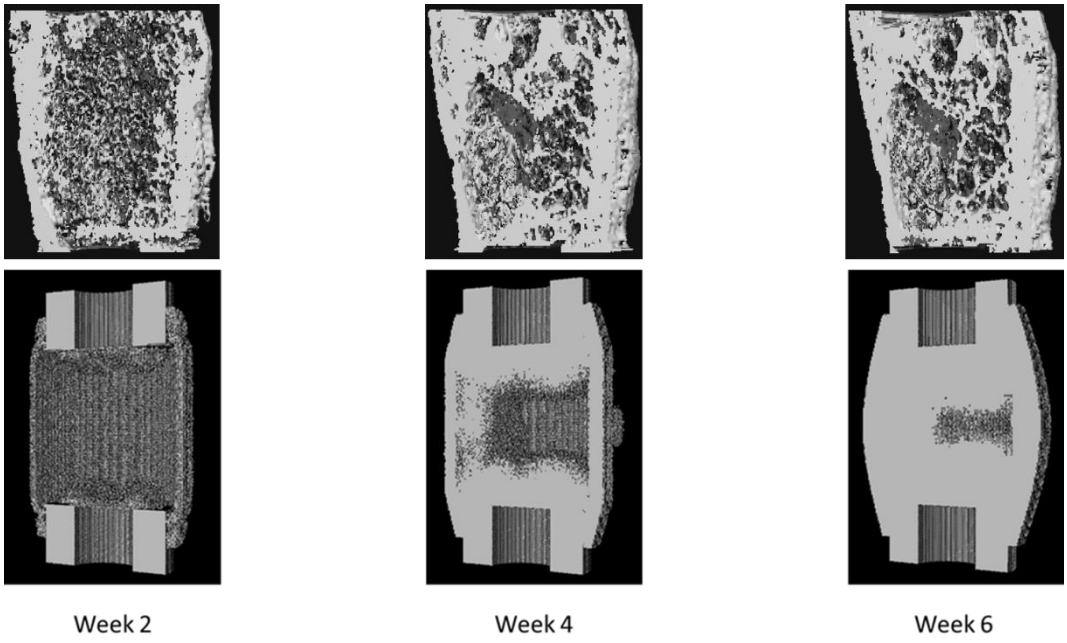

Figure 3.19. – µCT images (top) and predicted bone spatial distribution (bottom) at 2, 4 and 6 weeks post-operation under BMP-2 + load *case conditions.*

Minimal differences in newly formed bone tissue volume under additional mechanical stimulation were predicted within the defect. From a quantitative point of view, bone tissue formation under BMP-2 treatment was predicted to increase week after week independently of whether additional mechanical stimulation was provided or not (Figure 3.20.). This resulted in a negligible difference in bone volume predicted when BMP-2 treatment was supported by additional external loading at 2 weeks (-0.16 mm^3), 4 weeks (-0.24 mm^3) and 6 weeks (-0.24 mm^3) post-operation. *In vivo* data from BMP-2 treated rat large defects [45] showed that the computer model underestimated bone tissue volume at 2 weeks post-operation (*in silico*: *only BMP-2*: 26.79 mm^3, *BMP-2 + load*: 26.63 mm^3; *in vivo*: *only BMP-2*: 60±12 mm^3, *BMP-2 + load*: 105±28 mm^3) and slightly overestimated it at 6 weeks post-operation (*in silico*: *only BMP-2*: 141.32 mm^3, *BMP-2 + load*: 141.08 mm^3; *in vivo*: *only BMP-2*: 98±18 mm^3, *BMP-2 + load*: 115±27 mm^3). Good agreement was observed at 4 weeks post-operation (*in silico*: *only BMP-2*: 102.00 mm^3, *BMP-2 + load*: 101.76 mm^3; *in vivo*: *only BMP-2*: 110±20 mm^3, *BMP-2 + load*: 118±30 mm^3).

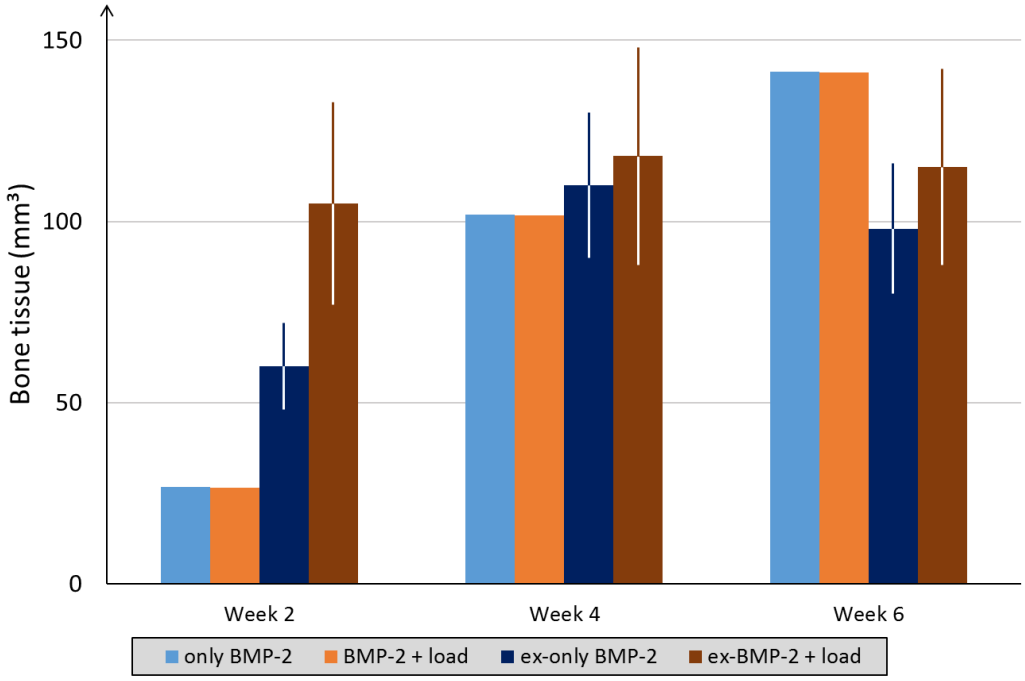

Figure 3.20. – Quantitative comparison of bone tissue volume between computer model and experimental data (average±SD) [45] at 2, 4 and 6 weeks post-operation for only BMP-2 *and* BMP-2 + load *case studies. Note: ex- prefix in legend identifies experimental data set.*

When the influence of additional mechanical loading on BMP-2 release was taken into account in the model, the additional release of BMP-2 favored bone formation during the first days post-surgery. From a qualitative point of view, no considerable differences were observed in tissue patterning over the course of healing: also in this case healing of the defect happened through periosteal bridging already at 2 weeks post-operation (Figure 3.21.).

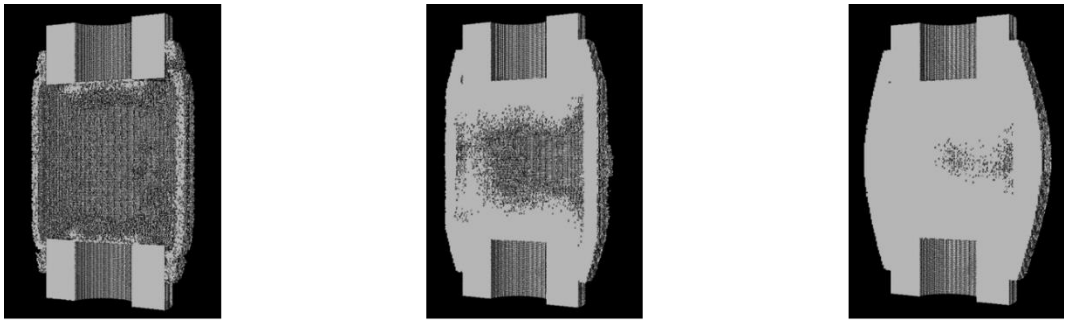

Figure 3.21. – Predicted bone spatial distribution within the callus domain at 2, 4 and 6 weeks post-operation under BMP-2 + load *case conditions. Note: BMP-2 dynamics were regulated by mechanics.*

From a quantitative point of view, the mechano-regulation of BMP-2 dynamics had a larger effect on the overall bone tissue formation process in the initial phases of healing. The inclusion of BMP-2 mechano-regulation showed that additional external loading promoted bone formation within the defect during the first weeks post-operation. In fact, at 2 weeks post-operation higher bone tissue volume was predicted when BMP-2 was mechano-regulated compared with the *only BMP-2* case (+1.51 mm^3) (Figure 3.22.). However, the effect diminished through time (Week 4: +0.61 mm^3, Week 6: -0.19 mm^3) (Figure 3.22.).

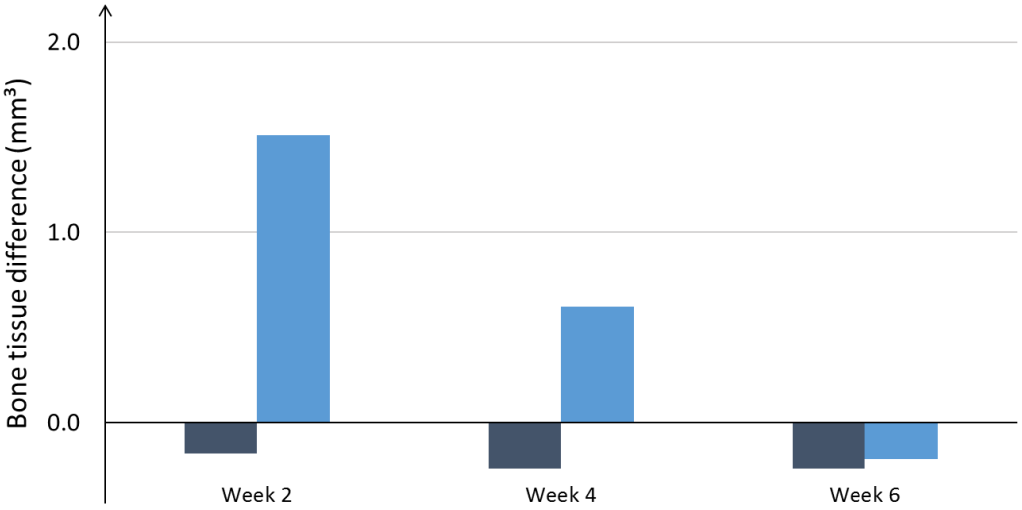

Figure 3.22. – Predicted difference in bone tissue volume between BMP-2 + load *and* only BMP-2 *case studies when mechanical regulation of BMP-2 was included (light blue) or not (dark blue).*

These results trend fitted with experimental data [45], where the significant contribution of additional mechanical loading on BMP-2 treated rat defect healing was only observed at 2 weeks post-operation. However, from an absolute point of view, the values did not fit with the μCT data and the mechanical contribution was predicted to be drastically smaller than the one observed in the experiments [45].

3.2.7. Untreated large bone defect healing led to non-union if cellular processes are limited to the first stages of healing

When limited cellular activity was imposed after 10 days post-operation, the predicted amount of cells involved in the healing process strongly decreased. Under this condition, the model correctly predicted non-union when BMP-2 treatment was not provided in both *control* and *only load* case studies. The limited cellular activity stopped the deposition of newly formed bone in the advanced stages of healing. No difference in bone patterning was observed between 4 and 6 weeks post-operation for both cases (Figure 3.23.). Bone tended to form both endosteally and periosteally from the first iterations. At 2

weeks post-operation, bone tissue was present within the endosteal region in the proximity of the medullary cavity and in the periosteum of the bone cortex (Figure 3.23.). From that time-point on, bone was observed to further form to consolidate the already formed structures but not to expand through the defect opening. At week 4, a consolidation of the medullary cavity encapsulation and of the periosteal bone could be observed (Figure 3.23.). Negligible changes in tissue patterning were observed at the following time-point (Figure 3.23.).

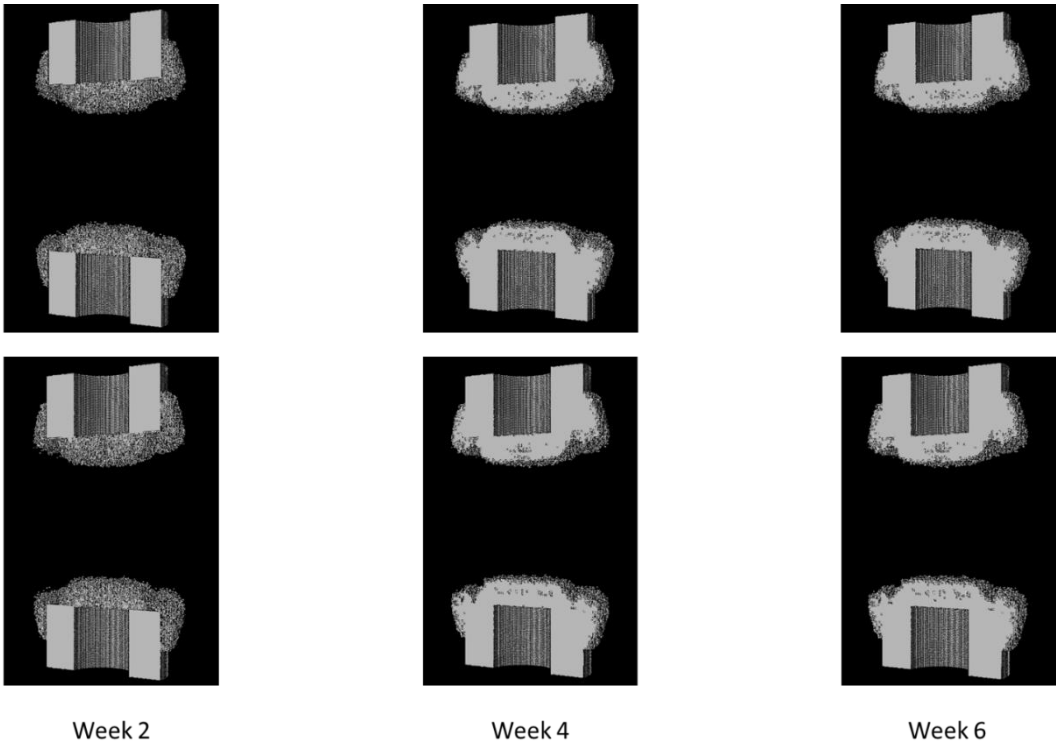

Figure 3.23. – Predicted bone spatial distribution within the callus domain at 2, 4 and 6 weeks post-operation of control *(top) and* only load *(bottom) defect healing case studies. Note: cellular activities were limited to the first 10 days of healing.*

Complete healing was also predicted under BMP-2 treatment under limited cellular activity. Under BMP-2 treatment, bone formed in the periosteal region of the callus following the chemotactic attraction of BMP-2. This resulted in the formation of a bone bridge around the collagen sponge region, at 2 weeks post-operation (Figure 3.24.). The callus was predicted to thicken over time and a consolidated bridge between the two extremities was predicted at 4 weeks post-operation (Figure 3.24.). Differently than the *control* cases, bone deposition was observed to continue after 4 weeks. At week 6, despite the limited cellular activity, further thickening of the bone bridging was predicted, with the creation of a rigid hollow callus (Figure 3.24.).

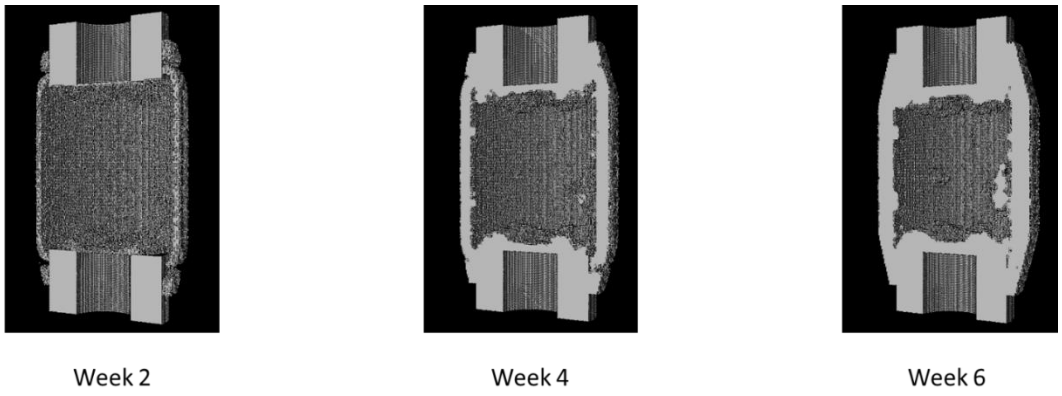

Figure 3.24. – Predicted bone spatial distribution within the callus domain at 2, 4 and 6 weeks post-operation under only BMP-2 *case condition. Note: cellular activities were limited to the first 10 days of healing.*

Additional mechanical loading was predicted to play a role in defect healing treated with BMP-2 under limited cellular activity after 10 days. In fact, despite the fact that bone tissue patterning followed analogous dynamics as the *only BMP-2* case, more bone was predicted to form when additional mechanical loading was provided. Bone bridging was still observed to form at week 2 and it consolidated at week 4 and week 6 (Figure 3.25.). Thicker bone bridging due to a higher bone deposition was predicted when additional mechanics was weekly provided (Figure 3.25.).

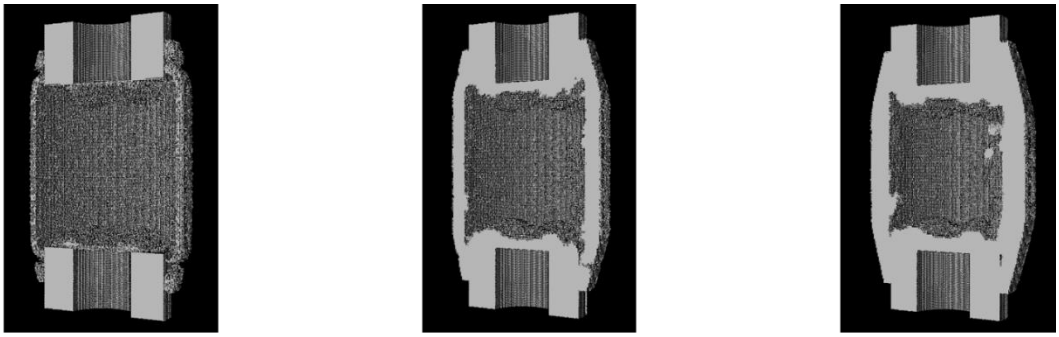

Figure 3.25. – Predicted bone spatial distribution within the callus domain at 2, 4 and 6 weeks post-operation under BMP-2 + load *case condition. Note: cellular activities were limited to the first 10 days of healing and BMP-2 dynamics were not mechano-regulated.*

Under additional mechanical stimulation, the bony connections between the defect extremities were characterized by more bone tissue than under BMP-2 treatment alone. A difference in volume quantity was predicted after 3 weeks post-operation. No difference was predicted at 1 (*only BMP-2*: 1.83 mm^3, *BMP-2 + load*: 1.83 mm^3) or 2 weeks (*only BMP-2*: 26.65 mm^3, *BMP-2 + load*: 26.55 mm^3) post-operation (Figure 3.26.). Instead, from the following time-points on, the mechanical stimulation was predicted to have an enhancing effect on bone tissue area. Noticeable differences were predicted at 3 weeks (*only BMP-2*: 45.51 mm^3, *BMP-2 + load*: 51.46 mm^3), 4 weeks (*only BMP-2*: 61.27 mm^3, *BMP-2 + load*: 69.21 mm^3), 5 weeks (*only BMP-2*: 76.16 mm^3, *BMP-2 + load*: 84.53 mm^3) and 6 weeks (*only BMP-2*: 85.62 mm^3, *BMP-2 + load*: 94.21 mm^3) post-operation (Figure 3.26.).

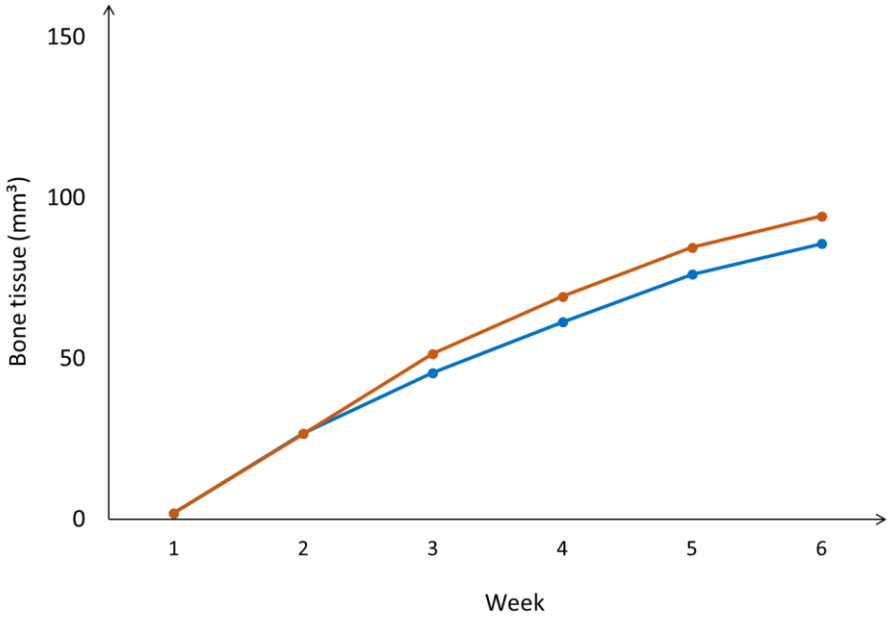

Figure 3.26. – Predicted bone tissue volume under only BMP-2 *(blue) and* BMP-2 + load *(orange) case studies when cellular activity was limited to the first 10 days post-surgery.*

The predicted mechanical environment within the defect showed that external mechanical stimulation resulted in mechanical conditions within the healing region favorable to bone tissue formation also in the latter stages of healing. Under BMP-2 treatment alone, the progressive stiffening of the callus due to bone bridging resulted in mechanical strains within the callus that favored bone resorption over formation. In fact, the hard callus formed at 6 weeks led to a drastic reduction of the compressive strains. At 6 weeks post-operation, under no additional mechanical stimulation, the strains within the callus were below 0.01, favoring bone resorption over formation in the endosteal region (0.002±0.001), intracortically on the lateral side (0.002±0.002) and intracortically on the medial side (0.003±0.002) (Figure 3.27B). The additional external mechanical load induced mechanical strains within the callus that further stimulated the formation of bone tissue (strains over 0.01) also when the hard callus was already consolidated. When additional mechanical loading was provided, the mechanical environment increased of one order of magnitude within the endosteal region (0.019±0.009), intracortically on the lateral side (0.028±0.014) and intracortically on the medial side (0.024±0.015) when compared with results under no additional mechanical stimulation (Figure 3.27C).

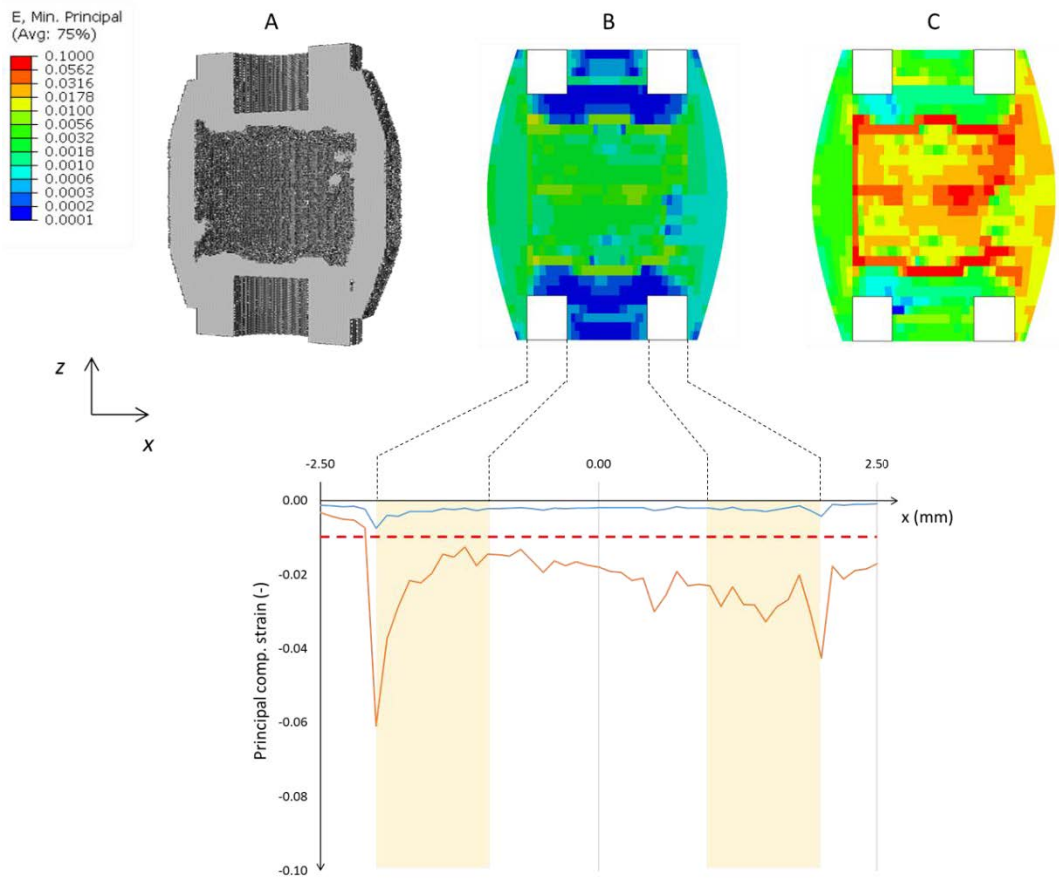

Figure 3.27. – Top: predicted bone tissue patterning (A) and minimal principal strain distributions at 6 weeks post-operation for only BMP-2 *(B) and* BMP-2 + load *(C) case studies. Bottom: average minimal principal strains distribution within the defect opening in the transversal axis (x) for* only BMP-2 *(blue) and* BMP-2 + load *(orange) case studies. Note: 0.01 strain limit for bone formation was reported in the plot (red dotted).*

3.2.8. Simulated spontaneous release of BMP-2 leads to predicted incomplete healing at 6 weeks

Immediate release of BMP-2 (no collagen sponge) led to the same predicted bone tissue patterning as observed in the *control* case (Figure 3.28.). The effect of BMP-2 on the promotion of bone healing at the cellular level was limited to the very first days after surgery and the process followed the non-treated conditions after the first week of simulation. Incomplete healing was observed under BMP-2 treatment without gradual BMP-2 release at 6 weeks (Figure 3.28.).

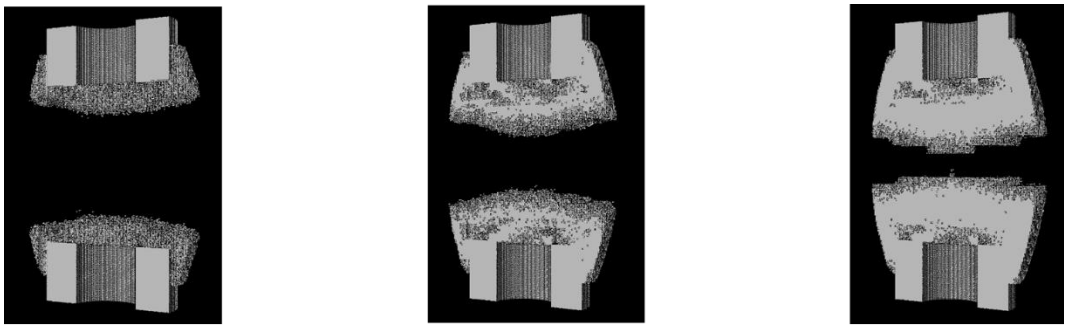

Figure 3.28. – Predicted bone spatial distribution within the callus domain at 2, 4 and 6 weeks post-operation under only BMP-2 *case study conditions when BMP-2 was instantaneously released at the first iteration.*

3.2.9. Discussion

Large bone defect healing is a compromised condition which if left untreated leads to a non-union [45] [114]. Mechanical as well as biological alterations within the healing region have been reported [115]-[117], however it remains largely unknown how those alterations contribute to impaired healing. This study investigated how mechanical and biological interactions at the cellular and tissue levels contribute to the bone healing outcome. A multiscale computer model was developed to simulate healing within a large femoral defect in rats and to investigate the mechanobiology of large bone defect healing at both cellular and tissue levels.

Large bone defect treatment with BMP-2 results in complete healing often characterized by periosteal bone bridging [11] [45]. Although several biological processes have been reported to be influenced by BMP-2 [48] [49] [75] [76], their relative contribution to bone tissue patterning remains unknown. In this study, the therapeutic effect of BMP-2 on large bone defect healing was additionally investigated at the cellular and tissue levels to unravel which cellular mechanisms might lead to periosteal bridging. The computer multiscale computer model was further developed to simulate the dynamics of BMP-2 concentration within the callus domain and its influence on cellular behavior, following BMP-2 dosage-related rules [74].

The computer model results showed that large bone defects result in an unsuitable mechanical environment for bone healing. The defect mechanical environment favored the encapsulation of the marrow cavity, compromising the bridging between the defect extremities. In several *in vivo* studies, non-unions due to medullary cavity encapsulation were observed in challenging conditions [44] [45] [115] [118]. The proposed *in silico* model showed that altered mechanics alone were not able to explain the non-union fate that characterized large bone defects. In non-treated large bone defects, non-union after 6 weeks was only predicted by the model when cellular activities within the healing region were limited. The cellular activities were limited to the first 10 days post-operation to reproduce potential

compromising effects on cells due to the large defect situation. The simulated lack of cellular motility and proliferative capacity after 10 days led to the arrest of bone formation over time. Impaired vascularization within the defect could trigger the simulated compromising condition at the cellular level. The compromising role of low blood supply was investigated in an *in silico* large bone defect model which included angiogenesis [72] [119], where they showed that limited vascularization could explain non-unions in large bone defects. However, these models were not able to explain the closure of the medullary cavity as observed experimentally and did not include alterations in the mechanical environment within the defect and its effect on cellular behavior.

To investigate the influence of BMP-2 on cellular activity and its consequences at the tissue level, the effect of BMP-2 on the cell dynamics was implemented in the model. The presented model correctly simulated bone bridging from the periosteal side of the callus under BMP-2 treatment. An analysis at cellular level showed that cellular chemotaxis induced by the growth factor favored the controlled migration of MSCs, allowing the formation of a connection between the defect extremities, which was not observed under untreated conditions. The presented model identified a potential mechanism behind tissue formation patterns observed under BMP-2 stimulated conditions. The predicted BMP-2 concentration pattern showed that chemotactic attraction was stronger in the periosteal side of callus in the first weeks post-operation The cells were mainly attracted to migrate towards the periosteal side of the callus domain, in the proximity of the collagen sponge. As bone healing was observed to happen through bridging within this region, it was concluded that BMP-2 chemotaxis played a primary role in successful healing and it could explain periosteal bridging observed at 2 weeks post-operation. Although other models have investigated BMP-2 stimulated healing [74], this is the first study to explain periosteal bone bridging. Differently than in previously published *in silico* studies on the role of BMP-2 in large bone defects, where BMP-2 was affecting the cellular density dynamics through time [73] [74], in

this model single cell behavior was simulated according to the surrounding BMP-2 density. Including the cellular level highlighted the role of BMP-2 dose-regulated migration of the cellular population on the overall enhancement of the critical sized defect healing treated with BMP-2.

Mechanical signals have been shown to influence the effect of BMP-2 on bone regeneration [120]. Experimentally, it was shown that external mechanical loading further promotes bone defect healing treated with BMP-2 at the early healing stages [45]. To investigate the role of additional mechanical loading on the bone healing process, the weekly *in vivo* mechanical loading described by Schwarz et al. (2013) [45] was implemented in the model. The *in silico* model also predicted a slight increase in bone tissue volume during the first weeks post-operation under additional mechanical stimulation. Enhanced bone tissue formation was due to the major release of the growth factor on weekly basis provided by the external loading. However, when additional mechanical loading was limited to regulate cellular activity (MSC differentiation pathway, cellular proliferation and apoptosis), the model was not able to reproduce the effect of additional mechanics on BMP-2 treated defect healing. Therefore, mechanical stimulation of BMP-2 release seems to play a higher role than mechanical enhancement of cellular activity during BMP-2 treated bone defect healing. Further studies on the optimization of growth factor release kinetics could provide a means to promote bone regeneration.

Implementation of BMP-2 release from the collagen sponge was fundamental to predict complete healing under BMP-2 treatment. If the initial dose of BMP-2 was entirely released within the defect since the first iteration, computer model predictions resulted in non-union, as in the untreated *control* case. Delayed healing and marrow encapsulation were predicted due to the fast degradation of the growth factor, which led the treatment to be completely consumed in less than a week. The gradual release allowed a continuous provision of BMP-2 through the whole healing period. The immediate release, in fact, showed short treatment time-span and no effect was experienced anymore after one week of treatment (Figure 3.17.). The shorter half-life of

BMP-2 (0.42 days [121]) compared to that in its encapsulated form (3.25 days) led to a fast reduction of the substance to physiological values already in the first days of treatment. The gradual release led to reduced consumption of the BMP-2 and physiological concentration levels were not predicted to occur in days but in weeks. Extended BMP-2 provision has been shown to enhance bone defect healing also experimentally [122]-[124]. The computational model proposed here could help to investigate the best release dynamics to promote healing under specific conditions and use adequate support structures for the provision of BMP-2 or alternative growth factors. In agreement with the results, slow release of growth factor showed better treatment response also in the bone healing computer models of Peiffer et al. (2011) [125], which showed faster angiogenesis when an injectable slow release Vascular Endothelial Growth Factor (VEGF) carrier was simulated.

The *in silico* model was subject to several limitations. For example, the computer model predicted higher bone formation and the encapsulation of the marrow cavity was characterized by more bone tissue than in the experiments. Computer model predictions showed continuous bone tissue formation endosteally over time, which resulted in an overall overestimation of bone tissue volume at every time-point. Defect non-union, which happened experimentally in critical size untreated conditions, was not predicted *in silico*. The bone defect model correctly predicted incomplete healing in 6 weeks when the defect was left untreated. However, computer model predictions of bone tissue patterning over 6 weeks showed delayed healing. Different reasons could be proposed to explain the prolonged process of bone formation, even under challenging healing conditions. For example, the computer model did not take into consideration different signaling processes at cellular level that could be affected by the challenging conditions. Moreover, angiogenesis was not taken into consideration and oxygen supply to the cells was always simulated to be 100%. Critical healing conditions generate a challenging environment for proper angiogenesis within the defect opening [44]. In the model, instead, the critical defect created challenging conditions

only from the mechanical point of view. Even if mechanics were observed to be characterized by reduced strains in large bone defects [115], the mechanical alteration alone was not enough to explain the observed non-unions. Only when cellular activities were limited to the first stages of healing, to extend compromised condition to the biology of defect healing, the model correctly simulated non-union. This compulsory requirement of the model underlined the importance of the compromised aspects at cellular level associated with the large defect condition, over the already mentioned effects due to the altered mechanical environment within the healing region [115].

Furthermore, the extension of mechanical regulation to BMP-2 release and diffusion resulted in additional bone tissue production at 2 weeks post-surgery. However, the improvement proposed by the model was still minor, if compared with *in vivo* results [45]. In the proposed model, a two-fold increase of BMP-2 release and diffusion was arbitrarily provided to test if additional release could explain the major bone production. The model demonstrated that the mechano-regulation of BMP-2 dynamics should not be underestimated to fully describe the mechanical contribution to BMP-2 treated large defects. However, further regulation algorithms should be investigated for their potential to describe the patterning of the growth factor when subject to additional external mechanical loading. In future models, the growth factor should follow the dynamics of the extracellular matrix within the callus. The predicted interstitial fluid flow velocity distribution could be used to describe the motion of BMP-2 within the extracellular matrix. In this study, the effect of BMP-2 on cellular activity was limited to cell migration, proliferation and tissue formation. Other cellular processes might also be enhanced by BMP-2. The proposed model was based on state-of-the-art literature reviews on the effect of BMP-2 on cellular activity [74]; however, further studies are needed to investigate other potential mechanisms.

In summary, the multiscale rat large bone defect healing model correctly predicted experimentally observed non-unions only when cellular activities were limited to the initial stages of healing. The mechanical patterns observed

within the critical sized defect, characterized by smaller mechanical stimuli than in a normal size defect or fracture, could not explain alone incomplete healing as observed experimentally [45]. Moreover, mechanical stimulation was predicted to play a minor role in the healing outcome in an untreated large bone defect. In addition, BMP-2 within the defect opening was revealed to play a strong role in the regulation of cellular dynamics. In particular, the BMP-2 chemotactic effect on cellular behavior was predicted to be central in the formation of periosteal bone bridging, as observed experimentally [45]. The presented model highlighted BMP-2 dose-dependent chemotaxis to play the main role in the promotion of healing. New treatment strategies of large bone defects based on growth factors should consider the release kinetics of the stimulating factors and optimize it to achieve successful healing outcomes.

4

CONCLUSIONS

The project developed within this doctoral thesis aimed to investigate how mechanics influences bone regeneration in compromised bone healing conditions. Although bone is able to self-regenerate, in multiple conditions its regeneration capacity can be hindered leading to delayed or non-unions. This work investigated how the local mechanical environment within the healing region influences the biological processes that are altered in compromised healing conditions. Specifically, the role of mechanics on the compromising effects of aging and large size bone defects was investigated. Fracture stabilization has been experimentally shown to lose its importance with aging. Computer models were developed to investigate which age-related alteration at the cellular level better explained this compromised condition. Reduced cellular mechanosensitivity alone was able to reproduce the minor response to changes in fixator stiffness associated with aging (Figure 4.1.). The critical sized bone defect was experimentally shown to result in a non-union. Computer simulations showed that altered mechanics within the healing region combined with limited cellular activity due to the large defect could explain experimental observations (Figure 4.1.). A therapeutic treatment was investigated by integrating into the model the effect of BMP-2 on cellular activity within the large defect. Computer model simulations showed that BMP-2 driven chemotaxis was able to explain experimentally observed periosteal bone bridging (Figure 4.1.). The acquired knowledge will be valuable to identify future treatments of bone fracture under critical healing conditions.

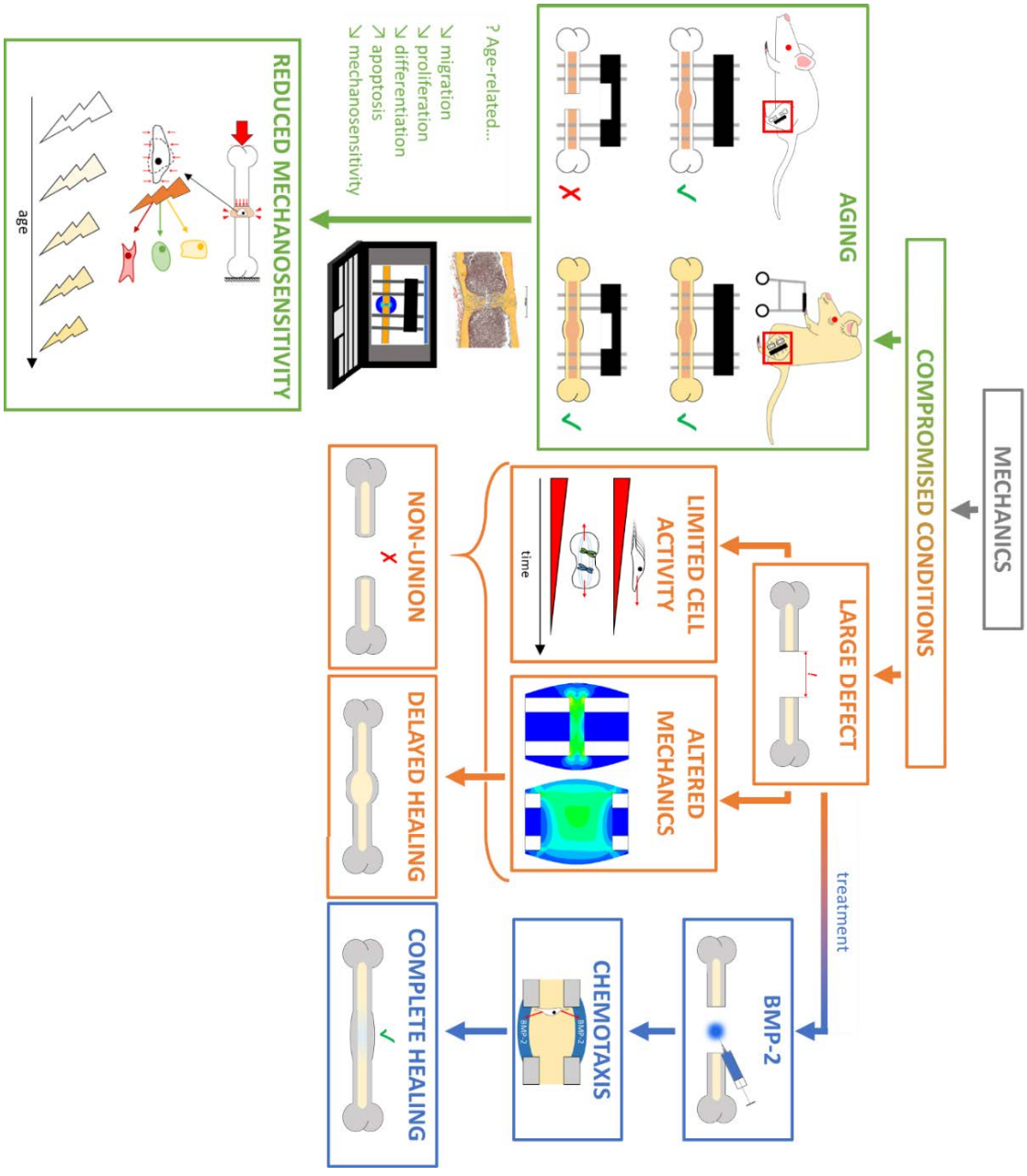

Figure 4.1. – Graphical abstract: overview of the project main questions and results.

In the first part of the project, finite element (FE) modelling was used to determine the mechanical environment within the healing region in a mouse osteotomy model under two different fixation stabilities: a rigid and a semirigid external fixator. The rigid fixator was characterized by circa 10-fold higher axial stiffness compared with the semirigid fixator. This difference in the mechanical stability showed *in vivo* an influence on bone healing progression in adult mice. Under semirigid conditions, bone healing was delayed and showed higher amounts of cartilage formation within the osteotomy gap. The FE results showed up to three times higher compressive principal strain and interstitial fluid flow velocity under semirigid compared with rigid external fixation. These results were thereafter used to identify mechano-regulatory rules with the potential to explain differences in *in vivo* tissue patterning under the two proposed fixation strategies.

A mechanobiological model was thereafter developed to investigate how the mechanical conditions within the healing region regulate the bone healing process. It was found that in mice, bone healing happens under higher mechanical stimulation than in larger animals. Inter-species differences in the mechanical regulation of bone healing have been already reported between rat and sheep [61]. Here, it has been shown that also between species of similar anatomy (mouse and rat), differences in the mechanical regulation of bone healing exist. These results are relevant for the design of fixation devices for veterinary fractures, where devices should be designed individually for the specific species.

Based on mouse bone osteotomy healing histological images, it was proposed an alternative mechano-regulatory rule to predict bone healing in mice under different stabilization conditions. A new mechano-regulatory rule was proposed to correctly interpret the dynamical evolution of the tissue patterning observed during the mouse bone healing process under different mechanical environment conditions. When the new mechano-regulatory rule was implemented, the model predicted the same healing outcome observed experimentally in mouse osteotomy healing under both rigid and semirigid

fixation conditions. Following the same methodology, the proposed computer model could be extended to the investigation of the mechano-regulation of healing in other animal models and, furthermore, in human patients.

In vivo experiments showed that with aging there was a reduced bone healing response to changes in fixation stability. While adult mice showed a clear effect of mechanical osteotomy stabilization, elderly mice showed no effect of fixation on the healing progression. Experimentally, many factors have been associated with age-related alterations in bone healing: reduced cell number, slower cell migration, decreased cellular proliferation and differentiation. The aim of this study was to investigate the contribution of age-related alterations at the cellular level to the overall bone healing process. In the proposed model, selected biological factors were altered at the cellular level to investigate the differences observed in bone healing between adult and elderly mice. The study simulated the mechanical environment under rigid and semirigid fixations to investigate the minor effect of fixation stability *in vivo* in elderly, compared with adult mice. A multi-parametric study was performed to identify how selected age-related changes at the cellular level could influence bone healing outcome. Multiple cellular parameters were selected and altered to evaluate their contribution to the age-related alteration of bone healing. The results of the analysis of variance showed that reduced mechanosensitivity has the highest influence on predicted bone and cartilage tissue formation during healing in mice. Moreover, while other age-related alterations at the cellular level were not able to explain bone healing in elderly mice, the inclusion of altered MSC mechanosensitivity correctly simulated tissue patterning observed *in vivo*. This result can have clinical resonance in the evaluation of optimal fixation strategy in patients, as it seems that mechanical stimulation has less impact on elderly patients due to reduced mechanoresponse of the cells. Altered mechanosensitivity will result in reduced response to physical rehabilitation in elderly patients, which is known to play a central role in enhancing healing performance in patients. Alternatively, from this outcome, it was derived that in adult patients the choice of the osteotomy stabilization

device plays a higher role than in elderly. Additional studies on human patients should be conducted to confirm these observations in mice.

Healing of large bone defects remains a clinical challenge [44] [45] [115] [118]. In this study, the bone healing process within a large defect was investigated using computer models. In accordance with previous studies [115], FEA predicted lower mechanical strains within a large bone defect, compared with a small gap. Reduced mechanical stimulation could explain marrow encapsulation, however the model predicted delayed defect healing instead of a non-union. Only if cellular activities within the healing region were limited to the first days post-operation, bone defect computer models predicted a non-union, as experimentally shown in critical sized defects in rats [45]. These results showed that mechanical alterations due to critical size defect alone were not able to explain experimental observations. The inclusion of alterations in the biological environment due to the large gap (reduced vascularization, impaired signaling) was necessary to correctly predict incomplete healing.

Experimentally, the treatment of large bone defects with BMP-2 promoted healing and avoided non-unions [11] [45]. The computer model simulated the dynamics of cellular patterning and BMP-2 concentration to investigate the primary mechanisms leading to enhanced healing in critical conditions. The effect of BMP-2 treatment was investigated *in silico* by regulating specific cellular activities (migration, proliferation, tissue production) according to the BMP-2 concentration within the callus. *In silico*, the computer model showed that the role of BMP-2 on the regulation of cellular migration, promotion of cellular proliferation and enhancement of bone tissue formation can explain the experimentally observed periosteal bridging of a large defect treated with BMP-2. In particular, the simulation of the spatial and temporal distribution of tissues, cells and BMP-2 within the healing region led to the identification of BMP-2 driven cell chemotaxis as a main driver of the experimentally observed tissue patterns. This outcome highlighted enhanced chemotaxis as a potential target in the future treatment of critical size bone defects.

To investigate the influence of mechanics on BMP-2 treatment, the effect of weekly external mechanical stimulation was additionally simulated for its potential to further promote healing. *In vivo*, the external loading was observed to enhance the healing of BMP-2 treated bone defects in the early stages [45]. The computer model predicted enhanced bone tissue formation only if the effect of external mechanics influenced the regulation of BMP-2 release and diffusion. This observation could open the road to the investigation of a more effective loading to stimulate fast healing in BMP-2 treated patients. It should not only enhance cellular activity but also control the optimal release and diffusion of the growth factors within the healing region. Loading magnitude and stimulation frequency could be parameters used to optimize the outcome of mechanically treated, growth factor stimulated defects.

An additional model of rat critical sized defect treated with BMP-2 was run to investigate the necessity of using a support structure to slowly deliver the BMP-2 within the defect opening. The model was characterized by a collagen sponge release dynamics to simulate the gradual release of BMP-2 within the defect. When the growth factor was simulated to be instantaneously released, delayed healing was predicted, as in untreated conditions. The BMP-2 concentration was subject to fast degradation when the substance was completely released at the initial stages. The enhancing effect of BMP-2 was limited to the first 10 days of healing, while with gradual release the effect was prolonged for weeks. This result highlighted the importance of using an adequate support to provide the treatment with the right timing and avoid premature degradation of BMP-2.

The results obtained from this project highlight the potential of computer models to simulate processes at different length- and time-scales. They allow the investigation of many aspects of bone healing which are not visible *in vivo* or challenging to measure. The flexibility of the analysis, moreover, permits the evaluation of specific features role to weight their importance on the overall process. With this *in silico* study, for example, it was possible to identify

the strong points of a growth factor therapy to evaluate alternative treatment strategies that involve analogous features. In the future, the same investigation road should be followed to highlight how a specific treatment (or, vice versa, a specific compromising condition) is involved in promoting (spoiling) a biological process.

Future work

As already reported, the computer models developed in this project were subject to some limitations. Computational simulations of such a complex process (bone regeneration) need to be subject to some compromises to reduce the complexity of the analysis. The proposed model aimed to simulate bone healing at different time- and length-scales, taking into account both mechanical and biological interactions. In the following paragraphs, some limitations are recalled and suggestions are given for future improvement.

Regarding the FE model, the geometry of the mouse and rat bones were simplified to hollow cylinders with homogeneous material properties to reduce the computational complexity. In the future, a realistic geometry of the long bone with the assignment of material properties as a function of the bone mineral density could be used to better reproduce the conditions of case-specific bone osteotomies. This might be particularly important if similar models are used to investigate bone regeneration in humans, where fractures will not be standardized as in the studies described here.

A new mechano-regulatory rule was proposed to adapt to high mechanical stimuli in mice but the results showed an overestimation of bone tissue formation in semirigid models. This problem was more evident in the latter remodeling stage of healing. Future models should better define the mechanical regulation of bone formation-resorption balance, which regulates bone remodeling in the last phases. In addition, the arrangement of oriented collagen fibers is known to guide tissue mineralization [126] but the proposed model did not consider its effect. Collagen fiber patterning and other biological

parameters (angiogenesis, immune signals …) could be added to the models to investigate their role in the healing outcome.

Age-related alterations of bone healing in mice were investigated with the help of Design of Experiments (DOE). The analysis of the multiple factors that alter healing performances in aged mice was performed by pinpointing the ones that most affect bone formation. To reduce the number of simulations, this study limited the DOE test to only two levels: one adult and one elderly level. Furthermore, the elderly level value was characterized either as a halving or a doubling of the adult level. Future studies should include additional age-related variations of the selected parameters. Otherwise, the parameters that were identified in this study as the most influential should be tested on a larger variability of values to represent the elderly level. In addition, to avoid excessive computational complexity, the study was limited in the number of parameters to investigate. Even if the chosen ones were taken from the literature, many other biological aspects were kept out of the investigation. As an example, aging also leads to changes in the immuno-regulation [127]-[129] and angiogenesis [130]. In the presented model, the mentioned parameters were not included. It would be interesting to extend the investigation of age-related alterations of bone healing to other biological factors in future models.

Non-union of critical sized bone defects was explained by the reduced cellular activities associated with the compromised biological environment. To simulate the critical healing condition, the cellular activities were limited to the first 10 days post-operation. After this period, the cell population stopped migrating, proliferating and differentiating. In the future models, the limitation of cellular activities should be regulated by critical healing conditions which are known to be related to the size of the defect. For example, the oxygen delivery within the healing region is compromised in large sized defects due to the slow restoration of the vasculature system [72]. As mentioned above for the aging condition, the inclusion of angiogenesis and other biological regulation should better simulate how the challenging conditions operate at

the cellular level to investigate the role of each contribution on the overall compromised healing process.

The model investigated the role of BMP-2 on the enhancement of large bone defect healing in rats. However, the study was limited in the number of BMP-2 regulated parameters involved. The model includes the same effect of BMP-2 on cells already investigated by Ribeiro et al. (2015) [74]. In the future, additional cellular parameters regulated by BMP-2, such as the promotion of cartilage formation and osteogenic differentiation, should be included. Moreover, BMP-2 is known to stimulate vascularization, through the enhancement of endothelial cell activities [131]. The agent-based computer model should further include those cells to investigate if enhanced angiogenesis could explain defect healing under treated conditions. Over the investigated BMP-2 enhancements at cellular level, MSC chemotaxis was shown to play a main role to bridge the bone in critical sized defect conditions. In the future, it should be further investigated if BMP-2 regulated chemotaxis alone is a sufficient condition that leads to complete defect healing or the enhancement of other cellular biological factors are necessary. Thereafter, the computer model highlighted the biological factors enhanced by BMP-2 that promote specific cellular activities, which have a primary role in the overall bone healing enhancement.

In the presented model, the external loading was observed to promote large defect healing under treated conditions only if BMP-2 dynamics within the healing region was further regulated by mechanics. This result put in the background the mechano-regulation of healing at cellular level, which has a minor role than the one at the BMP-2 level. To reproduce the defect healing case studies investigated experimentally [45], the proposed model simulated the effect of external loading only on a weekly basis. More frequent provision of external loading could extend the upregulation of specific aspects at cellular level to regulate healing at the macroscopic level. Future *in silico* studies could be performed to optimize the mechanical parameters.

APPENDICES

A

Finite element model characterization

A.1. Influence of callus domain dimensions on tissue patterning

To reduce the complexity of the bone healing computer model, several simplifications were implemented. As our model was recursively calling the FE analysis multiple times, the simplifications allowed to speed up the investigation. Simplifications ranged from the geometry of the model (the bone cortex was idealized as a hollow cylinder) to the characteristics of the materials (mechanical properties were considered isotropic). The size of the callus domain was a feature of the FE model that was optimized to reduce its complexity. The limitation in space provided by the domain affected the outcome of the model as the callus could only form within its boundaries. A larger domain was more suitable to avoid a limitation to tissue formation. In contrast, a larger callus requires more elements to generate the mesh in the callus domain geometry, which requires more calculation effort on the FE analysis. To investigate the influence of callus domain size on mouse bone healing outcome, three models were created. The geometry of the callus domain was investigated by changing the radius of the callus domain in

longitudinal direction: (S) 1.65 mm, (M) 2.00 mm, (L) 2.70 mm (Figure A.1.). The axial length was kept the same in all the three models: 3.50 mm.

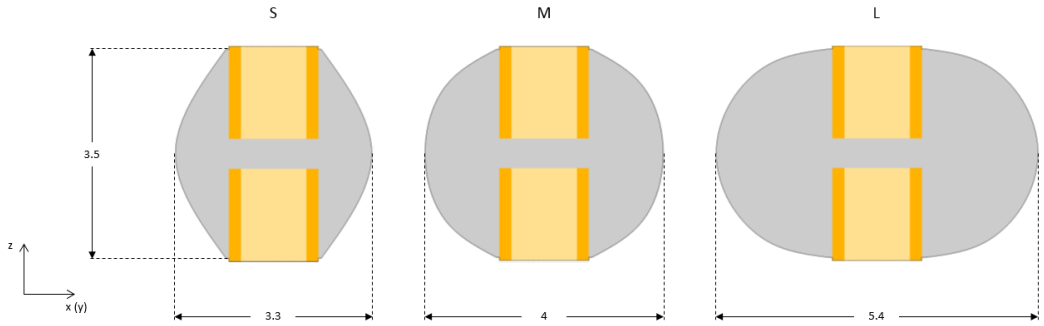

Figure A.1. – Three different callus domain sizes were investigated in the mouse osteotomy healing model.

The three mouse bone healing models were run to investigate the tissue patterning at 7, 14 and 21 days post-operation. The results of the models were compared among them to determine the influence of callus size on model predictions. Qualitative comparison between the results showed more bone formation within the osteotomy gap in S callus at days 14 and 21 (Figure A.2.). Cartilage formation was instead preponderant when the M and L callus sizes were adopted. Moreover, M and L conditions showed analogous tissue distribution within the osteotomy gap at day 14 and day 21 (Figure A.2.).

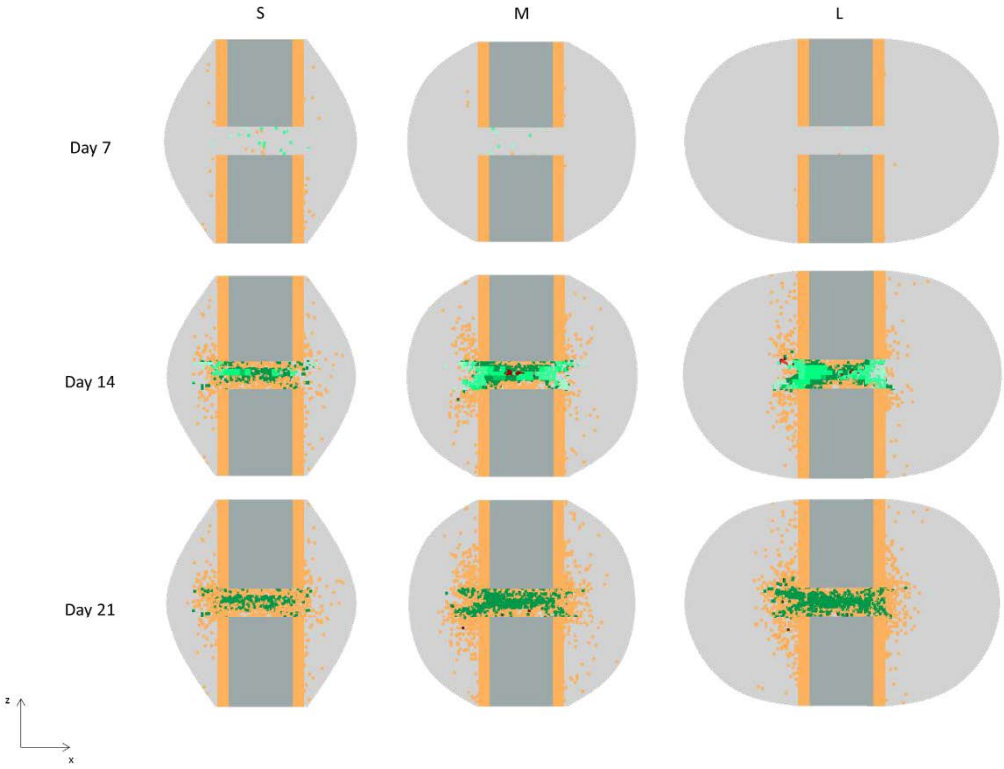

Figure A.2. – Tissue patterning predicted at 7, 14 and 21 days post-operation for different callus domain sizes under rigid external fixator. Dark yellow: bone, green: cartilage.

For our FE model of mouse bone healing, it was decided then to use the size M (2.00 mm radius). Size L would have required higher computational effort without any noticeable difference in the tissue patterning outcome. The M-sized callus domain was selected as a good compromise to guarantee enough space for callus development without constrictions. As no substantial differences were found with the L-sized domain, it was opted for size M to save computational effort. The study of the callus domain size was performed only on the mouse bone healing FE model, as the geometry of the bone was generated from scratch. The geometry of the rat bone healing model was obtained from previous work [61] and the callus domain size was kept untouched.

A.2. Influence of element size on FEM results

To guarantee efficient computational cost, the number of elements in the FE mesh of the geometry was minimized. Element size 0.20 mm was chosen to characterize the mesh size in the mouse bone healing model and 0.50 mm in the rat model. A large element size guarantees faster analysis but can negatively affect the precision of the analysis results. To reduce the loss of precision within the callus gap, which was the region of interest, without weakening the performance of the model, a compromise was reached: the size of elements within the callus domain was reduced while the rest of the element mesh size was kept to the original size. This guaranteed a more precise investigation of the mechanics within the osteotomy gap and avoided to excessively increase the computational cost. An investigation was performed on FE models to determine the best size of the elements within the callus. The study was conducted creating additional models that shared the geometry of the mouse and rat bone healing models but had reduced element size in the callus domain. The mechanical stimuli distribution within the osteotomy gap at day 0 was compared between the models to investigate the differences in mechanics associated with the different mesh sizes.

The investigation was iteratively conducted by halving the average mesh size. The distribution of primary compression strain within the osteotomy gap was investigated. The optimal element size was chosen when the average difference in compressive strains within the osteotomy region was observed to change no more than 1% if the element size would be further reduced. The results showed that with a 0.10 mm element size, further reduction of the element size would not affect the compressive strains within the gap region by more than the chosen threshold (Figure A.3.).

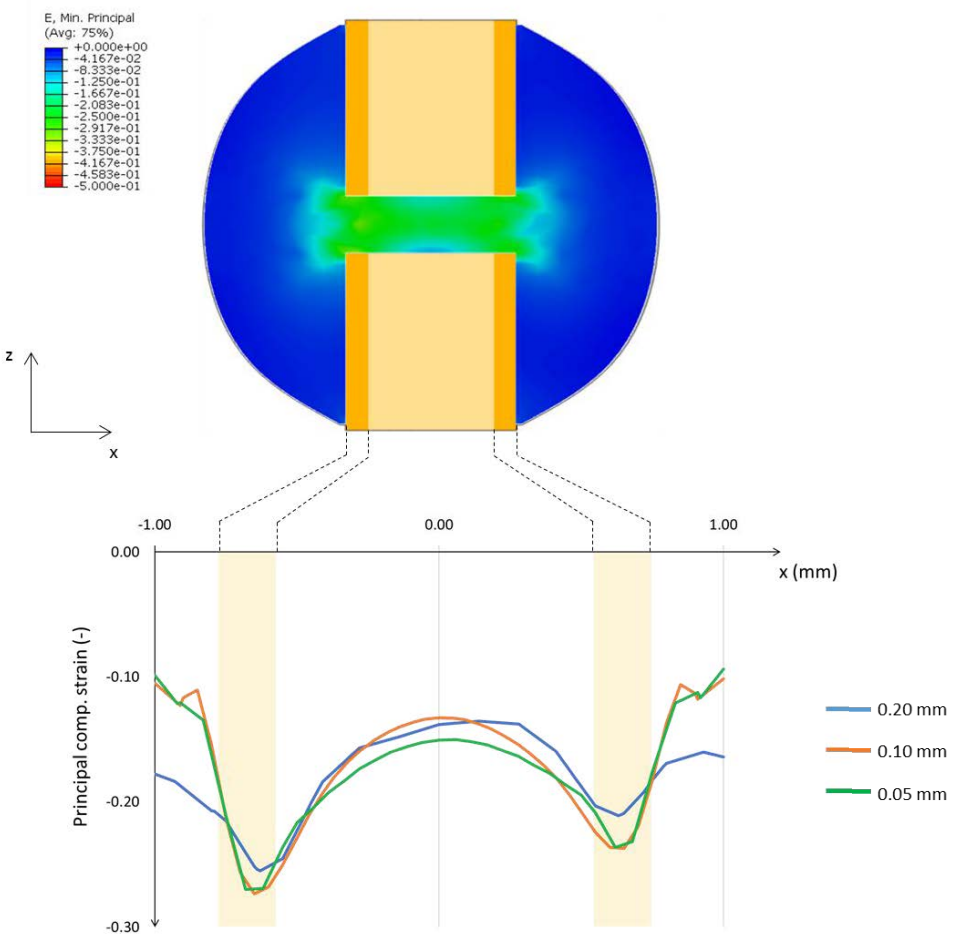

Figure A.3. – Top: minimal principal strain spatial distribution within the osteotomy gap with 0.10 mm size FE mesh immediately post-operation. Bottom: distribution through the transversal axis of minimal principal strains for the investigated element sizes. Note: only the rigid external fixator was used for this investigation.

From a quantitative point of view, the compressive principal strain with a 0.10 mm mesh size was analogous to those predicted with the finest mesh investigated (0.05 mm). In detail, small differences between the two were observed in lateral periosteum (0.10 mm: 13.8±5.5 %; 0.05 mm: 13.9±6.0 %), medial periosteum (0.10 mm: 12.6±4.7 %; 0.05 mm: 12.5±5.1 %), lateral intracortical (0.10 mm: 24.8±5.7 %; 0.05 mm: 24.3±6.6 %), medial intracortical (0.10 mm: 21.5±5.6 %; 0.05 mm: 20.9±6.2 %) and in the endosteum (0.10 mm: 17.9±6.2 %; 0.05 mm: 19.4±7.6 %). The use of a mesh characterized by larger elements (0.20 mm) generated substantial differences in compressive strains distribution: lateral periosteum (18.9±8.5 %), medial

periosteum (16.4±7.4 %), lateral intracortical (22.4±8.8 %), medial intracortical (18.8±7.5 %) and in the endosteum (15.4±8.4 %).

To reduce the calculation complexity without compromising the prediction results, a 0.10 mm element size was chosen to describe the callus domain mesh in both mouse and rat bone healing models.

B

Mechano-regulation of cell differentiation in mouse model

Bone healing mechanics were observed to be characterized by higher stimuli in mice than in rats. The rule that drove mechano-regulation of MSC differentiation in rats and sheep bone healing models [61] was not able to reproduce the mechanical regulation of bone healing in mice. Under those conditions, in fact, the FE model incorrectly predicted fibrous tissue presence within the osteotomy gap in mice at day 21 post-operation. The simulated mouse bone osteotomy gap was characterized by higher mechanical stimuli S, which was defined as a linear combination of octahedral shear strain and fluid flow velocity. The differentiation algorithm of the cellular distribution model evaluated the mechanical stimuli S which each MSC was subjected to determine its differentiation fate (*§ 2.2.2., Cell differentiation*). To adapt the algorithm, the boundaries of each phenotype differentiation range were modified to respond to higher mechanical stimuli S values. *In vivo* histology data from mouse osteotomy experiments and the mechanical environment

predicted by the FE model within the osteotomy gap were compared to find a relationship between the mechanical stimuli S and the desired tissue. Multiple tests were performed due to the dynamical variation of the mechanical properties within the osteotomy gap due to callus stiffening through the process. The predicted distribution of mechanical stimuli was coupled with the tissue patterning observed on the histological images to define the differentiation ranges for each case study (Figure B.1.).

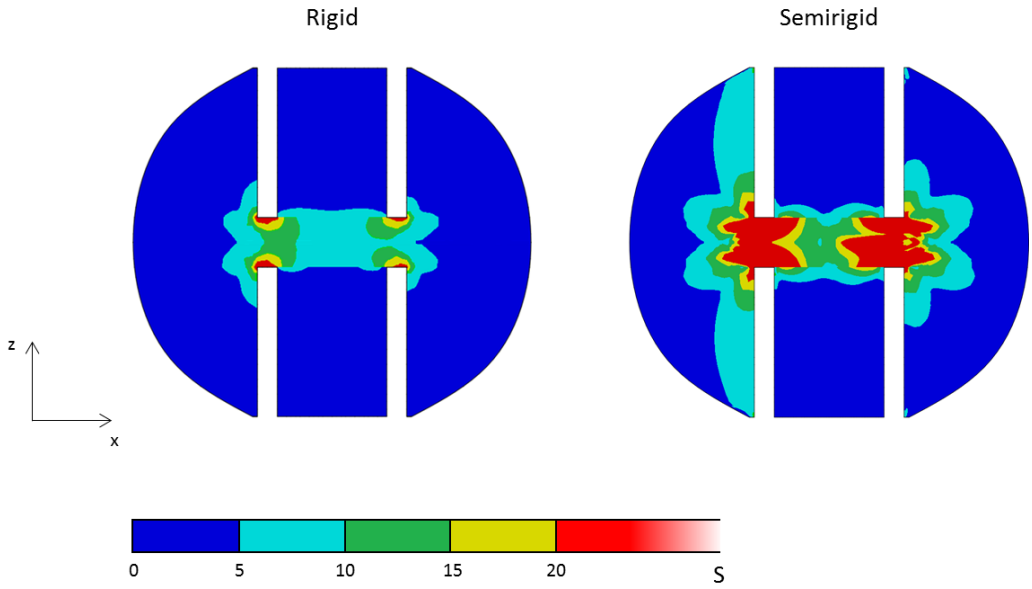

Figure B.1. – Mechanical stimuli S distribution within the mouse bone osteotomy under rigid and semirigid conditions immediately post-operation.

The comparison between tissue patterning at day 7 post-operation and the mechanical environment predicted by our model at the initial stage was indicative to investigate the mechano-regulation of the first phases of healing. As already mentioned, the differentiation algorithm was adapted to respond to higher stimuli. To avoid the immediate formation of hard callus, the mature osteoblast range was kept almost untouched while immature osteoblasts and chondrocytes ranges were extended to include higher S values (Table B.1.). In addition, the mechanical stimuli range of fibrous tissue formation, which was not observed *in vivo* at any stage of healing under both rigid and semirigid conditions, was reduced in the algorithm. To avoid the formation of fibroblasts,

in fact, the minimum S value that permitted the differentiation into fibroblasts was set to higher values (Table B.1.).

	Mature Osteoblast	**Immature Osteoblast**	**Chondrocyte**	**Fibroblast**
Rat [61]	$0.80 < S \leq 2.53$	$2.53 < S \leq 3$	$3 < S \leq 5$	$S > 5$
Proposed mouse model	$0.80 < S \leq 3$	$3 < S \leq 8$	$8 < S \leq 15$	$S > 15$

Table B.1. – Original and newly proposed ranges for mechano-regulation of healing in mice.

Under this condition, the typical healing phases observed *in vivo* were predicted: woven bone and cartilage presence in the first phases of healing structured the soft callus. The callus presence created the conditions to stabilize the osteotomy gap, which decreased the interfragmentary motion. This led to the production of mature bone during the following iterations and, consequently, to the hard callus formation. The investigation of the proposed mouse mechano-regulation rule correctly predicted bone healing in the initial phase of healing. However, model predictions diverted from the experimental results in the following phases of healing. To solve this problem, other mechano-regulation ranges were investigated for the mouse healing model.

The difference between tissue area predicted *in silico* and observed *in vivo* at 7, 14 and 21 days was used as an indicator to adapt the differentiation ranges. To reduce the number of factors involved in this investigation, the study was performed only under rigid external conditions. From the proposed mouse model that worked in the first phases of healing, other nine cases were investigated until a satisfactory rule was obtained. To minimize the quantitative difference between *in vivo* and *in silico* results, the predicted and simulated bone tissue and cartilage area were compared. The aim of the investigation was the reduction of the difference between those results at every time-point of the investigation. In many cases, the results showed

positive agreement with experimental results at certain time-points but poor match in others. All the tested case differentiation boundaries are not reported here, but the reduction of the difference with experimental results is shown in Figure B.2.

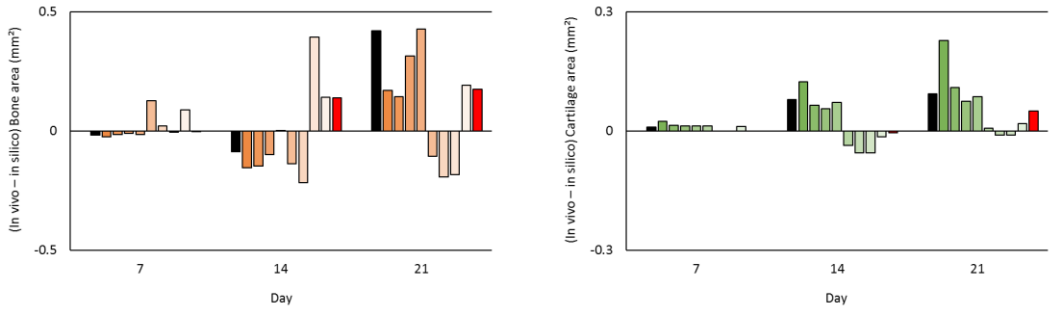

Figure B.2. – Quantitative comparison in bone (left) and cartilage (right) area between experiments and in silico *predictions at 7, 14 and 21 days post-operation under rigid external fixator. Error reduction was reported from the original proposed mouse regulatory rule (black bars) to the ultimate best case scenario (red bars). Multiple tests were performed and their errors are reported in gradient bars.*

The chosen rule to describe the mechano-regulation of bone healing is reported in Table B.2.

	Mature osteoblast	**Immature osteoblast**	**Chondrocyte**	**Fibroblast**
Mouse	$1 < S \leq 6$	$6 < S \leq 13$	$13 < S \leq 35$	$S > 35$

Table B.2. – Ultimate mechano-regulatory rule obtained by the reduction of tissue area errors.

This mechano-regulation rule satisfactory predict bone and cartilage formation under rigid conditions at 7, 14 and 21 days post-operation (red bars in Figure B.2). From a quantitative point of view, a good reduction of the error with experimental results was observed in the bone tissue area at 7 days (proposed model: -0.017 mm^2; ultimate model: -0.001 mm^2) and 21 days (proposed model: 0.420 mm^2; ultimate model: 0.175 mm^2). In cartilage area, a noticeable reduction of the error was observed at 7 days (proposed model:

0.010 mm^2; ultimate model: 0.000 mm^2) and 14 days (proposed model: 0.080 mm^2; ultimate model: -0.004 mm^2). Qualitative comparison with tissue patterning in adult mice showed good agreement also under semirigid conditions (*§ 3.1.3.*).

C

Bone healing model flow chart

Overview

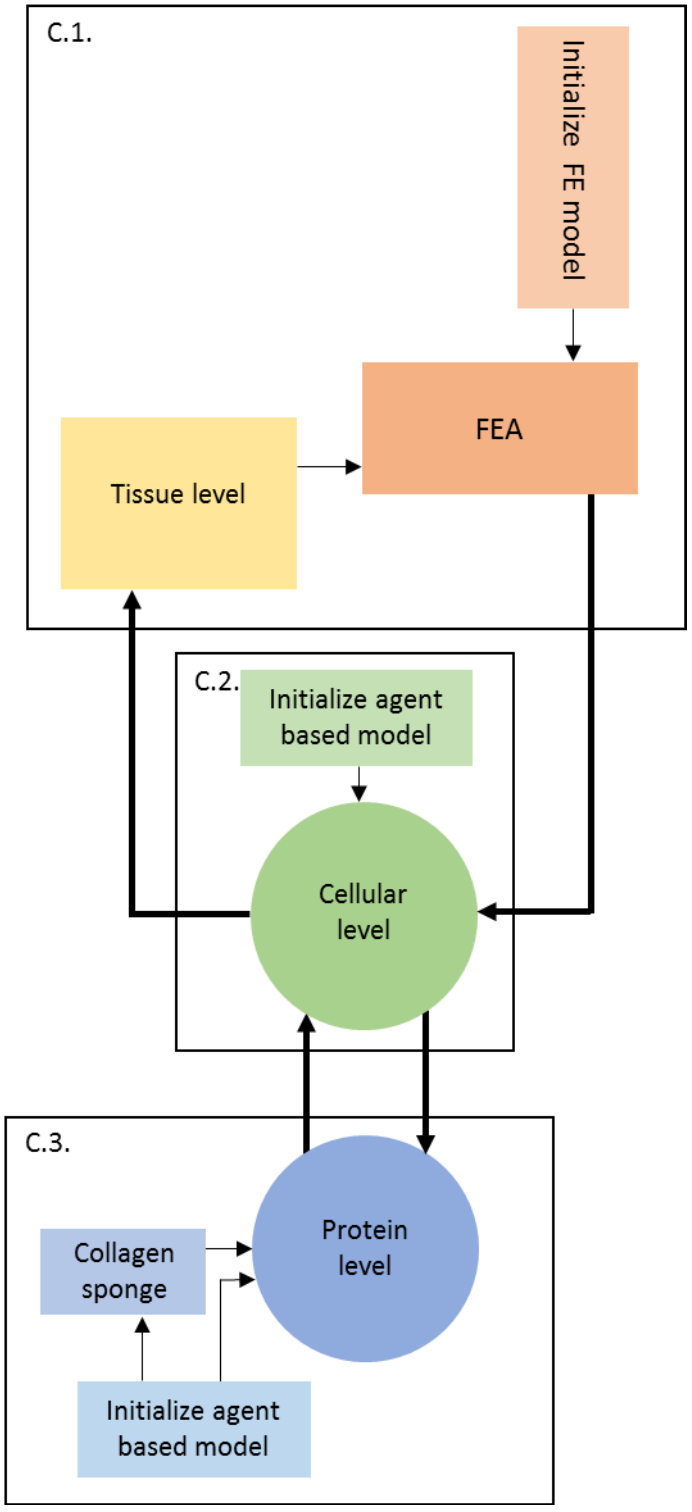
C.1.
Initialize FE model
FEA
Tissue level
C.2.
Initialize agent based model
Cellular level
C.3.
Protein level
Collagen sponge
Initialize agent based model

C.1.

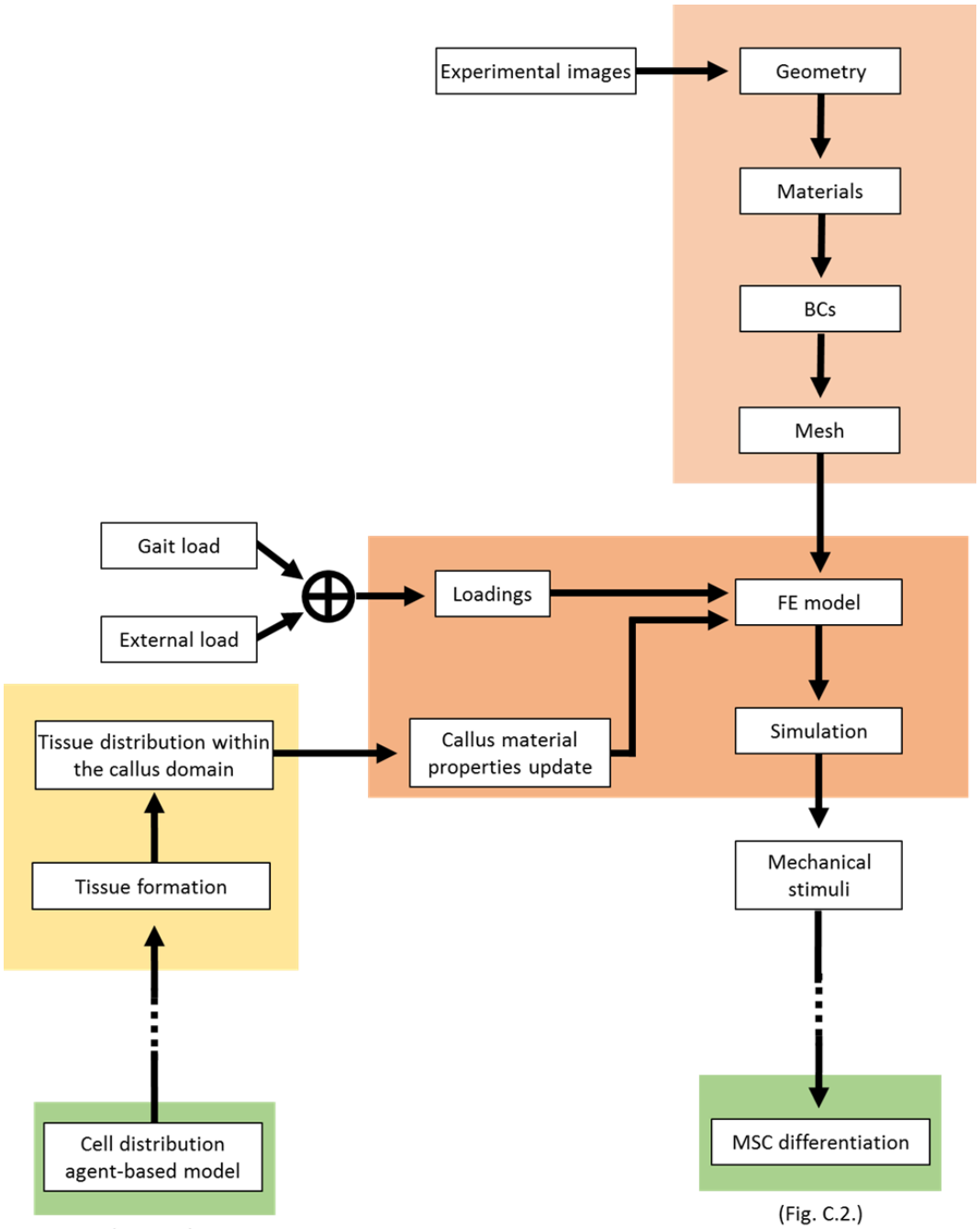

(Fig. C.2.)

(Fig. C.2.)

C.2.

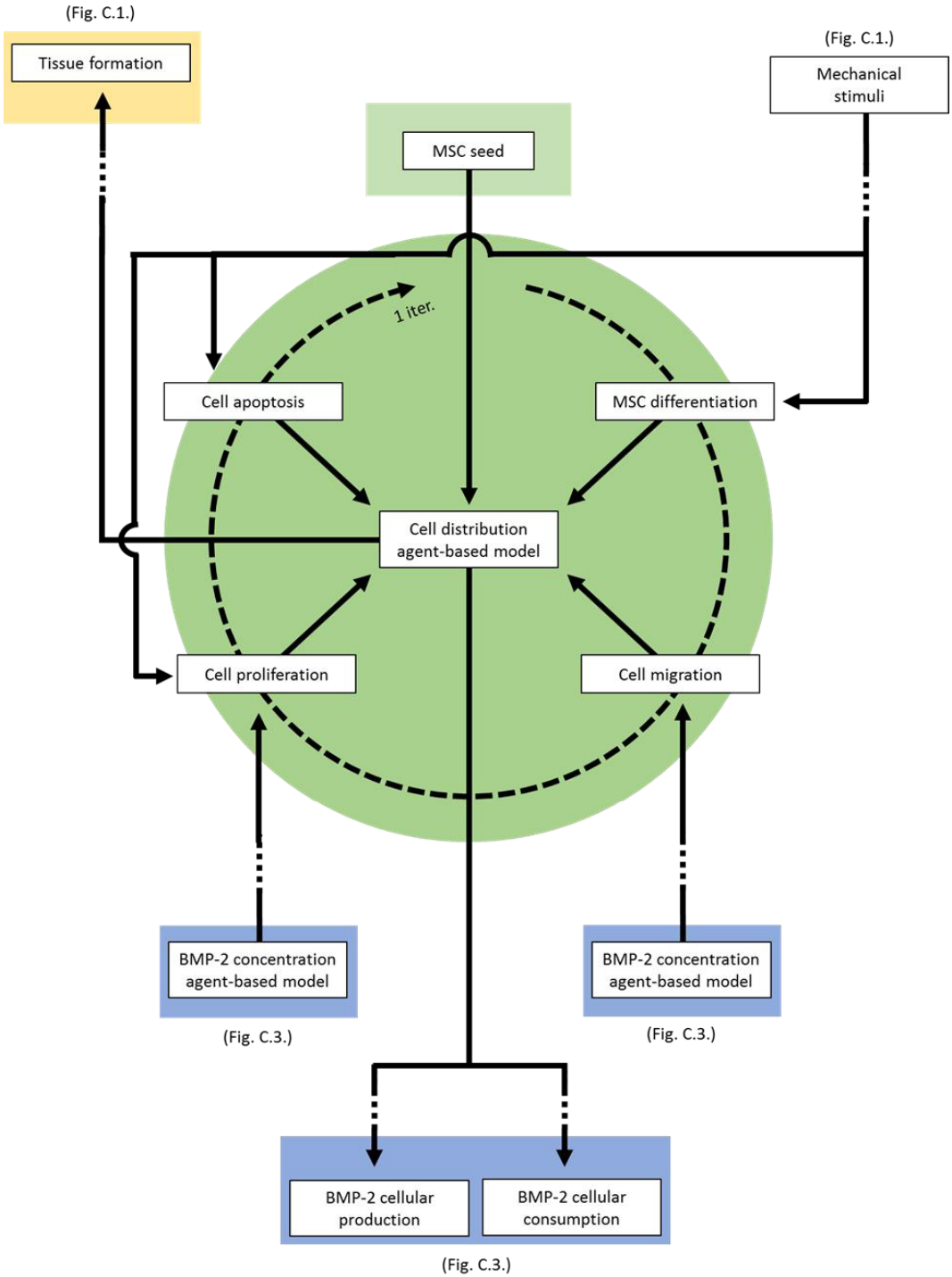
(Fig. C.1.)
Tissue formation
(Fig. C.1.)
Mechanical stimuli
MSC seed
1 iter.
Cell apoptosis
MSC differentiation
Cell distribution agent-based model
Cell proliferation
Cell migration
BMP-2 concentration agent-based model
(Fig. C.3.)
BMP-2 concentration agent-based model
(Fig. C.3.)
BMP-2 cellular production
BMP-2 cellular consumption
(Fig. C.3.)

C.3.

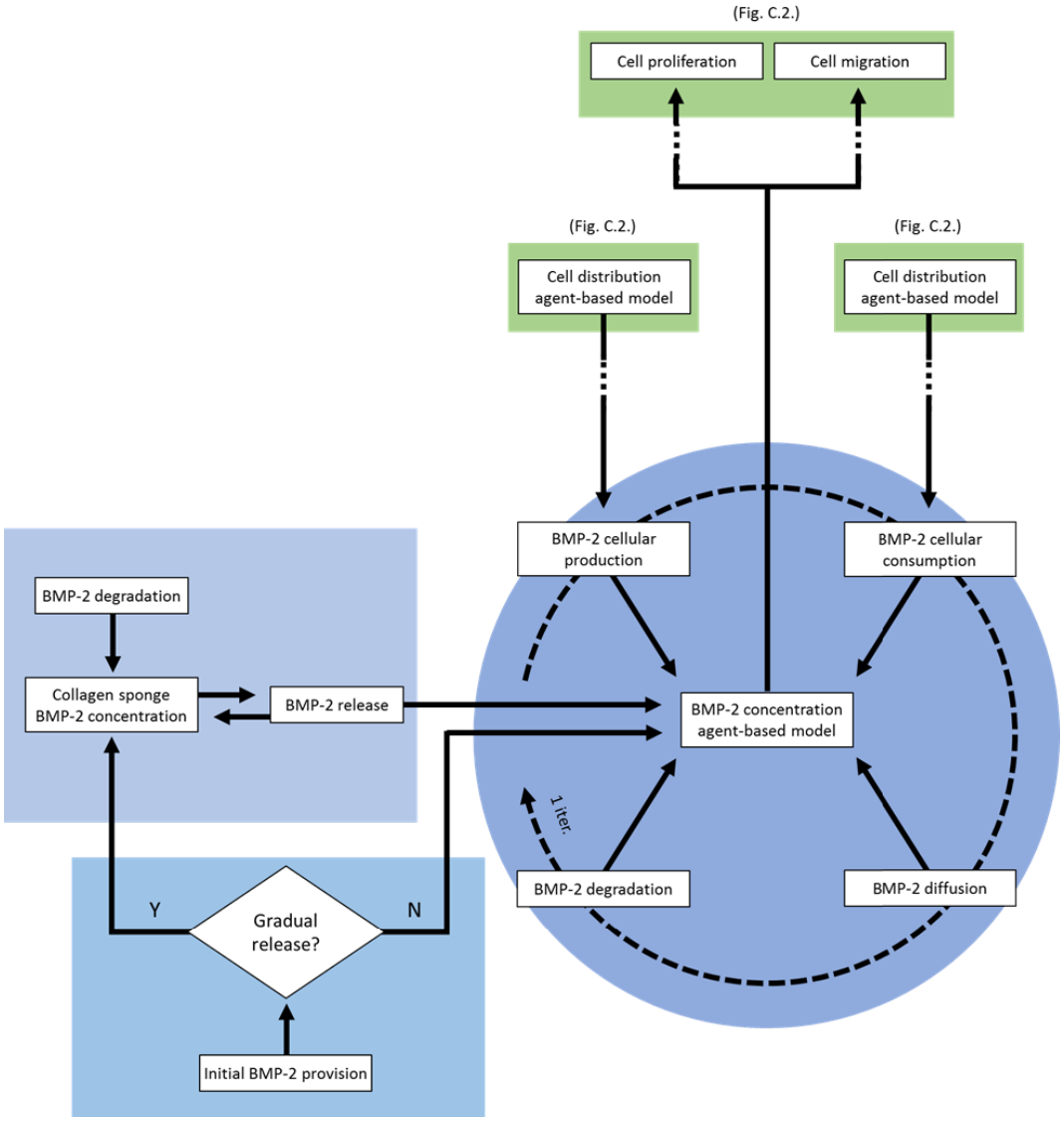
(Fig. C.2.)
Cell proliferation
Cell migration
(Fig. C.2.)
Cell distribution agent-based model
(Fig. C.2.)
Cell distribution agent-based model
BMP-2 cellular production
BMP-2 cellular consumption
BMP-2 degradation
Collagen sponge BMP-2 concentration
BMP-2 release
BMP-2 concentration agent-based model
1 iter.
BMP-2 degradation
BMP-2 diffusion
Y
Gradual release?
N
Initial BMP-2 provision

D

Age-related alteration of mechanosensitivity in mice

Age-related alteration of mechanosensitivity was investigated in this model as a reduction of MSC capacity to sense the mechanical stimuli that drive the differentiation. To simulate this alteration, the different mechanical stimuli driving cell differentiation were moved to higher values. To investigate the effect of aging on mechano-regulation, four different case studies were investigated. Two different strategies were followed: (1) multiplication by 1.5 and 2 of the limits of the mechano-regulatory stimulus (S) (Table D.1.: cases A and B) and (2) shifting of the limits to higher values by adding +1 and +3 (Table D.1.: cases C and D).

	Adult mouse	**Altered MSC mechanoresponse**			
		Case A	Case B	Case C	Case D
Resorption	$S \leq 0.8$	$S \leq 1.2$	$S \leq 1.6$	$S \leq 1.8$	$S \leq 3.8$
Silent zone	$0.8 < S \leq 1$	$1.2 < S \leq 1.5$	$1.6 < S \leq 2$	$1.8 < S \leq 2$	$3.8 < S \leq 4$
Immature osteoblasts	$1 < S \leq 6$	$1.5 < S \leq 9$	$2 < S \leq 12$	$2 < S \leq 7$	$4 < S \leq 9$
Mature osteoblasts	$6 < S \leq 13$	$9 < S \leq 19.5$	$12 < S \leq 26$	$7 < S \leq 14$	$9 < S \leq 16$
Chondrocytes	$13 < S \leq 35$	$19.5 < S \leq 52.5$	$26 < S \leq 70$	$14 < S \leq 36$	$16 < S \leq 38$
Fibroblasts	$S > 35$	$S > 52.5$	$S > 70$	$S > 36$	$S > 38$

Table D.1. – Proposed age-related alteration of differentiation ranges according to simulate reduced MSC mechanoresponse in mice. Baseline (adult mouse) and the four cases derived from it were reported.

A “silent zone”, where mechanical stimuli do not drive cell differentiation [132], and a “resorption” range of low mechanical stimuli, which drove the remodeling balance to favor the resorption of bone [95], were added. The investigation of the most suitable mechano-regulation rule was performed through a single-parameter analysis.

To evaluate the compromising effect of each case study on the healing outcome, a direct comparison with the baseline model (adult mouse) was performed. Age-altered bone and cartilage tissue area were evaluated at 7, 14 and 21 days under both rigid and semirigid fixator for all the four case studies (Table D.2.). Each value was directly compared with its analogous predicted with the baseline model (adult mouse in Table D.2.) and the percent deviation was calculated. Parameters that deviated more than 30% from the baseline model were considered altered by aging.

	Rigid Fixator						*Semirigid Fixator*					
	Bone Tissue			**Cartilage**			**Bone Tissue**			**Cartilage**		
	mm²			*mm²*			*mm²*			*mm²*		
	7d	14d	21d	7d	14d	21d	7d	14d	21d	7d	14d	21d
Adult mouse	0.04	0.41	0.42	0.00	0.05	0.06	0.03	0.17	0.70	0.02	0.28	0.23
Altered MSC mechanoresponse												
Case A	0.03	**0.25**	**0.27**	0.00	**0.02**	**0.02**	0.04	**0.40**	0.53	**0.01**	0.23	0.17
Case B	0.03	**0.19**	**0.21**	0.00	**0.01**	**0.01**	**0.05**	**0.47**	**0.47**	**0.01**	**0.07**	**0.08**
Case C	0.05	0.32	0.34	0.00	0.05	0.04	0.02	0.17	0.58	0.02	0.28	0.26
Case D	0.03	**0.18**	**0.20**	0.00	0.04	0.05	**0.01**	0.16	**0.43**	**0.01**	0.31	0.29

Table D.2. – Quantitative comparison of bone tissue and cartilage area (mm²) at 7, 14 and 21 days under both rigid and semirigid mechanical conditions for the baseline model (adult mouse) and the four age-related altered MSC mechanoresponse cases. Note: Differences higher than 30% between adult and altered MSC mechanoresponse models are marked in bold.

Case B was the only one that play a major role in tissue area extension (deviation larger than 30%) at all time points on both bone (Day 7: +67%, Day 14: +176%, Day 21: -33%) and cartilage (Day 7: -50%, Day 14: -75%, Day 21: -65%) under semirigid conditions. As major age-related alterations were observed experimentally under semirigid conditions, it was decided to consider Case B as the representative to simulate age-related reduction of mechanosensitivity in mice. The boundaries of Case B characterized mechano-regulation of bone healing in the design of experiments investigation where mechano-sensitivity was set to the elderly level (-1).

Bibliography

[1] Schuit SC, van der Klift M, Weel AE, de Laet CE, Burger H, Seeman E, Hofman A, Uitterlinden AG, van Leeuwen JP, Pols HA. *Fracture incidence and association with bone mineral density in elderly men and women: the Rotterdam Study.* Bone. 2004 Jan;34(1):195-202.

[2] Office of the Surgeon General (US). *Bone Health and Osteoporosis: A Report of the Surgeon General.* 2004.

[3] McKibbin B. *The biology of fracture healing in long bones.* J Bone Joint Surg Br. 1978 May;60-B(2):150-62.

[4] Marsell R, Einhorn TA. *The biology of fracture healing.* Injury. 2011 Jun;42(6):551-5. doi: 10.1016/j.injury.2011.03.031. Epub 2011 Apr 13.

[5] Marsh D. *Concepts of fracture union, delayed union, and nonunion.* Clin Orthop Relat Res. 1998 Oct;(355 Suppl):S22-30.

[6] Gomberg BF, Gruen GS, Smith WR, Spott M. *Outcomes in acute orthopaedic trauma: a review of 130,506 patients by age.* Injury. 1999 Aug;30(6):431-7.

[7] Hommel A, Ulander K, Bjorkelund KB, Norrman PO, Wingstrand H, Thorngren KG. *Influence of optimised treatment of people with hip fracture on time to operation, length of hospital stay, reoperations and mortality within 1 year.* Injury. 2008 Oct;39(10):1164-74. doi: 10.1016/j.injury.2008.01.048. Epub 2008 Jun 13.

[8] Haleem S, Lutchman L, Mayahi R, Grice JE, Parker MJ. *Mortality following hip fracture: trends and geographical variations over the last 40 years.* Injury. 2008 Oct;39(10):1157-63. doi: 10.1016/j.injury.2008.03.022. Epub 2008 Jul 24.

[9] Wiese A, Pape HC. *Bone defects caused by high-energy injuries, bone loss, infected nonunions, and nonunions.* Orthop Clin North Am. 2010 Jan;41(1):1-4, table of contents. doi: 10.1016/j.ocl.2009.07.003.

[10] Arrington ED, Smith WJ, Chambers HG, Bucknell AL, Davino NA. *Complications of iliac crest bone graft harvesting.* Clin Orthop Relat Res. 1996 Aug;(329):300-9.

[11] Kokubo S, Mochizuki M, Fukushima S, Ito T, Nozaki K, Iwai T, Takahashi K, Yokota S, Miyata K, Sasaki N. *Long-term stability of bone tissues induced by an osteoinductive biomaterial, recombinant human bone morphogenetic protein-2 and a biodegradable carrier.* Biomaterials. 2004 May;25(10):1795-803.

[12] Cahill KS, Chi JH, Day A, Claus EB. *Prevalence, complications, and hospital charges associated with use of bone-morphogenetic proteins in spinal fusion procedures.* JAMA. 2009 Jul;302(1):58-66. doi: 10.1001/jama.2009.956.

[13] Zara JN, Siu RK, Zhang X, Shen J, Ngo R, Lee M, Li W, Chiang M, Chung J, Kwak J, Wu BM, Ting K, Soo C. *High doses of bone morphogenetic protein 2 induce structurally abnormal bone and inflammation in vivo.* Tissue Eng Part A. 2011 May;17(9-10):1389-99. doi: 10.1089/ten.TEA.2010.0555. Epub 2011 Mar 3.

[14] Cahill KS1, McCormick PC2, Levi AD3. *A comprehensive assessment of the risk of bone morphogenetic protein use in spinal fusion surgery and postoperative cancer diagnosis.* J Neurosurg Spine. 2015 Jul;23(1):86-93. doi: 10.3171/2014.10.SPINE14338. Epub 2015 Apr 10.

[15] Krishnan L, Priddy LB, Esancy C, Klosterhoff BS, Stevens HY, Tran L, Guldberg RE. *Delivery vehicle effects on bone regeneration and heterotopic ossification induced by high dose BMP-2.* Acta Biomater. 2017 Feb;49:101-112. doi: 10.1016/j.actbio.2016.12.012. Epub 2016 Dec 8.

[16] Oryan A, Monazzah S, Bigham-Sadegh A. *Bone injury and fracture healing biology.* Biomed Environ Sci. 2015 Jan;28(1):57-71. doi: 10.3967/bes2015.006.

[17] Schmidt-Bleek K, Petersen A, Dienelt A, Schwarz C, Duda GN. *Initiation and early control of tissue regeneration - bone healing as a model system for tissue regeneration.* Expert Opin Biol Ther. 2014 Feb;14(2):247-59. doi: 10.1517/14712598.2014.857653.

[18] Augat P, Burger J, Schorlemmer S, Henke T, Peraus M, Claes L. *Shear movement at the fracture site delays healing in a diaphyseal fracture model.* J Orthop Res. 2003 Nov;21(6):1011-7.

[19] Gaston MS, Simpson AH. *Inhibition of fracture healing.* J Bone Joint Surg Br. 2007 Dec;89(12):1553-60.

[20] Hankenson KD, Zimmerman G, Marcucio R. *Biological perspectives of delayed fracture healing.* Injury. 2014 Jun;45 Suppl 2:S8-S15. doi: 10.1016/j.injury.2014.04.003.

[21] Claes L, Augat P, Suger G, Wilke HJ. *Influence of size and stability of the osteotomy gap on the success of fracture healing.* J Orthop Res. 1997 Jul;15(4):577-84.

[22] Klein P, Schell H, Streitparth F, Heller M, Kassi JP, Kandziora F, Bragulla H, Haas NP, Duda GN. *The initial phase of fracture healing is specifically sensitive to mechanical conditions.* J Orthop Res. 2003 Jul;21(4):662-9.

[23] Schell H, Epari DR, Kassi JP, Bragulla H, Bail HJ, Duda GN. *The course of bone healing is influenced by the initial shear fixation stability.* J Orthop Res. 2005 Sep;23(5):1022-8.

[24] Epari DR, Schell H, Bail HJ, Duda GN. *Instability prolongs the chondral phase during bone healing in sheep.* Bone. 2006 Jun;38(6):864-70. Epub 2005 Dec 15.

[25] Skak SV, Jensen TT. *Femoral shaft fracture in 265 children. Log-normal correlation with age of speed of healing.* Acta Orthop Scand. 1988 Dec;59(6):704-7.

[26] Meyer RA Jr, Tsahakis PJ, Martin DF, Banks DM, Harrow ME, Kiebzak GM. *Age and ovariectomy impair both the normalization of mechanical properties and the accretion of mineral by the fracture callus in rats.* J Orthop Res. 2001 May;19(3):428-35.

[27] Nilsson BE, Edwards P. *Age and fracture healing: a statistical analysis of 418 cases of tibial shaft fractures.* Geriatrics. 1969 Feb;24(2):112-7.

[28] Kasper G, Mao L, Geißler S, Draycheva A, Trippens J, Kühnisch J, Tschirschmann M, Kaspar K, Perka C, Duda GN, Klose J. *Insights into mesenchymal stem cell aging: involvement of antioxidant defense and actin cytoskeleton.* Stem Cells. 2009 Jun;27(6):1288-97. doi: 10.1002/stem.49.

[29] Geißler S, Textor M, Kühnisch J, Könnig D, Klein O, Ode A, Pfitzner T, Adjaye J, Kasper G, Duda GN. *Functional comparison of chronological and in vitro aging: differential role of the cytoskeleton and mitochondria in mesenchymal stromal cells.* PLoS One. 2012; 7(12): e52700.

[30] Ode A, Duda GN, Geissler S, Pauly S, Ode JE, Perka C, Strube P. *Interaction of age and mechanical stability on bone defect healing: an early transcriptional analysis of fracture hematoma in rat.* PLoS One. 2014 Sep 4;9(9):e106462. doi: 10.1371/journal.pone.0106462. eCollection 2014.

[31] Yukata K, Xie C, Li TF, Takahata M, Hoak D, Kondabolu S, Zhang X, Awad HA, Schwarz EM, Beck CA, Jonason JH, O'Keefe RJ. *Aging periosteal progenitor cells have reduced regenerative responsiveness to bone injury and to the anabolic actions of PTH 1-34 treatment.* Bone. 2014 May;62:79-89. doi: 10.1016/j.bone.2014.02.002. Epub 2014 Feb 12.

[32] D'Ippolito G, Schiller PC, Ricordi C, Roos BA, Howard GA. *Age-related osteogenic potential of mesenchymal stromal stem cells from human vertebral bone marrow.* J Bone Miner Res. 1999 Jul;14(7):1115-22.

[33] Lu C, Hansen E, Sapozhnikova A, Hu D, Miclau T, Marcucio RS. *Effect of age on vascularization during fracture repair.* J Orthop Res. 2008 Oct;26(10):1384-9. doi: 10.1002/jor.20667.

[34] Almeida M. *Aging mechanisms in bone.* Bonekey Rep. 2012 Jul 1;1. pii: 102.

[35] Checa S, Hesse B, Roschger P, Aido M, Duda GN, Raum K, Willie BM. *Skeletal maturation substantially affects elastic tissue properties in the endosteal and periosteal regions of loaded mice tibiae.* Acta Biomater. 2015 Jul;21:154-64. doi: 10.1016/j.actbio.2015.04.020. Epub 2015 Apr 18.

[36] Aido M, Kerschnitzki M, Hoerth R, Checa S, Spevak L, Boskey AL, Fratzl P, Duda GN, Wagermaier W, Willie BM. *Effect of in vivo loading on bone composition varies with animal age.* Exp Gerontol. 2015 Mar;63:48-58. doi: 10.1016/j.exger.2015.01.048. Epub 2015 Jan 30.

[37] Strube P, Sentuerk U, Riha T, Kaspar K, Mueller M, Kasper G, Matziolis G, Duda GN, Perka C. *Influence of age and mechanical stability on bone defect healing: age reverses mechanical effects.* Bone. 2008 Apr;42(4):758-64. doi: 10.1016/j.bone.2007.12.223. Epub 2008 Jan 12.

[38] Borgiani E, Figge C, Kruck B, Willie BM, Duda GN, Checa S. *Age-Related Changes in the Mechanical Regulation of Bone Healing Are Explained by Altered Cellular Mechanoresponse*. J Bone Miner Res. 2019 May 23. doi: 10.1002/jbmr.3801.

[39] Birkhold AI, Razi H, Duda GN, Weinkamer R, Checa S, Willie BM. *The influence of age on adaptive bone formation and bone resorption.* Biomaterials. 2014 Nov;35(34):9290-301. doi: 10.1016/j.biomaterials.2014.07.051. Epub 2014 Aug 13.

[40] Holguin N, Brodt MD, Sanchez ME, Silva MJ. *Aging diminishes lamellar and woven bone formation induced by tibial compression in adult C57BL/6.* Bone. 2014 Aug;65:83-91. doi: 10.1016/j.bone.2014.05.006. Epub 2014 May 15.

[41] Razi H, Birkhold AI, Weinkamer R, Duda GN, Willie BM, Checa S. *Aging Leads to a Dysregulation in Mechanically Driven Bone Formation and Resorption.* J Bone Miner Res. 2015 Oct;30(10):1864-73. doi: 10.1002/jbmr.2528. Epub 2015 May 1.

[42] Guldberg RE. *Spatiotemporal delivery strategies for promoting musculoskeletal tissue regeneration.* J Bone Miner Res. 2009 Sep;24(9):1507-11. doi: 10.1359/jbmr.090801.

[43] Schmidmaier G, Schwabe P, Wildemann B, Haas NP. *Use of bone morphogenetic proteins for treatment of non-unions and future perspectives.* Injury. 2007 Sep;38 Suppl 4:S35-41.

[44] Boerckel JD, Kolambkar YM, Dupont KM, Uhrig BA, Phelps EA, Stevens HY, García AJ, Guldberg RE. *Effects of protein dose and delivery system on BMP-mediated bone regeneration. Biomaterials.* 2011 Aug;32(22):5241-51. doi: 10.1016/j.biomaterials.2011.03.063. Epub 2011 Apr 20.

[45] Schwarz C, Wulsten D, Ellinghaus A, Lienau J, Willie BM, Duda GN. *Mechanical load modulates the stimulatory effect of BMP2 in a rat nonunion model.* Tissue Eng Part A. 2013 Jan;19(1-2):247-54. doi: 10.1089/ten.TEA.2012.0265. Epub 2012 Oct 4.

[46] Glatt V, Miller M, Ivkovic A, Liu F, Parry N, Griffin D, Vrahas M, Evans C. *Improved healing of large segmental defects in the rat femur by reverse dynamization in the presence of bone morphogenetic protein-2.* J Bone Joint Surg Am. 2012 Nov 21;94(22):2063-73. doi: 10.2106/JBJS.K.01604.

[47] Cuenca-López MD1, Peris JL, García-Roselló M, Atienza C, Prat J, Becerra J, Andrades JA. *Action of recombinant human BMP-2 on fracture healing in rabbits is dependent on the mechanical environment.* J Tissue Eng Regen Med. 2010 Oct;4(7):543-52. doi: 10.1002/term.271.

[48] Fiedler J, Röderer G, Günther KP, Brenner RE. *BMP-2, BMP-4, and PDGF-bb stimulate chemotactic migration of primary human mesenchymal progenitor cells.* J Cell Biochem. 2002;87(3):305-12.

[49] Lind M, Eriksen EF, Bünger C. *Bone morphogenetic protein-2 but not bone morphogenetic protein-4 and -6 stimulates chemotactic migration of human osteoblasts, human marrow osteoblasts, and U2-OS cells.* Bone. 1996 Jan;18(1):53-7.

[50] Knippenberg M, Helder MN, Zandieh Doulabi B, Wuisman PI, Klein-Nulend J. *Osteogenesis versus chondrogenesis by BMP-2 and BMP-7 in adipose stem cells.* Biochem Biophys Res Commun. 2006 Apr 14;342(3):902-8. Epub 2006 Feb 20.

[51] Caron MM, Emans PJ, Cremers A, Surtel DA, Coolsen MM, van Rhijn LW, Welting TJ. *Hypertrophic differentiation during chondrogenic differentiation of progenitor cells is stimulated by BMP-2 but suppressed by BMP-7.* Osteoarthritis Cartilage. 2013 Apr;21(4):604-13. doi: 10.1016/j.joca.2013.01.009. Epub 2013 Jan 24.

[52] Huang Z, Ren PG, Ma T, Smith RL, Goodman SB. *Modulating osteogenesis of mesenchymal stem cells by modifying growth factor availability.* Cytokine. 2010 Sep;51(3):305-10. doi: 10.1016/j.cyto.2010.06.002. Epub 2010 Jun 26.

[53] Wang YK, Yu X, Cohen DM, Wozniak MA, Yang MT, Gao L, Eyckmans J, Chen CS. *Bone morphogenetic protein-2-induced signaling and osteogenesis is regulated by cell shape, RhoA/ROCK, and cytoskeletal tension.* Stem Cells Dev. 2012 May 1;21(7):1176-86. doi: 10.1089/scd.2011.0293. Epub 2011 Oct 3.

[54] Shen B, Wei A, Tao H, Diwan AD, Ma DD. *BMP-2 enhances TGF-beta3-mediated chondrogenic differentiation of human bone marrow multipotent mesenchymal stromal cells in alginate bead culture.* Tissue Eng Part A. 2009 Jun;15(6):1311-20. doi: 10.1089/ten.tea.2008.0132.

[55] Sun J, Li J, Li C, Yu Y. *Role of bone morphogenetic protein-2 in osteogenic differentiation of mesenchymal stem cells.* Mol Med Rep. 2015 Sep;12(3):4230-4237. doi: 10.3892/mmr.2015.3954. Epub 2015 Jun 18.

[56] Carter DR, Beaupré GS, Giori NJ, Helms JA. *Mechanobiology of skeletal regeneration.* Clin Orthop Relat Res. 1998 Oct;(355 Suppl):S41-55.

[57] Prendergast PJ, Huiskes R, Søballe K. *ESB Research Award 1996. Biophysical stimuli on cells during tissue differentiation at implant interfaces.* J Biomech. 1997 Jun;30(6):539-48.

[58] Claes LE, Heigele CA. *Magnitudes of local stress and strain along bony surfaces predict the course and type of fracture healing.* J Biomech. 1999 Mar;32(3):255-66.

[59] Bailón-Plaza A, van der Meulen MC. *Beneficial effects of moderate, early loading and adverse effects of delayed or excessive loading on bone healing.* J Biomech. 2003 Aug;36(8):1069-77.

[60] Wehner T, Wolfram U, Henzler T, Niemeyer F, Claes L, Simon U. *Internal forces and moments in the femur of the rat during gait.* J Biomech. 2010 Sep 17;43(13):2473-9. doi: 10.1016/j.jbiomech.2010.05.028. Epub 2010 Jun 20.

[61] Checa S, Prendergast PJ, Duda GN. *Inter-species investigation of the mechano-regulation of bone healing: comparison of secondary bone healing in sheep and rat.* J Biomech. 2011 Apr 29;44(7):1237-45. doi: 10.1016/j.jbiomech.2011.02.074. Epub 2011 Mar 17.

[62] Vetter A, Witt F, Sander O, Duda GN, Weinkamer R. *The spatio-temporal arrangement of different tissues during bone healing as a result of simple mechanobiological rules.* Biomech Model Mechanobiol. 2012 Jan;11(1-2):147-60. doi: 10.1007/s10237-011-0299-x. Epub 2011 Mar 24.

[63] Burke DP, Kelly DJ. *Substrate stiffness and oxygen as regulators of stem cell differentiation during skeletal tissue regeneration: a mechanobiological model.* PLoS One. 2012;7(7):e40737. doi: 10.1371/journal.pone.0040737. Epub 2012 Jul 24.

[64] Steiner M, Claes L, Ignatius A, Niemeyer F, Simon U, Wehner T. *Prediction of fracture healing under axial loading, shear loading and*

bending is possible using distortional and dilatational strains as determining mechanical stimuli. J R Soc Interface. 2013 Jul 3;10(86):20130389. doi: 10.1098/rsif.2013.0389. Print 2013 Sep 6.

[65] Isaksson H, Wilson W, van Donkelaar CC, Huiskes R, Ito K. *Comparison of biophysical stimuli for mechano-regulation of tissue differentiation during fracture healing.* J Biomech. 2006;39(8):1507-16. Epub 2005 Jun 21.

[66] Epari DR, Taylor WR, Heller MO, Duda GN. *Mechanical conditions in the initial phase of bone healing.* Clin Biomech (Bristol, Avon). 2006 Jul;21(6):646-55. Epub 2006 Mar 2.

[67] Geris L, Sloten JV, Van Oosterwyck H. *Connecting biology and mechanics in fracture healing: an integrated mathematical modeling framework for the study of nonunions.* Biomech Model Mechanobiol. 2010 Dec;9(6):713-24. doi: 10.1007/s10237-010-0208-8. Epub 2010 Mar 24.

[68] Gómez-Benito MJ, García-Aznar JM, Kuiper JH, Doblaré M. *Influence of fracture gap size on the pattern of long bone healing: a computational study.* J Theor Biol. 2005 Jul 7;235(1):105-19.

[69] García-Aznar JM, Kuiper JH, Gómez-Benito MJ, Doblaré M, Richardson JB. *Computational simulation of fracture healing: influence of interfragmentary movement on the callus growth.* J Biomech. 2007;40(7):1467-76. Epub 2006 Aug 22.

[70] Ribeiro FO, Folgado J, Garcia-Aznar JM, Gómez-Benito MJ, Fernandes PR. *Is the callus shape an optimal response to a mechanobiological stimulus?* Med Eng Phys. 2014 Nov;36(11):1508-14. doi: 10.1016/j.medengphy.2014.07.015. Epub 2014 Aug 27.

[71] Wehner T, Steiner M, Ignatius A, Claes L. *Prediction of the time course of callus stiffness as a function of mechanical parameters in experimental rat fracture healing studies--a numerical study.* PLoS One. 2014 Dec 22;9(12):e115695. doi: 10.1371/journal.pone.0115695. eCollection 2014.

[72] Carlier A, van Gastel N, Geris L, Carmeliet G, Van Oosterwyck H. *Size does matter: an integrative in vivo-in silico approach for the treatment of critical size bone defects.* PLoS Comput Biol. 2014 Nov 6;10(11):e1003888. doi: 10.1371/journal.pcbi.1003888. eCollection 2014 Nov.

[73] Moore SR, Saidel GM, Knothe U, Knothe Tate ML. *Mechanistic, mathematical model to predict the dynamics of tissue genesis in bone defects via mechanical feedback and mediation of biochemical factors.* PLoS Comput Biol. 2014 Jun 26;10(6):e1003604. doi: 10.1371/journal.pcbi.1003604. eCollection 2014 Jun.

[74] Ribeiro FO, Gómez-Benito MJ, Folgado J, Fernandes PR, García-Aznar JM. *In silico Mechano-Chemical Model of Bone Healing for the Regeneration of Critical Defects: The Effect of BMP-2.* PLoS One. 2015 Jun 4;10(6):e0127722. doi: 10.1371/journal.pone.0127722. eCollection 2015.

[75] Wang Q, Huang C, Xue M, Zhang X. *Expression of endogenous BMP-2 in periosteal progenitor cells is essential for bone healing.* Bone. 2011 Mar 1;48(3):524-32. doi: 10.1016/j.bone.2010.10.178. Epub 2010 Nov 5.

[76] Kim HK, Oxendine I, Kamiya N. *High-concentration of BMP2 reduces cell proliferation and increases apoptosis via DKK1 and SOST in human primary periosteal cells.* Bone. 2013 May;54(1):141-50. doi: 10.1016/j.bone.2013.01.031. Epub 2013 Jan 27.

[77] Huang Z, Nelson ER, Smith RL, Goodman SB. *The sequential expression profiles of growth factors from osteoprogenitors to osteoblasts in vitro.* Tissue Eng. 2007 Sep;13(9):2311-20.

[78] Umulis D, O'Connor MB, Blair SS. *The extracellular regulation of bone morphogenetic protein signaling.* Development. 2009 Nov;136(22):3715-28. doi: 10.1242/dev.031534.

[79] Borgiani E, Duda GN, Checa S. *Multiscale Modeling of Bone Healing: Toward a Systems Biology Approach.* Front Physiol. 2017 May 8;8:287. doi: 10.3389/fphys.2017.00287. eCollection 2017.

[80] Bailón-Plaza A, van der Meulen MC. *A mathematical framework to study the effects of growth factor influences on fracture healing.* J Theor Biol. 2001 Sep 21;212(2):191-209.

[81] Geris L, Gerisch A, Sloten JV, Weiner R, Oosterwyck HV. *Angiogenesis in bone fracture healing: a bioregulatory model.* J Theor Biol. 2008 Mar 7;251(1):137-58. Epub 2007 Nov 19.

[82] Checa S, Prendergast PJ. *A mechanobiological model for tissue differentiation that includes angiogenesis: a lattice-based modeling approach.* Ann Biomed Eng. 2009 Jan;37(1):129-45. doi: 10.1007/s10439-008-9594-9. Epub 2008 Nov 15.

[83] Carlier A, Geris L, Bentley K, Carmeliet G, Carmeliet P, Van Oosterwyck H. *MOSAIC: a multiscale model of osteogenesis and sprouting angiogenesis with lateral inhibition of endothelial cells.* PLoS Comput Biol. 2012;8(10):e1002724. doi: 10.1371/journal.pcbi.1002724. Epub 2012 Oct 11.

[84] Carlier A, Lammens J, Van Oosterwyck H, Geris L. *Computational modeling of bone fracture non-unions: four clinically relevant case studies.* In Silico Cell Tissue Sci. 2015 Dec 18;2:1. eCollection 2015.

[85] *www.3ds.com/products-services/simulia/products/abaqus/abaquscae/*

[86] Kruck B, Zimmermann EA, Damerow S, Figge C, Julien C, Wulsten D, Thiele T, Martin M, Hamdy R, Reumann MK, Duda GN, Checa S, Willie BM. *Sclerostin Neutralizing Antibody Treatment Enhances Bone Formation but Does Not Rescue Mechanically Induced Delayed Healing.* J Bone Miner Res. 2018 Sep;33(9):1686-97. doi: 10.1002/jbmr.3454. Epub 2018 May 23.

[87] Ghiasi MS, Chen J, Vaziri A, Rodriguez EK, Nazarian A. *Bone fracture healing in mechanobiological modeling: A review of principles and methods.* Bone Rep. 2017 Mar 16;6:87-100. doi: 10.1016/j.bonr.2017.03.002. eCollection 2017 Jun.

[88] *www.matweb.com/*

[89] *www.bloodshed.net/dev/devcpp.html*

[90] *gcc.gnu.org/*

[91] Fan W, Crawford R, Xiao Y. *Structural and cellular differences between metaphyseal and diaphyseal periosteum in different aged rats.* Bone. 2008 Jan;42(1):81-9. Epub 2007 Sep 21.

[92] Lamers E, van Horssen R, te Riet J, van Delft FC, Luttge R, Walboomers XF, Jansen JA. The influence of nanoscale topographical cues on initial osteoblast morphology and migration. Eur Cell Mater. 2010 Nov 9;20:329-43.

[93] Checa S, Prendergast PJ. *Effect of cell seeding and mechanical loading on vascularization and tissue formation inside a scaffold: a mechano-biological model using a lattice approach to simulate cell activity.* J Biomech. 2010 Mar 22;43(5):961-8. doi: 10.1016/j.jbiomech.2009.10.044. Epub 2009 Dec 1.

[94] Huiskes R, Van Driel WD, Prendergast PJ, Søballe K. *A biomechanical regulatory model for periprosthetic fibrous-tissue differentiation.* J Mater Sci Mater Med. 1997 Dec;8(12):785-8.

[95] Lacroix D, Prendergast PJ. *A mechano-regulation model for tissue differentiation during fracture healing: analysis of gap size and loading.* J Biomech. 2002 Sep;35(9):1163-71.

[96] Isaksson H, van Donkelaar CC, Huiskes R, Ito K. *A mechano-regulatory bone-healing model incorporating cell-phenotype specific activity.* J Theor Biol. 2008 May 21;252(2):230-46. doi: 10.1016/j.jtbi.2008.01.030. Epub 2008 Feb 9.

[97] Fick A. *On liquid diffusion.* The London, Edinburgh, and Dublin Philosophical Magazine and Journal of Science. Series 4. Volume 10. 1855. doi: 10.1080/14786445508641925

[98] Fujioka-Kobayashi M, Schaller B, Saulacic N, Pippenger BE, Zhang Y, Miron RJ. *Absorbable collagen sponges loaded with recombinant bone morphogenetic protein 9 induces greater osteoblast differentiation when*

compared to bone morphogenetic protein 2. Clin Exp Dent Res. 2017 Feb 9;3(1):32-40. doi: 10.1002/cre2.55. eCollection 2017 Feb.

[99] Taguchi G, Chowdhurry S, Wu Y. *Taguchi's Quality Engineering Handbook.* Wiley 2005.

[100] Isaksson H, van Donkelaar CC, Huiskes R, Yao J, Ito K. *Determining the most important cellular characteristics for fracture healing using design of experiments methods.* J Theor Biol. 2008 Nov 7;255(1):26-39. doi: 10.1016/j.jtbi.2008.07.037. Epub 2008 Aug 3.

[101] Brinker MR, Bailey DE Jr. *Fracture healing in tibia fractures with an associated vascular injury.* J Trauma. 1997 Jan;42(1):11-9.

[102] Lu C, Saless N, Wang X, Sinha A, Decker S, Kazakia G, Hou H, Williams B, Swartz HM, Hunt TK, Miclau T, Marcucio RS. *The role of oxygen during fracture healing.* Bone. 2013 Jan;52(1):220-9. doi: 10.1016/j.bone.2012.09.037. Epub 2012 Oct 12.

[103] Borgiani E, Duda GN, Willie B, Checa S. *Bone healing in mice: does it follow generic mechano-regulation rules?* Facta Universitatis. Series: Mechanical Engineering 2015;13:217-27.

[104] Gómez-Benito MJ, García-Aznar JM, Kuiper JH, Doblaré M. *A 3D computational simulation of fracture callus formation: influence of the stiffness of the external fixator.* J Biomech Eng. 2006 Jun;128(3):290-9.

[105] Steiner M, Claes L, Ignatius A, Simon U, Wehner T. *Numerical simulation of callus healing for optimization of fracture fixation stiffness.* PLoS One. 2014 Jul 3;9(7):e101370. doi: 10.1371/journal.pone.0101370. eCollection 2014.

[106] Stenderup K, Justesen J, Clausen C, Kassem M. *Aging is associated with decreased maximal life span and accelerated senescence of bone marrow stromal cells.* Bone. 2003 Dec;33(6):919-26.

[107] Webster D, Müller R. *In silico models of bone remodeling from macro to nano--from organ to cell.* Wiley Interdiscip Rev Syst Biol Med. 2011 Mar-Apr;3(2):241-51. doi: 10.1002/wsbm.115. Epub 2010 Aug 25.

[108] Geris L, Vander Sloten J, Van Oosterwyck H. *In silico biology of bone modelling and remodelling: regeneration.* Philos Trans A Math Phys Eng Sci. 2009 May 28;367(1895):2031-53. doi: 10.1098/rsta.2008.0293.

[109] Isaksson H, van Donkelaar CC, Huiskes R, Ito K. *Corroboration of mechanoregulatory algorithms for tissue differentiation during fracture healing: Comparison with in vivo results.* J Orthop Res. 2006 May;24(5):898-907.

[110] Repp F, Vetter A, Duda GN, Weinkamer R. *The connection between cellular mechanoregulation and tissue patterns during bone healing.* Med Biol Eng Comput. 2015 Sep;53(9):829-42. doi: 10.1007/s11517-015-1285-8. Epub 2015 Apr 11.

[111] Khayyeri H, Isaksson H, Prendergast PJ. *Corroboration of computational models for mechanoregulated stem cell differentiation.* Comput Methods Biomech Biomed Engin. 2015;18(1):15-23. doi: 10.1080/10255842.2013.774381. Epub 2013 Mar 15.

[112] Isaksson H, Gröngröft I, Wilson W, van Donkelaar CC, van Rietbergen B, Tami A, Huiskes R, Ito K. *Remodeling of fracture callus in mice is consistent with mechanical loading and bone remodeling theory.* J Orthop Res. 2009 May;27(5):664-72. doi: 10.1002/jor.20725.

[113] Silbermann M, Bar-Shira-Maymon B, Coleman R, Reznick A, Weisman Y, Steinhagen-Thiessen E, von der Mark H, von der Mark K. *Long-term physical exercise retards trabecular bone loss in lumbar vertebrae of aging female mice.* Calcif Tissue Int. 1990 Feb;46(2):80-93.

[114] Hoerth RM, Seidt BM, Shah M, Schwarz C, Willie BM, Duda GN, Fratzl P, Wagermaier W. *Mechanical and structural properties of bone in non-critical*

and critical healing in rat. Acta Biomater. 2014 Sep;10(9):4009-19. doi: 10.1016/j.actbio.2014.06.003. Epub 2014 Jun 12.

[115] Mehta M, Checa S, Lienau J, Hutmacher D, Duda GN. *In vivo tracking of segmental bone defect healing reveals that callus patterning is related to early mechanical stimuli.* Eur Cell Mater. 2012 Nov 2;24:358-71; discussion 371.

[116] Verrier S, Alini M, Alsberg E, Buchman SR, Kelly D, Laschke MW, Menger MD, Murphy WL, Stegemann JP, Schütz M, Miclau T, Stoddart MJ, Evans C. *Tissue engineering and regenerative approaches to improving the healing of large bone defects.* Eur Cell Mater. 2016 Jul 19;32:87-110.

[117] Carlisle PL, Guda T, Silliman DT, Hale RG, Brown Baer PR. *Are critical size bone notch defects possible in the rabbit mandible?* J Korean Assoc Oral Maxillofac Surg. 2019 Apr;45(2):97-107. doi: 10.5125/jkaoms.2019.45.2.97. Epub 2019 Apr 29.

[118] Betz OB, Betz VM, Abdulazim A, Penzkofer R, Schmitt B, Schröder C, Augat P, Jansson V, Müller PE. *Healing of large segmental bone defects induced by expedited bone morphogenetic protein-2 gene-activated, syngeneic muscle grafts.* Hum Gene Ther. 2009 Dec;20(12):1589-96. doi: 10.1089/hum.2009.037.

[119] Geris L, Reed AA, Vander Sloten J, Simpson AH, Van Oosterwyck H. *Occurrence and treatment of bone atrophic non-unions investigated by an integrative approach.* PLoS Comput Biol. 2010 Sep 2;6(9):e1000915. doi: 10.1371/journal.pcbi.1000915.

[120] Cuenca-López MD1, Peris JL, García-Roselló M, Atienza C, Prat J, Becerra J, Andrades JA. *Action of recombinant human BMP-2 on fracture healing in rabbits is dependent on the mechanical environment.* J Tissue Eng Regen Med. 2010 Oct;4(7):543-52. doi: 10.1002/term.271.

[121] Bramono DS, Murali S, Rai B, Ling L, Poh WT, Lim ZX, Stein GS, Nurcombe V, van Wijnen AJ, Cool SM. *Bone marrow-derived heparan sulfate*

potentiates the osteogenic activity of bone morphogenetic protein-2 (BMP-2). Bone. 2012 Apr;50(4):954-64. doi: 10.1016/j.bone.2011.12.013. Epub 2011 Dec 28.

[122] Visser R, Arrabal PM, Becerra J, Rinas U, Cifuentes M. *The effect of an rhBMP-2 absorbable collagen sponge-targeted system on bone formation in vivo.* Biomaterials. 2009 Apr;30(11):2032-7. doi: 10.1016/j.biomaterials.2008.12.046. Epub 2009 Jan 19.

[123] La WG, Kang SW, Yang HS, Bhang SH, Lee SH, Park JH, Kim BS. *The efficacy of bone morphogenetic protein-2 depends on its mode of delivery.* Artif Organs. 2010 Dec;34(12):1150-3. doi: 10.1111/j.1525-1594.2009.00988.x.

[124] Pelaez M, Susin C, Lee J, Fiorini T, Bisch FC, Dixon DR, McPherson JC 3rd, Buxton AN, Wikesjö UM. *Effect of rhBMP-2 dose on bone formation/maturation in a rat critical-size calvarial defect model.* J Clin Periodontol. 2014 Aug;41(8):827-36. doi: 10.1111/jcpe.12270. Epub 2014 Jun 9.

[125] Peiffer V, Gerisch A, Vandepitte D, Van Oosterwyck H, Geris L. *A hybrid bioregulatory model of angiogenesis during bone fracture healing.* Biomech Model Mechanobiol. 2011 Jun;10(3):383-95. doi: 10.1007/s10237-010-0241-7. Epub 2010 Sep 9.

[126] Petersen A, Princ A, Korus G, Ellinghaus A, Leemhuis H, Herrera A, Klaumünzer A, Schreivogel S, Woloszyk A, Schmidt-Bleek K, Geissler S, Heschel I, Duda GN. *A biomaterial with a channel-like pore architecture induces endochondral healing of bone defects.* Nat Commun. 2018 Oct 25;9(1):4430. doi: 10.1038/s41467-018-06504-7.

[127] Montecino-Rodriguez E, Berent-Maoz B, Dorshkind K. *Causes, consequences, and reversal of immune system aging.* J Clin Invest. 2013 Mar;123(3):958-65. doi: 10.1172/JCI64096. Epub 2013 Mar 1.

[128] Gibon E, Lu L, Goodman SB. *Aging, inflammation, stem cells, and bone healing.* Stem Cell Res Ther. 2016 Mar 22;7:44. doi: 10.1186/s13287-016-0300-9.

[129] Weyand CM, Goronzy JJ. *Aging of the Immune System. Mechanisms and Therapeutic Targets.* Ann Am Thorac Soc. 2016 Dec;13 Suppl 5:S422-S428. doi: 10.1513/AnnalsATS.201602-095AW.

[130] Edelberg JM, Reed MJ. *Aging and angiogenesis.* Front Biosci. 2003 Sep 1;8:s1199-209.

[131] Langenfeld EM, Langenfeld J. *Bone morphogenetic protein-2 stimulates angiogenesis in developing tumors.* Mol Cancer Res. 2004 Mar;2(3):141-9.

[132] Huiskes R, Ruimerman R, van Lenthe GH, Janssen JD. *Effects of mechanical forces on maintenance and adaptation of form in trabecular bone.* Nature. 2000 Jun 8;405(6787):704-6.

Acknowledgments

A doctorate is never a one-man achievement. Over the academic maturation, this Ph.D. has helped me to develop interaction with the scientific community and to create strong interpersonal bonds, not only from a professional point of view, with many colleagues with my same passion for the field of research. For this reason, I would like to dedicate the last sentences of my manuscript to thank all those colleagues I was lucky to meet and connect with during the last four years of my professional career.

First of all, I would like to express my deep gratitude to my main supervisor, *Prof. Sara Checa*, who always provided valuable and constructive suggestions during the development of this research work. Her rewarding ideas and feedbacks actively contributed to a productive progress of the project, which resulted in the creation of this manuscript. The smart approach that distinguishes her working method has been of great inspiration throughout this period.

I would also like to express my very great appreciation to my supervisors, *Prof. Georg Duda* and *Prof. Manfred Zehn*, who patiently supported my Ph.D. work with clever and expert advices to strongly enhance the quality of my work with pertinent recommendations and profitable contributions.

I am particularly grateful for the professional collaboration of *Christine Figge*, *Dr. Bettina Kruck* and *Dr. Bettina Willie*. Their work from the experimental side was of paramount importance in providing support to my in silico study and in validating the computer models.

My special thanks are extended to the entire team of the *Julius Wolff Institute* and *Berlin-Brandenburg School of Regenerative Therapies*, who has always assisted me from social and academic points of view. In particular, I want to acknowledge the help provided by *Aline Lückgen*, *Camille Metz* and *Vincenzo*

Orassi in the translation and additional reviewing of multiple sections of this manuscript. My colleagues *Dr. Tamer Abdalrahman*, *Dr. Laia Albiol*, *Dr. Clemens Kühn*, *Ehsan Soodmand* and *Martina Tortorici* were also so kind to support my work with their sharp advices and original suggestions in the biomechanics field and beyond.

Writing the acknowledgments' section is never easy. In this case, it is even more complicated as the more I think of the people that I should include in these few lines, the more the list grows and I am aware that I would need an entire chapter to fit them all. There are many other colleagues and experts that I would like to acknowledge here for their priceless and valuable cooperation. I hope that they will realize how much I appreciate them, even if their names are not mentioned here. *Thank you.*